Chemically exfoliated inorganic nanosheets for nanoelectronics ⊕

Takaaki Taniguchi (iD) ; Leanddas Nurdiwijayanto (iD) ; Renzhi Ma (iD) ; Takayoshi Sasaki ✉ (iD)

Check for updates

🗎 CHORUS

View
Online

Export
Citation

CrossMark

Articles You May Be Interested In

The properties and prospects of chemically exfoliated nanosheets for quantum materials in two dimensions

Appl. Phys. Rev. (February 2021)

Film transfer enabled by nanosheet seed layers on arbitrary sacrificial substrates

APL Mater (May 2015)

Defect-state mediated excitonic transitions and associated electrical nature in exfoliated MoS_2 nanostructures

AIP Conference Proceedings (November 2020)

Chemically exfoliated inorganic nanosheets for nanoelectronics Ⓕ

View Online   Export Citation   CrossMark

Takaaki Taniguchi, Ⓘ Leanddas Nurdiwijayanto, Ⓘ Renzhi Ma, Ⓘ and Takayoshi Sasaki[a] Ⓘ

AFFILIATIONS

World Premier International Center for Materials Nanoarchitectonics (WPI-MANA), National Institute for Materials Science (NIMS),
1-1 Namiki, Tsukuba, Ibaraki 305-0044, Japan

[a]Author to whom correspondence should be addressed: sasaki.takayoshi@nims.go.jp

ABSTRACT

Two-dimensional (2D) nanomaterials constitute one of the most advanced research targets in materials science and engineering in this century. Among various methods for the synthesis of 2D nanomaterials, including top-down exfoliation and bottom-up crystal growth, chemical exfoliation has been widely used to yield monolayers of various layered compounds, such as clay minerals, transition metal chalcogenides (TMDCs), and oxides, long before the discovery of graphene. Soft chemical exfoliation is a technique to weaken the layer-to-layer interaction in layered compounds by chemical modification of interlayer galleries, which promotes monolayer exfoliation. The chemical exfoliation process using organic substances, typically amines, has been applied to a range of layered metal oxides and hydroxides for two decades, establishing high-yield exfoliation into their highly crystalline monolayers and colloidal integration processes have been developed to assemble the resultant 2D nanomaterials into well-organized nanoscale devices. Recently, such a strategy was found to be effective for TMDC and MXene nanosheets, expanding the lineup of functionalities of solution-processed 2D nanomaterial devices from dielectrics, optics, magnetics, and semiconductors to superconductors. Throughout this review, we share the historical research flow, recent progress, and prospects in the development of soft-chemical exfoliation, colloidal integration, and thin film applications of oxides, TMDC, and MXene nanosheets.

TABLE OF CONTENTS

I. BACKGROUND, TARGET, AND FRAMEWORK OF THIS REVIEW

2D nanomaterials have been globally investigated since Geim *et al.* reported the isolation of graphene by tape exfoliation of graphite to observe the quantum Hall effect.[1] Since then, graphene has continually exhibited intriguing properties, such as semiconducting properties[2] and superconductivity[3] in bilayer graphene. The emergence of

28 September 2023 06:36:42

graphene has also triggered intensive research focusing on novel 2D nanomaterials, including graphene derivatives such as graphene oxide (GO),[4] fluorographene,[5] and hydrogenated graphene[6] as well as graphene analogs such as monolayered or few-layered transition metal chalcogenides (TMDCs),[7] black phosphorus (phosphorene),[8] silicon (silicene),[9] and boron (borophane).[10] These 2D nanomaterials exhibit unique functionalities not found in their bulk forms. For example, tunable bandgaps and direct to indirect semiconducting transitions depending on the layer number have been found in semiconducting TMDCs[11] and phosphorene.[12] The modulated electronic structures are beneficial for device applications, such as photo-detectors (PDs) and electroluminescence (EL) devices.[13,14] A controllable degree of valley freedom in the 2D electronic states is attractive to develop valleytronics.[15] Furthermore, van der Waals (vdW) heterostructures formed via heteroassembly of different 2D nanomaterials as building blocks serve as a powerful platform to explore new physical phenomena by coupling different electronic states.[16–18] Because of their extreme thinness, atomically or molecularly thin inorganic crystals are structurally flexible and exhibit very limited absorbance in the visible region, making it possible to develop flexible and transparent devices that are difficult to be fabricated with conventional inorganic materials such as brittle ceramics.[19] Next-generation electronics would be created owing to their novel physical properties and tunability superior to the polymer-based materials used as general components for flexible devices.

Although 2D nanomaterial research has emerged as a relatively recent topic, the chemical exfoliation of layered crystals into isolated monolayers, so-called "nanosheets," was conducted before the discovery of graphene. For example, exfoliated GO nanosheets were already synthesized in 1962[20] and then investigated as a unique monolayer material,[21] although they were denoted as "graphite oxide sheets" because of lack of the technical terms "graphene" and nanosheet at that time. The exfoliation of MoS$_2$ into monolayers via lithium intercalation was reported in 1986.[22] The exfoliation of layered oxides into oxide nanosheets, one of the main target materials of this review, has been systematically studied since the 1990s.[23,24] Simultaneously, colloidal integration techniques using nanosheet dispersions have been applied to construct ultrathin devices, especially for dielectrics, in the past two decades.[25,26] In fact, the interface between 2D nanomaterials and nanoelectronics was found by a series of studies conducted far before the first synthesis of graphene.

Recently, such chemical exfoliation followed by thin film deposition using nanosheet colloids has also been adopted for a wider range of nanoelectronics, owing to the discovery of highly efficient exfoliation methods for other types of layered crystals, including TMDCs and MXenes, with semiconducting, metallic conducting, and superconducting properties. Importantly, the latest and most efficient exfoliation methods of these new members rely on the same principle as one developed for exfoliating oxide nanosheets [Figs. 1(a) and 1(b)], where insertion of bulky organoammonium cations into the interlayer space weakens the layer-to-layer interaction, leading to high-yield exfoliation.[27,28] Although, of course, the physical properties of exfoliated nanosheets depend on the crystalline structures and chemical compositions of the resultant nanosheets, these three types of nanosheets exhibit colloidal chemistry similar to each other. This is because they commonly exhibit negative surface charges, which originate in their parent layered structures. As a result, integration techniques to

fabricate thin films can be shared for these three types of negatively charged nanosheets. Therefore, reviewing them together not only provides an efficient understanding of the synthesis, integration, and possible applications of each class of nanosheets but also emphasizes the current common issues to be solved for further development of high-performance devices using these exfoliated nanosheets. 2D metal oxides, TMDCs, and MXenes cover a wide range of functions to construct nanodevices such as insulators, dielectrics, semiconductors, metallic conductors, superconductors, and ferromagnets. Thus, the information provided in this review will be of practical use for researchers in a broad field of applied physics. In this review, we first focus on outlining the advantages of chemical exfoliation by comparing the features of other synthetic methods to obtain 2D nanomaterials, including adhesive tape exfoliation, ultrasonic exfoliation, gas-phase growth, and solution-phase growth methods [Figs. 2(a)–2(e) and Table I]. Note that the 2D nanomaterials synthesized by the other methods are also denoted as nanosheets hereafter. Subsequently, we will explain the principle, processes, and advantages of the chemical exfoliation of layered compounds. Next, we introduce integration techniques of exfoliated nanosheets into thin films for use in nanoelectronic devices. Finally, examples of ultrathin device applications will be provided, followed by a discussion to share the current status and perspective of 2D nanomaterial research based on chemically exfoliated nanosheets.

II. SYNTHETIC METHODS OF NANOSHEETS
A. Adhesive tape exfoliation [Fig. 2(a)]

Mechanical exfoliation is one of the most widely used methods to obtain isolated nanosheets from 2D vdW crystals due to its simplicity.[29] In general, 2D vdW crystals can be cleaved because their layered structures are based on strong intraplane and weak interplanar bonds. The method is simple in that single crystals are repeatedly cleaved using adhesive tape until thin layers are obtained. Mechanical exfoliation was applied for the isolation of graphene in 2004[1] and then has been used for the discovery of monolayers of 2H-MoS$_2$,[30] hBN,[31] phosphorene,[32] etc. Recently, mono-, bi-, and trilayers of CrI$_3$ were obtained by this method, leading to the discovery of unique ferromagnetic and antiferromagnetic behavior depending on the number of layers.[33] Hence, this method is still important in the search for new 2D nanomaterials with yet-unrevealed physical phenomena. However, this method is not generally suitable for practical device applications because the yields are low and the sizes of the monolayered and few-layered sheets are rather small.

B. Ultrasonic exfoliation [Fig. 2(b)]

Ultrasonic exfoliation is a technique in which the polycrystalline grains of 2D crystals are dispersed in a polar solvent and exfoliated into nanosheets by ultrasonication.[34] The advantage is that it can be applied to the mass production of 2D nanomaterials cost-effectively. This approach has been continuously developed as a method to produce graphene inks after the tape exfoliation was first achieved.[35] Ultrasonic exfoliation of various 2D vdW crystals such as TMDCs has been systematically investigated by Coleman et al. For example, effects of solvents and sonication conditions on exfoliation were examined in detail.[36] However, thus far, sonication methods yield a mixture of monolayers, few layers, and multilayers with a broad lateral size distribution.[37] Ultrasonic treatment not only induces delamination but also
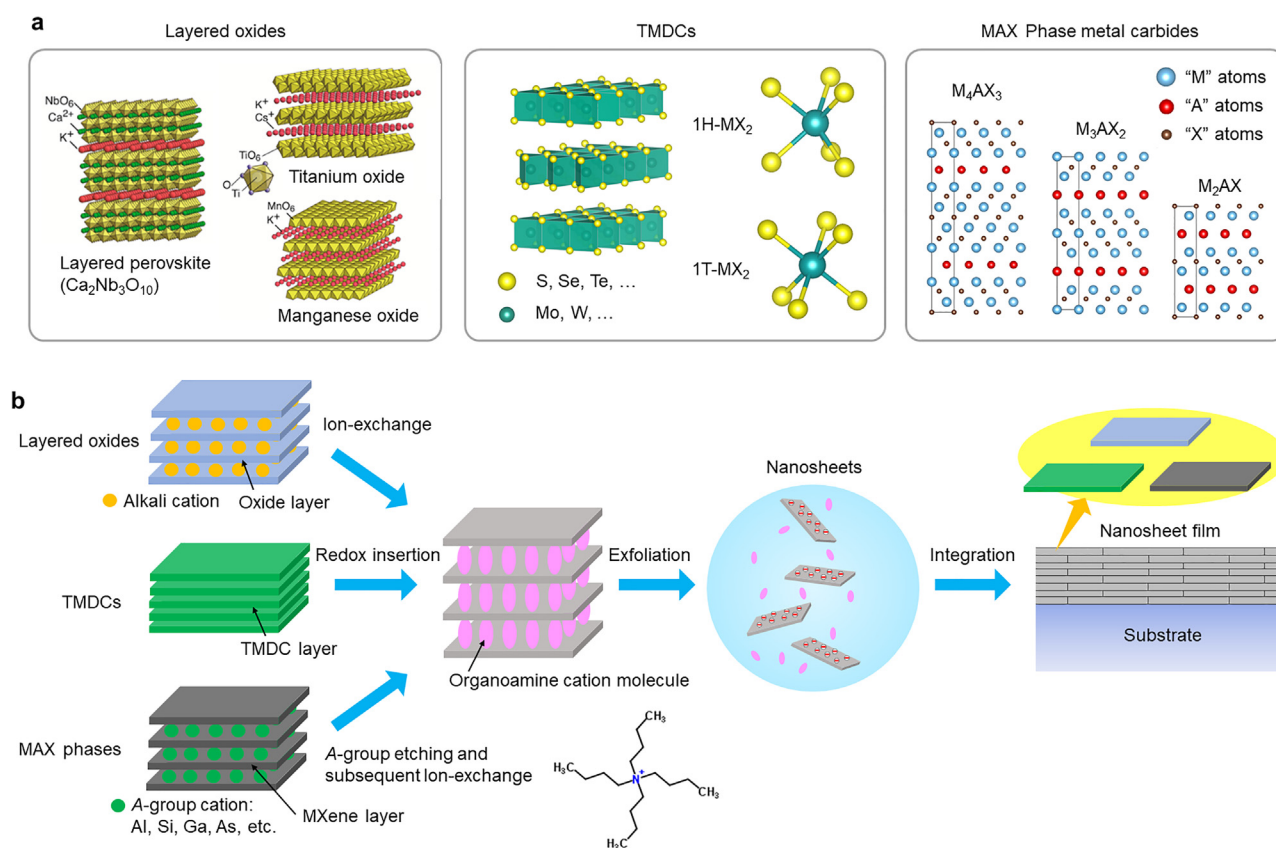
FIG. 1. (a) Crystalline frameworks of exfoliatable layered oxides, TMDCs, and MXenes and (b) their common chemical exfoliation–colloidal integration processes.

breaks the flakes.[38] As a result, the thinner sheets obtained by ultrasonic exfoliation tend to have smaller lateral sizes. Typically, the sheet sizes are as small as a few hundred nm for a few layers. There would be potential applications of these nanoflakes for electronic devices.[39–48] However, it is difficult to offer intriguing features derived from extremely thin thickness, such as transparency and tunability in electronic structures and physical properties.

C. Gas-phase growth [Fig. 2(c)]

For the application of atomically thin materials to devices, it is necessary to develop a technique to fabricate high-quality atomic-layer thin films. Various gas-phase processes, such as chemical vapor deposition (CVD),[49] atomic layer deposition (ALD),[50] pulsed layer deposition (PLD),[51] sputtering,[52] and electron beam deposition (EBD)[53,54] have been studied for this purpose. The most successful case of these methods is CVD,[55] which is a method of depositing films by chemical reaction on the substrate surface by supplying a carrier gas containing the components of the desired thin film. During the last decade, CVD growth has been employed to fabricate a wide variety of 2D nanomaterials, such as graphene,[56] hBN,[57] chalcogenides,[58] and phosphorene.[59] Moreover, certain key issues including large domain size, layer number control, and crystallinity control have been resolved to some extent.[60] The CVD method is the most promising method for application to semiconductor devices in the future, as it can grow high-quality 2D TMDC nanosheets at a relatively reasonable cost. Nevertheless, the CVD process involves a complex growth mechanism, such as sublimation and diffusion processes of multiple precursors. Thus, maintaining the controllability, reproducibility, and high quality of large-scale growth has been a major challenge. Additionally, CVD growth requires high temperatures above ca. 700 °C. As a result, the CVD-grown nanolayer needs to be peeled from the growth substrate followed by transfer onto the polymer substrate in the fabrication of flexible devices. Such complex and multiple processes not only make the nanocoating process more costly but also result in imperfect quality in large-scale coatings.

D. Liquid-phase growth [Fig. 2(d)]

In this method, 2D crystals are grown by the precipitation of a metal ion precursor dissolved in a solvent with an appropriate mineralizing agent. Layered crystals commonly tend to grow in a plate-like shape, as growth in the in-plane direction is kinetically favored. In such a solution growth method, nanosheets consisting of single to several layers can be grown by using appropriate solvents and surfactants to further facilitate 2D anisotropic growth. For example, surfactant-assisted 2D anisotropic growth has been demonstrated with layered metal oxides such as lepidocrocite-type TiO_2 (Ref. 61) and birnessite-
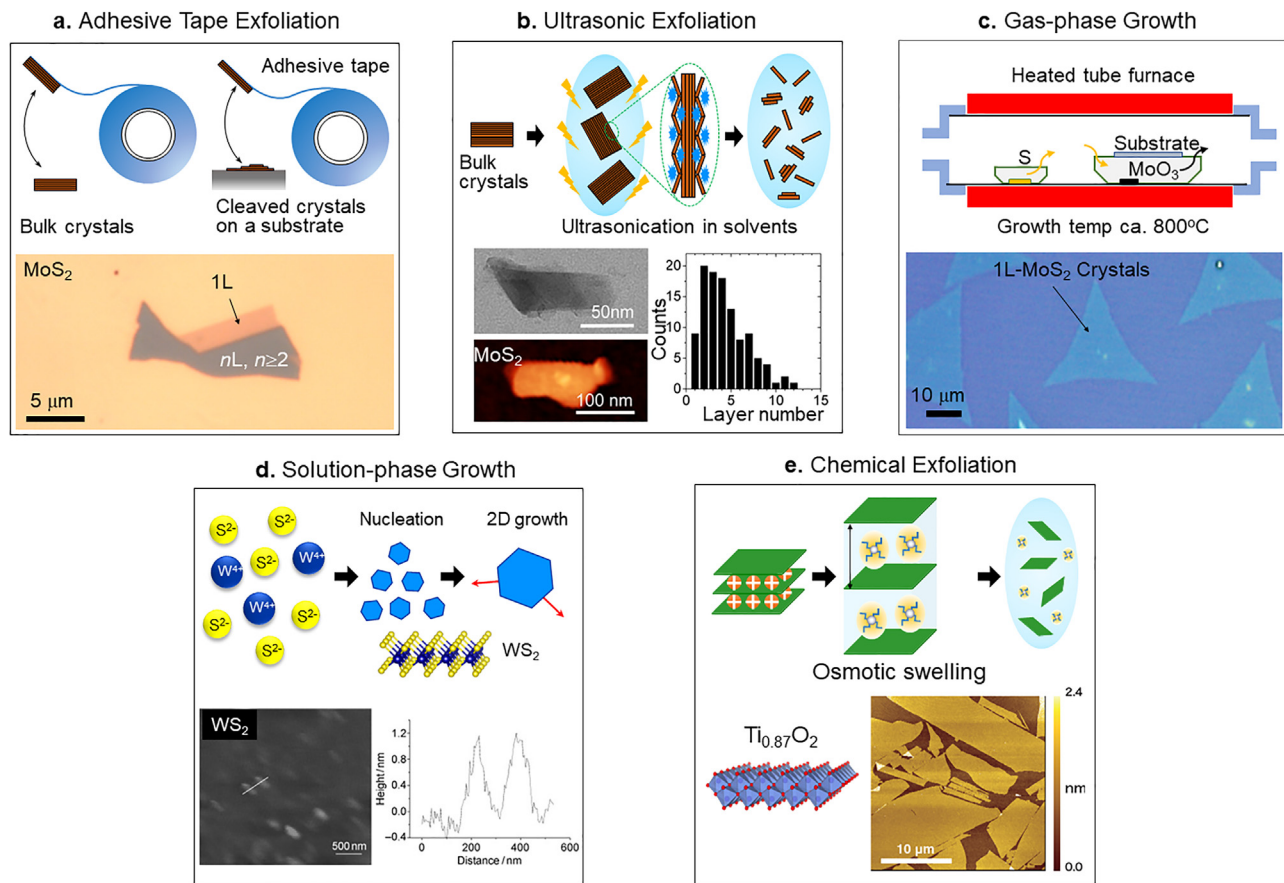
FIG. 2. Synthetic methods for nanosheets. Schematics for (a) tape exfoliation, (b) ultrasonic exfoliation, (c) gas-phase lateral growth, (d) solution-phase growth, and (e) chemical exfoliation. Figure data in panel (b) are reproduced with permission from Varrla *et al.*, Chem. Mater. **27**, 1129 (2015). Copyright 2015 American Chemical Society. Figure data in panel (d) are reproduced with permission from Ramakrishna Matte *et al.*, Angew. Chem. Int. Ed. **49**, 4059 (2010). Copyright 2010 Wiley-VCH.

type MnO_2.[62,63] As a unique advantage, this approach can also be used to produce nanosheets of compounds other than layered forms. For example, Sun *et al.* used inverse lamellar micelles to achieve molecular self-assembly synthesis of ultrathin 2D nanosheets of transition metal oxides.[64] This synthesis procedure has been successfully applied to the preparation of 2D nanostructures of nonlayered metal oxides such as TiO_2, ZnO, Co_3O_4, and Fe_3O_4. Additionally, there are several other solution-based nanosheet growth routes, such as CO capping (Pd),[65] 2D oriented attachment (CeO_2),[66] and surfactant-assisted lamellar formation [ZnO,[67] CeO_2 (Ref. 68)]. The general advantage of liquid phase growth is that mass-scale synthesis is possible by utilizing a relatively inexpensive process, making it suitable for applications that require large quantities, e.g., electrode materials. Nevertheless, these nanosheets have rarely been used to fabricate electronic devices. The small lateral size of nanosheets, generally less than 1 μm, may be a reason for the lack of device applications. Additionally, the low crystallinity of the products, which is a general drawback of any nanomaterial synthesized by low-temperature solution growth, would also make these nanosheets unsuitable for device applications. Furthermore, the synthesis of nanosheets with a complex chemical

TABLE I. Characteristics of the listed synthetic methods for nanosheets.

Synthetic method	Strategy	Crystallinity	Yield of monolayer	Cost	Applicable materials
Adhesive tape exfoliation	Top-down	Excellent	Low	Low	TMDC
Ultrasonic exfoliation	Top-down	Moderate–Low	Low	Low	TMDC/MXene
Gas-phase growth	Bottom-up	Excellent-moderate	High	High	Oxide/TMDC
Solution-phase growth	Bottom-up	Low	Low–high	Low	Oxide/TMDC
Chemical exfoliation	Top-down	Excellent-low	High	Moderate–low	Oxide/TMDC/MXene

28 September 2023 06:36:42

composition has not been attained because of difficulties in controlling the solution reaction.

E. Chemical exfoliation method [Fig. 2(e)]

The chemical exfoliation of layered metal oxides has been systematically studied over the past two decades. In this method, large cations are inserted into the interlayer galleries to weaken the binding forces between the host layers so that high-yield exfoliation into single-layer nanosheets is achieved by applying a small external force. Importantly, all the interlayer galleries in a layered crystal pose equivalent chemical reactivity. Therefore, in principle, all the host layers can be separated into monolayer nanosheets. In contrast, the disintegration of a layered crystal by adhesive tape exfoliation and ultrasonic methods are based on cleavage, where the layered crystal splits into two thinner flakes. Thus, the probability of obtaining a monolayer sheet is inevitably low. The so-called soft-chemical exfoliation route has been extensively investigated to produce oxide nanosheets. Recently, the approach has also played an important role in the synthesis of high-quality TMDC and MXene nanosheets. In this section, we first describe the chemical exfoliation into oxide nanosheets so that researchers in the field of applied physics can understand the principle and chemistry behind the exfoliation process. It would be easy to assess the chemical exfoliation processes to TMDC and MXene nanosheets after understanding the exfoliation process to oxide nanosheets.

1. Chemical exfoliation of metal oxides

Exfoliatable layered metal oxides are commonly composed of negatively charged host layers and interlayer alkali metal cations. For example, layered perovskites form a large category of exfoliatable layered systems. Figure 1(a) displays $KCa_2Nb_3O_{10}$ as a representative exfoliatable Dion–Jacobson (DJ) phase denoted as $A'[A_{n-1}B_nO_{3n+1}]$, where n is the number of BO_6 octahedral units along with the layer normal and A' is the alkali metal ion located between the layers. The Ruddlesden–Popper (RP) phase denoted as $A_2'[A_{n-1}B_nO_{3n+1}]$, such as $K_2SrTa_2O_7$ ($n = 2$), $K_2CaNaTa_3O_{10}$ ($n = 3$),[69] and Aurivillius (AV) phases denoted as $Bi_2O_2[A_{n-1}B_nO_{3n+1}]$, such as $Bi_2SrTa_2O_9$ ($n = 2$)[70] are also exfoliatable layered perovskites. The chemistry of intercalation and exfoliation of these layered perovskites has been recently reviewed by Mallouk et al.[71] A series of layered transition metal oxides, such as titanates,[23] niobates,[72] manganates,[73] titanoniobates,[74,75] tantalates,[76] tungstates,[77,78] and ruthenates,[79] etc., can also be exfoliated. The lineup of oxide nanosheets is reported in our previous review.[80] If the doped and solid solution types of layered oxides are included, the number of potentially exfoliatable layered oxide candidates is quite large.

As a general principle, the exfoliation, or infinite swelling, of layered metal oxides can be achieved when the electrostatic interaction between the adjacent layers is weakened, typically started by a high degree of interlayer expansion via osmotic swelling [Fig. 3(a)]. In this step, the interlayer galleries of the layered oxides are filled with a massive amount of water or solvents. Natural clay minerals with low layer charge density undergo spontaneous swelling and exfoliation reactions in contact with water. On the other hand, layered metal oxides such as $Cs_{0.7}Ti_{1.825}O_4$ (or $K_{0.8}Ti_{1.73}Li_{0.27}O_4$),[23] $KCa_2Na_{n-3}Nb_nO_{3n+1}$ for $n = 3 - 6$,[81] $K_{0.45}MnO_2$,[73,82] and $K_{0.2}RuO_{2.1}$,[79] typically composed of corner-shared or edge-shared MO_6 octahedra ($M = Ti$, Nb, Mn, Ru, etc.) as the host slabs bound with alkali metal cations (K^+, Cs^+, Rb^+,

etc.) have a high layer charge density, providing strong electrostatic attraction between the host layers and interlayer counterions. Such electrostatic attraction causes spontaneous exfoliation similar to clay minerals unfavorable. Thus, preconversion into hydrated protonic forms, such as $H_{0.7}Ti_{1.825}O_4 \cdot H_2O$, $H_{1.07}Ti_{1.73}O_4 \cdot H_2O$, $HCa_2Na_{n-3}Nb_n O_{3n+1} \cdot 1.5H_2O$ for $n = 3 - 6$, $H_{0.13}MnO_2 \cdot 0.7H_2O$, and $H_{0.2}RuO_{2.1} \cdot n H_2O$, is required. This process can be conducted by treating them with an acid solution, facilitated by the ion-exchangeable nature of interlayer alkali metal ions. The protonated forms show unique reactivity known as osmotic swelling when brought into contact with an aqueous solution of organoammonium hydroxides, e.g., tetrabutylammonium hydroxide [$(C_4H_9)_4N^+OH^-$, TBA^+OH^-] and tetramethylammonium hydroxide [$(CH_3)_4N^+OH^-$, TMA^+OH^-]. A large volume of the solution itself is taken up to greatly expand the interlayer galleries, reducing the electrostatic interaction strength between the layers. Consequently, exfoliation can proceed upon applying a small external force, such as shearing by manual or mechanical agitation of the mixtures, yielding a colloidal dispersion [Fig. 3(b)].[83] The $Ti_{0.87}O_2^{0.52-}$ nanosheets thus obtained exhibit unilamellar entities with micrometer-scale lateral dimensions and atomic-scale thicknesses (~ 1 nm) [Fig. 3(b)]. Along with the grain size of the initial layered oxide, the size of the resultant nanosheets generally depends on the exfoliation conditions. For example, when TMA is used for exfoliation, the resulting dispersions show a stream-like Schlieren appearance, indicating a higher degree of anisotropy of the exfoliated products coming from the larger lateral size (~ 10 μm) of the nanosheets than that of those exfoliated with TBA. The standard agitation using reciprocal shaking yields titania nanosheets with a lateral size of ~ 0.5 μm, while gentler hand-shaking results in larger nanosheets up to several tens of micrometers. TEM observation confirms that individual nanosheets are single crystals and free from extrinsic defects possibly induced by the exfoliation process [Fig. 3(c)],[84] which is a common feature for other nanosheets such as $Ca_2Nb_3O_{10}$ (Ref. 85) and $TiNbO_5$.[86] The parent layered oxides are synthesized by high-temperature solid-state reactions typically at 900–1300 °C. Such a high-temperature process allows the formation of highly crystalline products with uniform chemical composition, and nanosheets derived from them inherit such a well-defined nature. Synthesis of TMDC and MXene nanosheets by chemical exfoliation can also start with highly crystalline bulk precursors. Thus, high crystallinity can be a common advantage of chemically exfoliated nanosheets. Nevertheless, we must keep in mind that if redox reactions of the host layers are involved in the ion-exchange and/or exfoliation processes, defects or vacancies can be introduced. Thus, careful control of these chemical processes is required to optimize the crystallinity, i.e., device performance.

As a general physical property change associated with monolayer exfoliation of layered oxides, an increase in bandgap is observed in many oxide nanosheets as well as in TMDCs. For example, the bandgap of the titania nanosheets was determined to be 3.84 eV from the ultraviolet (UV)-Vis absorption and photo-electrochemical action spectra,[87] which is larger than the energy gap of the parent layered titanate (3.2 eV) [Fig. 4(a)].[88] Using the same photo-electrochemical analysis, the bandgaps of $Ca_2Nb_3O_{10}^-$, $TiNbO_5^-$, and $Ti_2NbO_7^{7-}$ nanosheets were determined to be 3.44, 3.68, and 3.64 eV, respectively.[89] These values are larger than that for the parent layered oxides, $KCa_2Nb_3O_{10}$ (3.33 eV), $KTiNbO_5$ (3.51 eV), and $CsTi_2NbO_7$ (3.56 eV). It was further found that the bandgap expansion by
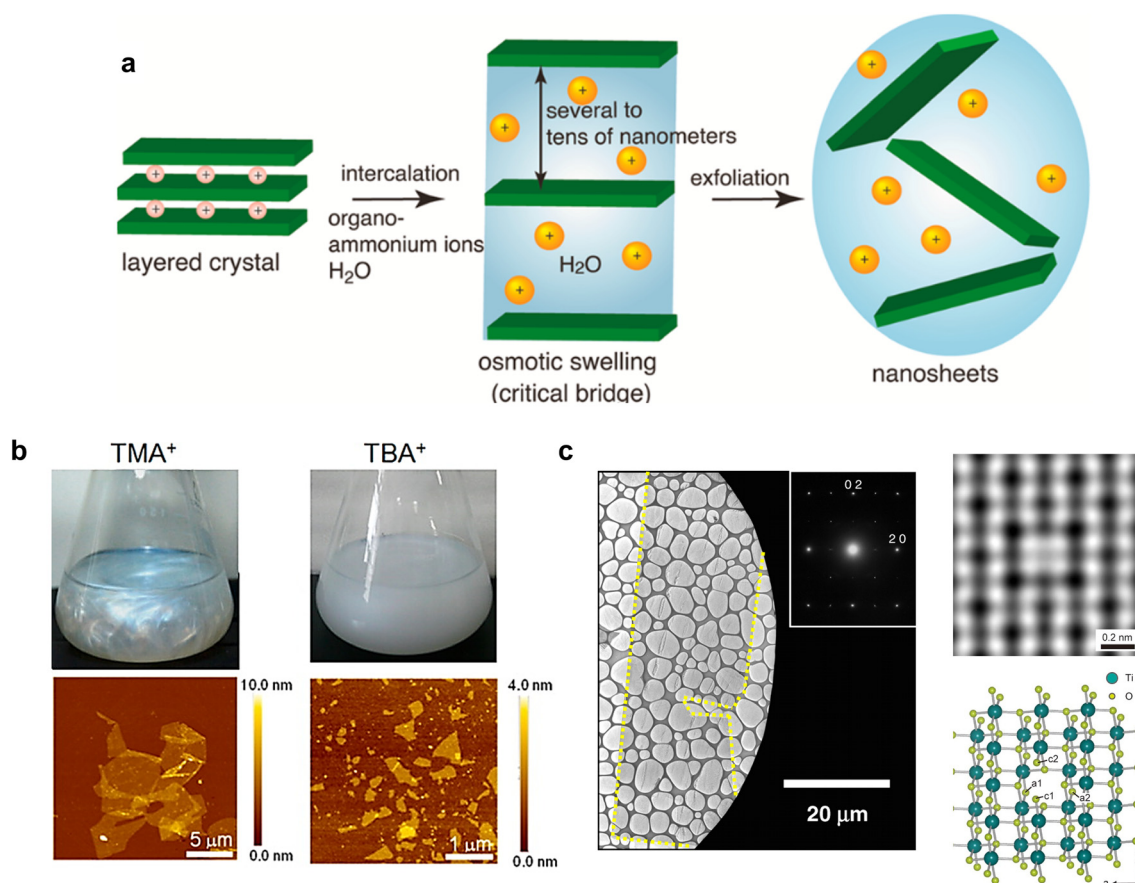
FIG. 3. Chemical exfoliation of layered oxide. (a) Schematic illustration of the osmotic swelling to exfoliation process. (b) Photographs of $Ti_{0.87}O_2^{0.52-}$ nanosheet dispersions exfoliated in aqueous TMA^+ and TBA^+ solutions and the corresponding AFM images. (c) TEM image of exfoliated monolayer $Ti_{0.87}O_2^{0.52-}$ nanosheets, displaying a high degree of crystallinity and free from extrinsic defects. Panel (a) is reproduced with permission from Ma *et al.*, Acc. Chem. Res. **48**, 136 (2015). Copyright 2015 American Chemical Society. Panel (b) is reproduced with permission from Maluangnont *et al.*, Chem. Mater. **25**, 3137 (2013). Copyright 2013 American Chemical Society. Panel (c) is reproduced with permission from Tanaka *et al.*, Chem. Mater. **15**, 3564 (2003). Copyright 2003 American Chemical Society and Ohwada *et al.*, Sci. Rep. **3**, 2801 (2013). Copyright 2013 Authors licensed under a Creative Commons Attribution-NonCommercial-NoDerivs 3.0.

exfoliation was suppressed by increasing the *n* number (increasing the number of NbO_6 octahedra in the nanosheet thickness) in a $Ca_2Na_{n-3}Nb_nO_{3n+1}$ series for $n = 3-6$.[90] The enlarged bandgaps of oxide nanosheets by exfoliation generally maintain after the re-stacking [Fig. 4(b)].[87,91] The random stacking of nanosheets might prevent interactions of the electronic orbitals between adjacent nano-sheets.[92] The enlarged bandgap preserved in multilayer films can enhance the insulating properties beneficial for dielectric applications as will be discussed in Sec. IV A 1.

Several theoretical studies have been conducted to describe the electronic structure of the lepidocrocite titania nanosheet.[93–95] In the first Density Functional Theory (DFT) study by Sato *et al.*, the bandgap of monolayer TiO_2 is calculated to be 3.15 eV, which is larger than that of rutile (2.28 eV) and anatase (2.67 eV) likely due to the quantum size effect in the two-dimensional structure [Fig. 4(c)].[93] The density of states of the TiO_2 nanosheet is a resemblance of anatase, indicating closely related crystal-field splitting and bonding characteristics. In addition, the calculation revealed the highly anisotropic

dielectric constant and mechanical flexibility of the TiO_2 nanosheet. A more recent DFT study by Zhou *et al.* predicts that the lepidocrocite TiO_2 nanosheets exhibit intriguing physical properties such as direct bandgap (5.3 eV), high hole mobility (1069 cm² V⁻¹ s⁻¹), and huge exciton binding energy (1.23 eV).[94]

Factors that control the osmotic swelling process have been revealed to be guidelines in the high-yield exfoliation of oxide nanosheets. According to systematic studies on the exfoliation of layered titanates using TBA^+ as an exfoliation agent,[23,96–98] the TBA^+/H^+ ratio was found to be a key to the massive interlayer expansion required for the subsequent exfoliation, where TBA^+ and H^+ correspond to the molar amount of TBA^+ in the solution and that of H^+ in the proton-ated titanate, respectively. Figure 5(a) shows XRD data for the proton-ated titanate powder ($H_{0.7}Ti_{1.825}O_4 \cdot H_2O$) and the colloidal solutions themselves, obtained via reaction at different TBA^+/H^+ ratios. The $H_{0.7}Ti_{1.825}O_4 \cdot H_2O$ reacted with TBAOH and exhibited a series of new diffraction peaks in the low 2θ region together with a large halo at approximately 20°–50° attributable to background scattering from
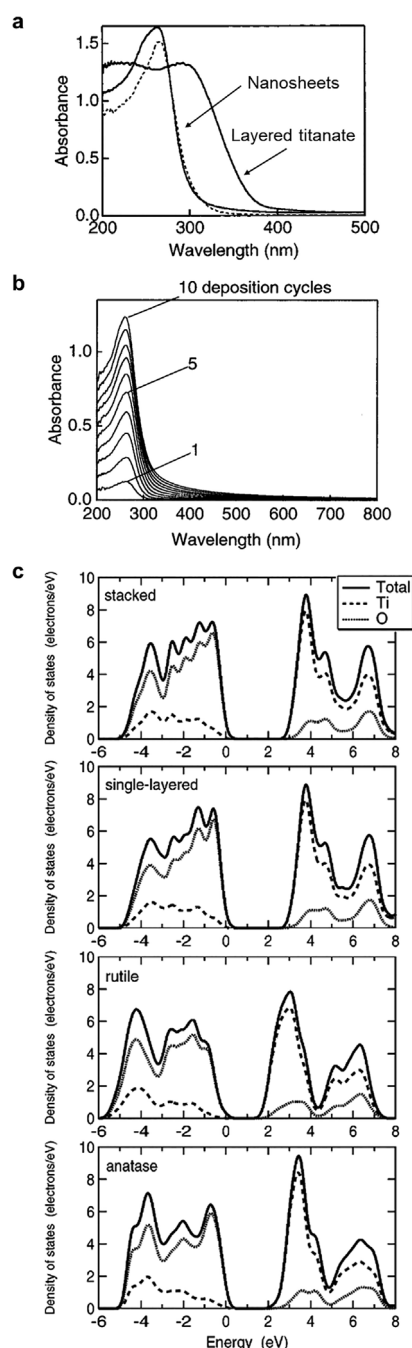
FIG. 4. Electronic band structure of titania nanosheets. (a) UV—visible absorption spectra of protonic layered titanate ($H_{0.7}Ti_{1.825}O_4 \cdot H_2O$) powder, titania nanosheet film (solid), and colloid (dots). (b) UV-visible spectra in the multilayer buildup process of titania nanosheets. (c) Total and partial density of states for stacked and single-layered TiO_2 nanosheets, rutile, and anatase TiO_2. Panel (a) is reproduced with permission from Sasaki et al., J. Phys. Chem. B **101**, 10159 (1997). Copyright 1997 American Chemical Society. Panel (b) is reproduced with permission from Sasaki et al., Chem. Mater. **13**, 4661 (2001). Copyright 2001 American Chemical Society. Panel (c) is reproduced with permission from Sato et al., J. Phys. Chem. B **107**, 9824 (2003). Copyright 2003 American Chemical Society.

water. A sample at $TBA^+/H^+ = 0.1$ showed two immiscible diffraction peaks, which correspond to the TBA-intercalated titanate (intercalation phase) as well as the original titanate. Samples at $TBA^+/H^+ = 15$ and 25 displayed a series of ordered basal reflections, which are attributable to highly expanded layered structures via osmotic swelling. Diffraction peaks coming from such a swollen structure disappeared at $TBA^+/H^+ = 5$, suggesting the occurrence of exfoliation. XRD data taken on colloidal aggregates recovered from the colloidal mixtures via centrifugation are of great help in gaining a deeper understanding of the swelling and exfoliation phenomena [Fig. 5(b)]. At a TBA^+/H^+ ratio of 2, the sample showed a broad halo-like hump, which shows a close match to the square of the structure factor calculated based on the architecture of the titanate layer. This resemblance, as well as the absence of basal reflections, indicates that the individual titanate layer scatters x-rays without interference, providing strong proof of the exfoliation status. The broad hump gradually disappeared accompanied by the evolution of pronounced ordered basal reflections as the TBA^+/H^+ ratio increased, indicating that osmotic swelling is predominant at high doses of TBA ions. The sample at $TBA^+/H^+ = 25$ showed an intersheet distance of 4.2 nm, which was equal to the value observed from the colloidal suspension itself. The higher concentration of TBA^+, as an inevitable result, leads to a smaller volume of the solution required to compensate for the negative charge of the host layers and vice versa. According to the interpretation of XRD data, a phase diagram of the intercalation/exfoliation/osmotic swelling of layered titanate can be drawn, as depicted in Fig. 5(c). Although the intercalation chemistry of each exfoliatable layered oxide depends on the composition, structure, charge density, and Brønsted acidity,[83] the description elaborated above can be applied to explain the boundaries of intercalation/exfoliation/swelling for other exfoliatable layered metal oxides, such as layered manganese oxide [Fig. 5(d)].[73]

Recent studies using flux-grown platelet crystals of several tens of micrometers provide further insights into the mechanism at the osmotic swelling/exfoliation boundary.[99,100] Interestingly, the reaction between $H_{0.8}Ti_{1.2}Fe_{0.4}O_4 \cdot H_2O$ and an aqueous 2-(dimethylamino)ethanol [DMAE, $(CH_3)_2NC_2H_4OH$] solution yielded stable monolithic swollen crystals, exhibiting gigantic one-direction expansion to ~100 times larger than their original thickness (2–3 μm).[99] The optimum amine to proton ratio induced a huge interlayer separation of up to 90 nm [Fig. 5(e)]. The expanded galleries should be primarily filled with water containing a trace amount of DMAE molecules.[100] A range of organoammonium ions was also found to bring out a similar enormous swelling behavior [Fig. 5(f)]. However, the stability of the swollen crystals is affected by the chemical nature of ammonium ions. Species with relatively smaller size and higher polarity, such as DMAE, stabilize the swollen structure, while those with opposite natures, such as TBA^+ or TMA^+, favor exfoliation [Fig. 5(f)]. Similar expansion-exfoliation behavior upon reaction with various organoammonium ions was also observed in Dion–Jacobson-type layered perovskite niobates ($KCa_2Nb_3O_{10}$).[101,102] More recently, Dudko et al. found large interlayer expansion and delamination of sodium hectorite ($Na_{0.5}Mg_{2.5}Li_{0.5}Si_4O_{10}F_2$) by osmotic swelling in various organic solvents, including propylene carbonate (PC), ethylene carbonate, formamide, etc.[103] These new insights have deepened the fundamental understanding of the swelling—exfoliation phenomena of layered compounds. As will be introduced in Secs. II E 2 and II E 3, exfoliation with organoamines has been recently utilized as a powerful approach to producing TMDC and MXene nanosheets. On the basis of the knowledge obtained through studies on the exfoliation of layered
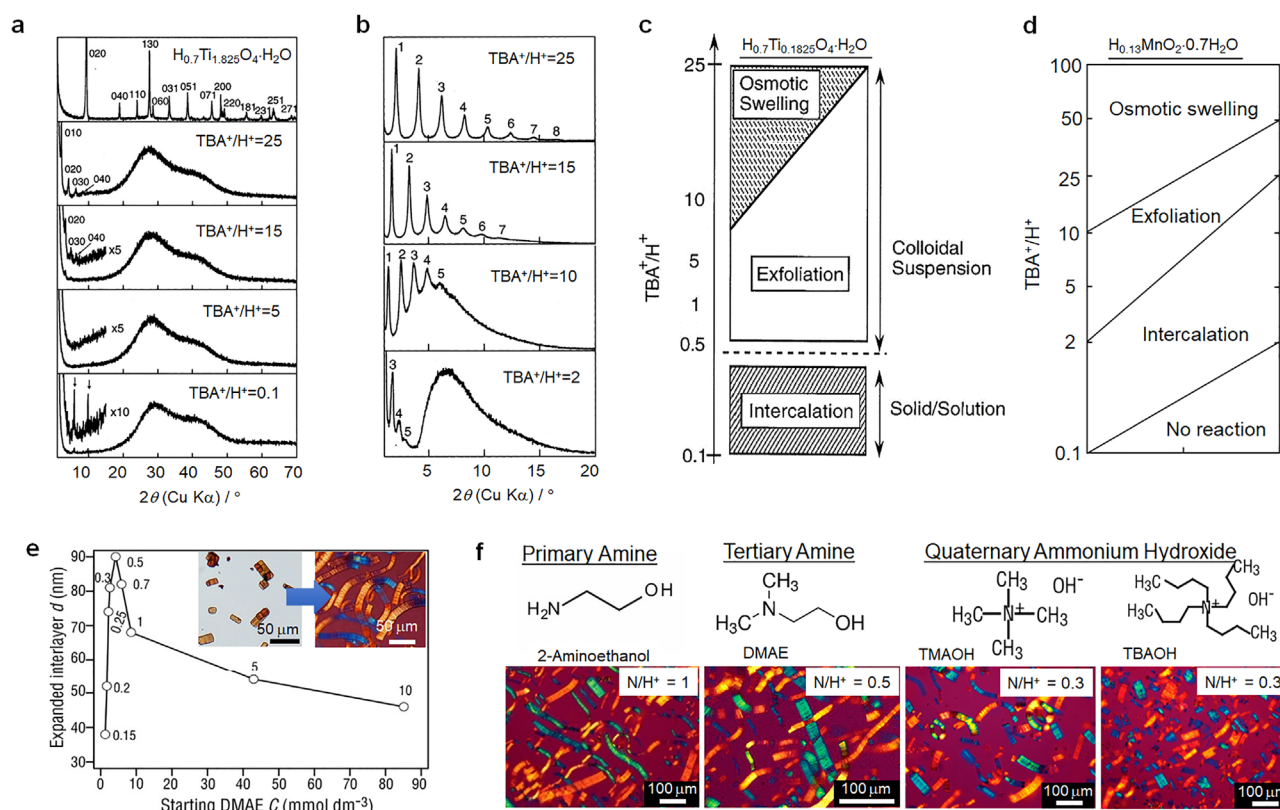
28 September 2023 06:36:42

FIG. 5. Exfoliation mechanism of layered oxide. (a) XRD profiles of protonated titanate ($H_{0.7}Ti_{1.825}O_4 \cdot H_2O$) and their colloidal mixtures obtained by reaction with TBAOH solutions at various concentrations. A ratio of TBA^+/H^+ indicates a molar dose of TBA^+ ions with respect to exchangeable protons in the titanate. (b) XRD profiles of colloidal aggregates recovered from the suspension of (a) via centrifugation. The peaks are indexed based on the order of basal reflections from the swollen titanate. Reaction diagrams between the protonated layered oxides and TBAOH solutions for systems of (c) $H_{0.7}Ti_{1.825}O_4 \cdot H_2O$ and (d) $H_{0.13}MnO_2 \cdot 0.7H_2O$. (e) Expanded interlayer distance of $H_{0.8}[Ti_{1.2}Fe_{0.8}]O_4 \cdot H_2O$ crystals when treated with different doses of DMAE solutions. Inset: Optical microscopy images of $H_{0.8}[Ti_{1.2}Fe_{0.8}]O_4 \cdot H_2O$ platelet crystals before and after treatment with a DMAE solution at $N/H^+ = 0.5$. (f) Polarization optical microscopy images of $H_{0.8}[Ti_{1.2}Fe_{0.8}]O_4 \cdot H_2O$ crystals in solutions of different types of amine and ammonium ions. The DMAE solution produced stable swollen crystals, whereas the TBAOH solution promoted spontaneous exfoliation into unilamellar nanosheets. Panels [(a)–(c)] are reproduced with permission from Sasaki et al., J. Am. Chem. Soc. **120**, 4682 (1998). Copyright 1998 American Chemical Society. Panel (d) is reproduced with permission from Omomo et al., J. Am. Chem. Soc. **125**, 3568 (2003). Copyright 2003 American Chemical Society. Panels (e) and (f) are adapted with permission from Geng et al., J. Am. Chem. Soc. **136**, 5491 (2014). Copyright 2014 American Chemical Society.

oxides and clay minerals, the role of solvents should be considered to improve the exfoliation yields to TMDC and MXene nanosheets.

2. Chemical exfoliation of TMDCs

Approximately 60 transition metal dichalcogenides (TMDCs) with a layered structure have been reported to date,[104] apart from solid solutions. Their structural framework consists of a sheet of hexagonally arranged metal ions, M, which is sandwiched by two sheets of chalcogen atoms, Ch. [Fig. 1(b)]. The M–Ch bond ionicity gives rise to two possible coordination environments: octahedral and triangular prismatic configurations. The octahedral structure arises from the repulsion between the upper and lower Ch atoms linked to the core M when the ionicity is high. The triangular prism-shaped environment, on the other hand, is preferred when the covalent nature of the bonding is high. As a result, group 4 (Ti, Zr, Hf) and group 6 (Mo, W) compounds mainly adopt octahedral and trigonal prismatic configurations, respectively,

while group 5 (Nb, Ta) compounds have both configurations. In their single-layer form, the common polymorphs are categorized into the trigonal-prismatic 1H-phase, the octahedral 1T-phase, and the distorted 1T′-phase. Note that monolayer 1H MoS_2 is often referred to as 2H to connect it to the corresponding bulk state.

Ion-exchangeable interlayer cations are absent in the original TMDCs. However, layered structures can serve as hosts for the intercalation of a wide variety of electron-donating species ranging from Lewis bases to alkali metals. Therefore, similar to the layered oxide described above, modification of the gallery space by insertion of appropriate cations can lead to chemical exfoliation. Taking MoS_2 as an example, the preparation of single-layer materials can be realized by using n-butyl lithium in hexane as the intercalation agent to insert Li^+ ions into the layered structures followed by exfoliation in water with ultrasonication [Fig. 6(a)]. Here, it is suggested that lithium plays dual roles.[22] First, the insertion of Li^+ ions expands the interlayer distance, which weakens the vdW interactions between the layers.
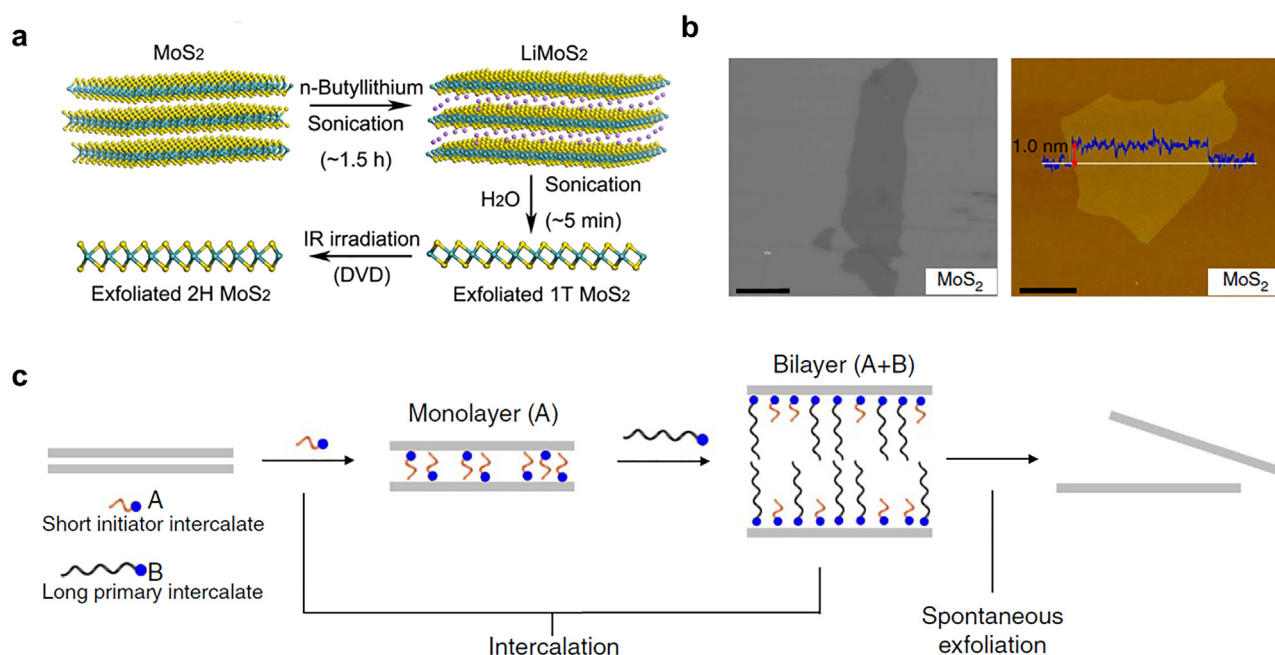
FIG. 6. Chemical exfoliation methods of TMDCs. (a) Scheme of lithium insertion in MoS_2 followed by exfoliation in water. The as-exfoliated MoS_2 nanosheets have a 1T structure. 2H MoS_2 nanosheets are obtained by subsequent thermal activation, such as using the near-IR laser of a commercial DVD optical drive. Reproduced with permission from Fan et al., Nano Lett. **15**, 5956 (2015). Copyright 2015 American Chemical Society. (b) SEM and AFM images of single-layer MoS_2 synthesized with sodium naphthalenide ($A^+C_{10}H_8^-$) for alkali metal insertion. The scale bars in the SEM and AFM images are 10 and 5 μm, respectively. Reproduced with permission from Zheng et al., Nat. Commun. **5**, 2995 (2014). Copyright 2014 Springer Nature Publishing. (c) Scheme of the tandem molecular intercalation (TMI) process for the exfoliation of TMDCs. The TMI process incorporates two different Lewis base intercalates. Short initiator intercalates (orange tail) are intercalated first into the interlayer gap, and then long primary intercalates (black tail) enter to form randomly mixed bilayers of intercalates and widen the interlayer gap. Finally, TMCs with bilayer intercalates are spontaneously delaminated to single-layer nanosheets. Reproduced with permission from Jeong et al., Nat. Commun. **6**, 5763 (2015). Copyright 2015 Springer Nature Publishing.

Second, the intercalated Li reacts with water to produce H_2 gas, cleaving layer-to-layer bonding. Several drawbacks of this original process should be addressed here. First, it requires a high reaction temperature (e.g., 100 °C) and a long reaction time (e.g., three days) for lithiation. Second, the size of the resultant nanosheets is rather small, less than 1 μm, and they are highly defective due to the harsh reductive reaction from Mo^{4+} to Mo^{3+} in the Li intercalation and the delamination process forming H_2 gas inside the gallery.

Zheng et al. explored a two-step expansion and intercalation method to solve these problems.[105] In the process, first, MoS_2 powders were expanded in a hydrothermal condition by reacting with hydrazine (N_2H_4). A redox rearrangement, in which part of N_2H_4 is oxidized to N_2H_5 upon intercalation, is a plausible mechanism behind the expansion. When the intercalated MoS_2 is heated to a high temperature, the intercalated N_2H_5 decomposes into N_2, NH_3, and H_2. An alkali metal naphthalenide ($A^+C_{10}H_8$) is used for reductive insertion in the next step. Note that they used Na and K as intercalants in the synthesis. Because the ionic radii of Na and K ions are larger than that of Li ion, these ions can expand the gallery height to a larger extent. In addition, they explained that Na and K intercalation compounds react more violently with water than Li compounds, implying that single-layer TMDs should be obtained more efficiently. In fact, they attained a high yield of single-layer MoS_2 sheets with a larger lateral width of approximately 10 μm, which is ten times larger than those obtained using n-butyl lithium [Fig. 6(b)]. Additionally, the intercalation

reaction was conducted in a shorter duration of 5 h than the conventional method. Improved exfoliation of TMDC crystals by using Na and K interactions has been confirmed in subsequent studies.[106,107]

Although the exfoliation route via alkali metal intercalation is quite effective, the use of reactive alkali metals and H_2 generation is dangerous for mass production. To avoid this problem, Jeong et al. established the "tandem molecular intercalation (TMI)" approach to produce single-layer 2D TMC nanosheets from colloidal TMDC multilayer nanostructures benignly and effectively.[108] The method employs two distinct Lewis base intercalates [Fig. 6(c)]. To start the gap-widening process, short-length "initiator" Lewis base molecules of propylamine are inserted into the interlayer space of 2D TMDCs. A subsequent ion exchange with long "primary" molecules, butylamine or hexylamine, increases the interlayer distance, allowing for facile exfoliation. This simple process is operative at room temperature without sonication or H_2 generation. Single-layer nanosheets of group IV (TiS_2, ZrS_2), group V (NbS_2), and VI (WSe_2, MoS_2) TMDCs have been successfully synthesized using the proper intercalates.

Phase control is crucial for the potential applications of exfoliated TMDC nanosheets. Monolayer TMDCs, such as MoS_2, WS_2, $MoSe_2$, and WSe_2, exhibit two polymorphs [Fig. 1(b)]: a thermodynamically stable 2H phase and a metastable 1T phase. 2H-phase TMDCs typically show a semiconducting property with bandgaps in a range of 1–2 eV depending on the layer number, while 1T-phase TMDCs exhibit metallic features. Thus, for example, a metallic 1T monolayer

can be used for transparent conductors, while 2H monolayers make them attractive for semiconductor channels in transistors and optical detectors. The 1T phase is dominant for exfoliated TMDC nanosheets synthesized via alkali metal insertion because of heavy electron doping in the intercalation steps. The 2H phase can be restored from the metastable 1T phase nanosheets by postannealing at approximately 200 °C (Refs. 109 and 110) and local heating with a near infrared laser [Fig. 5(a)].[111]

More recently, Lin *et al.* developed the electrochemical intercalation of quaternary ammonium cations (such as tetraheptylammonium

bromide, THAB) into TMDC crystals followed by mild sonication for exfoliation as a general and powerful approach to obtain phase-pure semiconducting TMDC nanosheets [Fig. 7(a)].[27] Because of the large size of THAB of ≈20 Å, the number of ions intercalated and, correspondingly, the number of electrons injected are limited, hampering the 2H to 1T phase transition [Fig. 7(b)]. The expanded MoS_2 crystal by insertion of quaternary ammonium ions was sonicated in a solution of N,N-dimethylformamide (DMF) containing polyvinylpyrrolidone (PVP) in the exfoliation stage. PVP acts as a stabilizing agent,
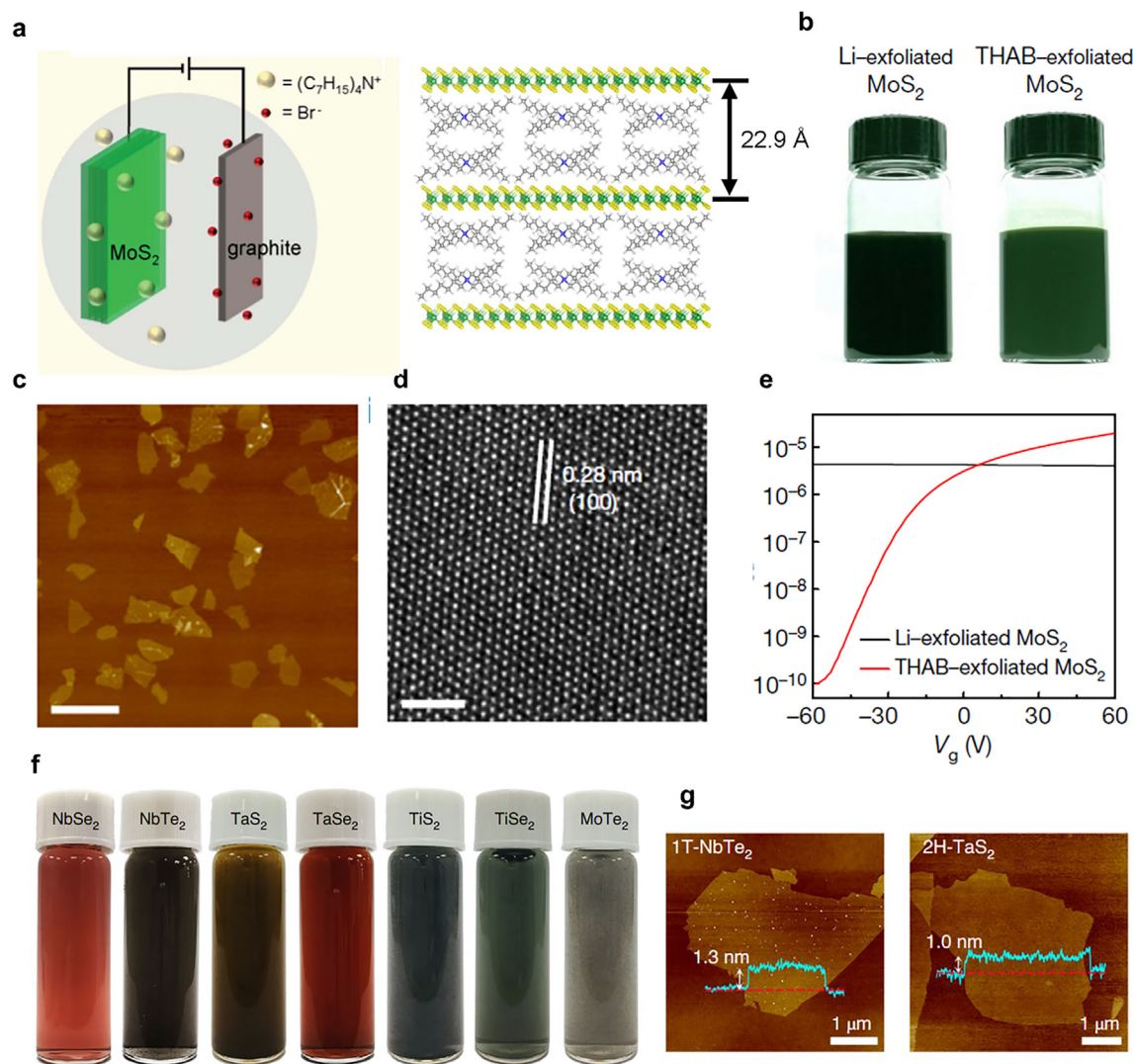

FIG. 7. Electrochemical exfoliation of TMDCs. (a) Schematic of the electrochemical intercalation of MoS_2 and amine-intercalated MoS_2. (b) Photograph of THAB-exfoliated MoS_2 nanosheets in isopropanol and Li-exfoliated MoS_2 nanosheets in water. Li-exfoliated MoS_2 nanosheets were prepared via lithium intercalation, followed by sonication and exfoliation in water. (c) AFM image of THAB-exfoliated MoS_2. Scale bar, 2 μm. (d) High-resolution TEM image of THAB-exfoliated MoS_2 nanosheets. Scale bar, 2 nm. (e) I_{sd}–V_g transfer characteristics of FETs made from a single THAB-exfoliated MoS_2 nanosheet (red) and from a single Li-exfoliated MoS_2 nanosheet (black) on a 300-nm-thick SiO_2/Si substrate and with V_{sd} = 1 V. The semiconducting 2H-phase THAB-exfoliated MoS_2 exhibited a much higher ON/OFF ratio than the metallic 1T-phase Li-exfoliated MoS_2. Reproduced with permission from Lin *et al.*, Nature **562**, 254 (2018). Copyright 2018 Springer Nature Publishing. (f) Photographs of a series of TBA-exfoliated TMDCs dispersed in PC solvent. (g) AFM images and height profiles of the 1T-$NbTe_2$ and 2H-TaS_2 monolayers. Reproduced with permission from Li *et al.*, Nat. Mater. **20**, 181 (2021). Copyright 2021 Springer Nature Publishing.

preventing MoS_2 nanosheets from restacking. The resultant 2H MoS_2 nanosheets were dispersed in isopropanol [Fig. 7(b)]. AFM and TEM observations showed the presence of MoS_2 nanosheets with a few-layer thickness without noticeable defects [Figs. 7(c) and 7(d)]. Furthermore, the electrochemical amine-intercalation approach can be applied for the exfoliation of various TMDCs, including WSe_2, Bi_2Se_3, $NbSe_2$, In_2Se_3, and Sb_2Te_3, demonstrating its potential for generating versatile solution-processable 2D materials. The approach is reproducible[112,113] and has been extended to other TMDCs.[114]

Li *et al.* pointed out that an increase in the cation size inevitably raises the intercalation barrier, lowering intercalation and exfoliation rates of bulk TMDC crystals upon an electrochemical exfoliation process. Thus, they employed a cointercalant of organoammonium cations solvated with a large number of neutral solvent molecules to improve the yield of monolayer exfoliation.[115] In their synthesis, THA dissolved in propylene carbonate (PC) was employed to verify cathodic exfoliation of seven different types of bulk TMDC materials [Fig. 7(f)]. These layered materials demonstrated rapid volumetric expansion and exfoliation into monolayers when a voltage of 5 V was applied to the working electrode of a TMDC crystal [Fig. 7(g)]. A key to high-yield monolayer exfoliation is the insertion of PC molecules with THA ions, which is analogous to the swelling processes observed in the intercalation–exfoliation process of layered oxides in an aqueous solution. The crystallinity of the exfoliated monolayers is superior to that of monolayer flakes synthesized by the MBE and CVD techniques, according to scanning TEM (STEM) analyses. Such an electrochemical intercalation route is being developed to achieve high-yield solution-phase exfoliation of TMDC monolayers in high purity.[116]

3. Chemical exfoliation to MXenes

MXenes are a category of nanosheets obtained through the exfoliation of trielement layered metal carbides and nitrides named the $M_{n+1}AX_n$ (MAX) phase. The MAX phase is characterized by a layered hexagonal crystal structure, as shown in Fig. 1(c). The structure is based on an M_6X octahedron, where the X atoms (C and N) fill the octahedral sites between M atoms such as Sc, Ti, Cr, Zr, and Nb. These octahedra alternate with layers of A elements such as Al, Si, Ga, and Ge located at the center of the triangular prism. When the number n is 1, 2, or 3, the A layers are separated by two, three, or four layers of octahedra, respectively. More than 60 types of MAX phases have now been found. In addition to the typical $M_{n+1}AX_n$, there are also M_2A_2X and $M_{n+1}A_xX_{n+x}$. Furthermore, a wide range of solid solutions can be formed in MAX-phase systems so that the exfoliatable candidates are diverse, similar to layered oxides and TMDCs.

MXene was first reported in 2012 by Naguib *et al.*[28] Since then, synthetic techniques for MXenes have been rapidly developed owing to their various potential applications. Recent progress in the synthesis of MXenes was summarized in detail by Abdolhosseinzadeh *et al.*[117] Therefore, in this review, we briefly describe the overall process and historical flow with key referenced works. The first step in synthesizing MXenes is a selective etching of A layers from MAX phase frameworks. HF was employed for etching in the initially developed method, resulting in platy grains with accordion-like side surfaces [Fig. 8(a)]. After etching, functional groups formed at the $M_{n+1}X_n$ surfaces (OH, O, and F; represented hereafter by T_x) weaken the layer-to-layer

bonding, which then allows separation of the layers from each other via sonication. The yield of monolayer or few-layered MXene was very low at the initial stage. This indicates that strong layer-to-layer bonds persist in A-etched forms. Therefore, interlayer modification has been continuously studied to enhance the yield of MXenes. In 2013, Mashtalir *et al.* reported the intercalation of hydrazine and its cointercalation with N,N-dimethylformamide.[118] The intercalated Ti_3C_2 was delaminated by sonication in water to form a stable colloidal suspension. In 2015, Naguib *et al.* developed a more general approach for the large-scale delamination of MXenes using organoamines [Fig. 8(a)].[28] They used TBAOH and *n*-butylamine to react with $M_{n+1}X_nT_x$. When compared to pristine MAX-phase layered carbide, the intercalated forms showed a significant increase in basal spacing, resulting in efficient delamination to form stable colloidal solutions by manual shaking in water [Fig. 8(b)]. In parallel, Li *et al.* reported delamination of Nb_2CT_x by intercalating isopropylamine followed by mild sonication in water. Thus, the organoamine intercalation approach, used for the synthesis of oxide and TMDC nanosheets, can be widely applied to produce MXene family members. The amine–intercalation–exfoliation routes of MXene synthesis have been rapidly adopted for the synthesis of new MXenes such as Mo_2CT_x[119] and $Ti_4N_3T_x$.[120] Alhabeb *et al.* summarized the synthetic protocols in detail to guide the high-yield exfoliation of MXene,[121] which is a useful place to start the subject of MXene. In addition, in 2016, Xuan *et al.* reported organic-base-driven intercalation and delamination of titanium carbide that takes advantage of the amphoteric nature of the constituent Al [Fig. 8(c)].[122] If this approach can be used for the delamination of other MXenes, the synthesis would be free from the initial acid-etching process.

III. INTEGRATION OF 2D NANOSHEETS

Although the chemical compositions of layered metal oxides, TMDCs, and MXenes are largely different, their nanosheets obtained by chemical exfoliation commonly have a negative surface charge. The negative charge of oxide nanosheets is inherited from their parent layered oxides accommodating alkali metal ions. The negative surface charge of TMDC nanosheets is introduced by reductive cation insertion into the charge-neutral precursor crystals as the pretreatment step for delamination. MXenes are negatively charged after etching of the metal layer between host layers. Thus, they have similar colloidal characteristics so that, in principle, they can be organized into nanofilms using similar solution-based integration approaches. As shown below, the colloidal assembly processes based on monolayer deposition enable atom-scale thickness control that is conventionally achieved only with state-of-the-art vacuum processing, such as ALD, CVD, and MBE, requiring a high deposition temperature. These vacuum processes frequently require an epitaxial relationship between the substrate as a seed and target materials for controlled growth. In contrast, the solution-phase assembly of nanosheets is not limited by the crystalline structure of the substrate, allowing the deposition of films on a range of substrates, e.g., Si/SiO_2, ITO, and Pt/Au. Moreover, solution processing can be performed at room temperature and ambient pressure, which greatly benefits the production of flexible devices composed of plastic substrates. In this chapter, we describe the concepts, methods, and features of film integration techniques using chemically exfoliated nanosheets available thus far.
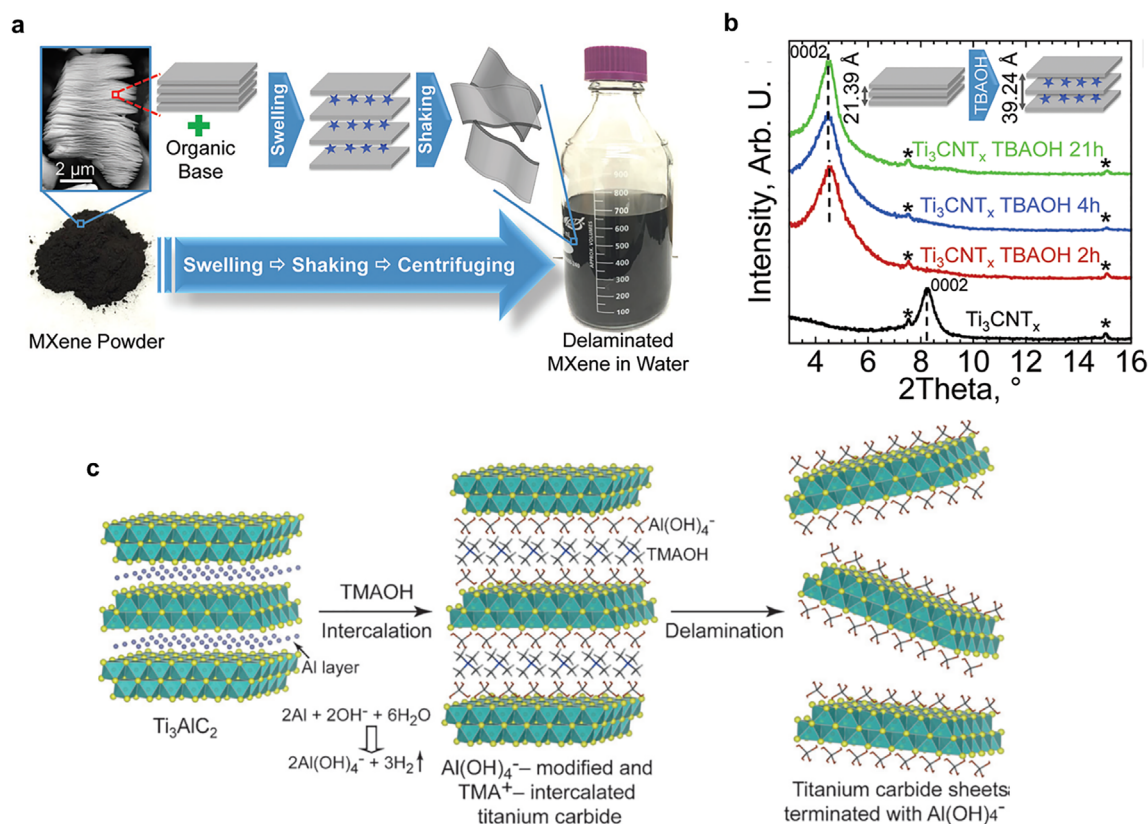
FIG. 8. Chemical exfoliation of MXene. (a) Schematic for the MXene delamination process by reacting Al-etched MAX phase grains with an organic base that causes multilayered grains (pictured in the bottom left) to swell significantly. Then, by simply manual shaking or mild sonication in water, the layers are delaminated, forming a stable colloidal suspension (right side). (b) XRD patterns for Ti_3CNT_x before and after mixing with TBAOH solution for 2, 4, and 21 h (red, blue, and green). The insets are schematics of the MXene unit cells before and after TBAOH intercalation with the corresponding change in the c lattice parameter. Reproduced with permission from Naguib et al., Dalton Trans. **44**, 9353 (2015). Copyright 2015 The Royal Society of Chemistry. (c) Schematic illustration showing the intercalation and delamination process via treatment with the organic base TMAOH. TMAOH reacts with the Al atomic layer in the gallery to promote key processes, including cleavage of the Ti–Al bonds through Al hydrolysis, modification of the TC unit surface with $Al(OH)_4$, and intercalation of bulky TMA^+ into the gallery, all in a single step. The cleavage of Ti-Al metallic bonds and intercalation of bulky ions facilitate the subsequent disintegration of the precursor layered crystals into their elementary layers. Reproduced with permission from Xuan et al., Angew. Chem. Int. Ed. **55**, 14569 (2016). Copyright 2016 Wiley-VCH.

A. Electrostatic layer-by-layer (LbL) deposition

The electrostatic LbL growth technique was first developed by Decher to fabricate layered polymeric multi-nanocomposite films.[123,124] In principle, LbL films can be formed by dipping the substrate into two solutions containing oppositely charged materials in a sequential fashion. To date, the approach has been adopted for a variety of systems of charged materials, including proteins[125,126] and colloidal nanoparticles.[127,128] The LbL deposition of negatively charged nanosheets is driven by an electrostatic attraction force when the substrate surface is positively charged, opposite to that of nanosheets [Fig. 9(a)]. The use of a polycation is of importance to modify the substrate surface charge so as to "glue" the individual nanosheet building blocks into the desired nanostructure. Polyethyleneimine (PEI) and poly(diallyldimethylammonium chloride) (PDDA) are effective polycationic binders widely used for negatively charged oxide nanosheets. The fabrication of multilayered films of nanosheets can be accomplished by repeating the sequential processes. Stepwise deposition can be confirmed using various characterization techniques, such as UV-visible absorption spectroscopy, AFM, ellipsometry, and XRD. Two-dimensional nanosheets can also be assembled with positively charged cationic complexes and inorganic polyoxocations [e.g., silver (Ag)-coordinated PEI[129] and Al_{13} Keggin ions[130,131]] to fabricate unique pillared nanosheet architectures. LbL deposition is well adopted for large-scale coatings as well as coatings on shaped materials.[132] Recently, LbL methods have been used for the deposition of TMDC[113,133,134] and MXene[135–137] nanosheets. As these nanosheets are negatively charged, polycations that are used for the LbL of oxide nanosheets were also used in these studies. The qualities of the TMDC and MXene films produced by LbL are almost identical to those of oxide nanosheet films.

It should be noted that the LbL process sometimes results in the formation of few-layer films in a single deposition cycle [Fig. 9(b), left]. For example, the first report on the assembly of exfoliated nanosheets demonstrated that up to approximately three nanosheet layers were generated within a single deposition cycle of a mica-type clay mineral with PDDA.[138] The formation of a monolayer film can be achieved by carefully tuning the assembly process. Systematic studies
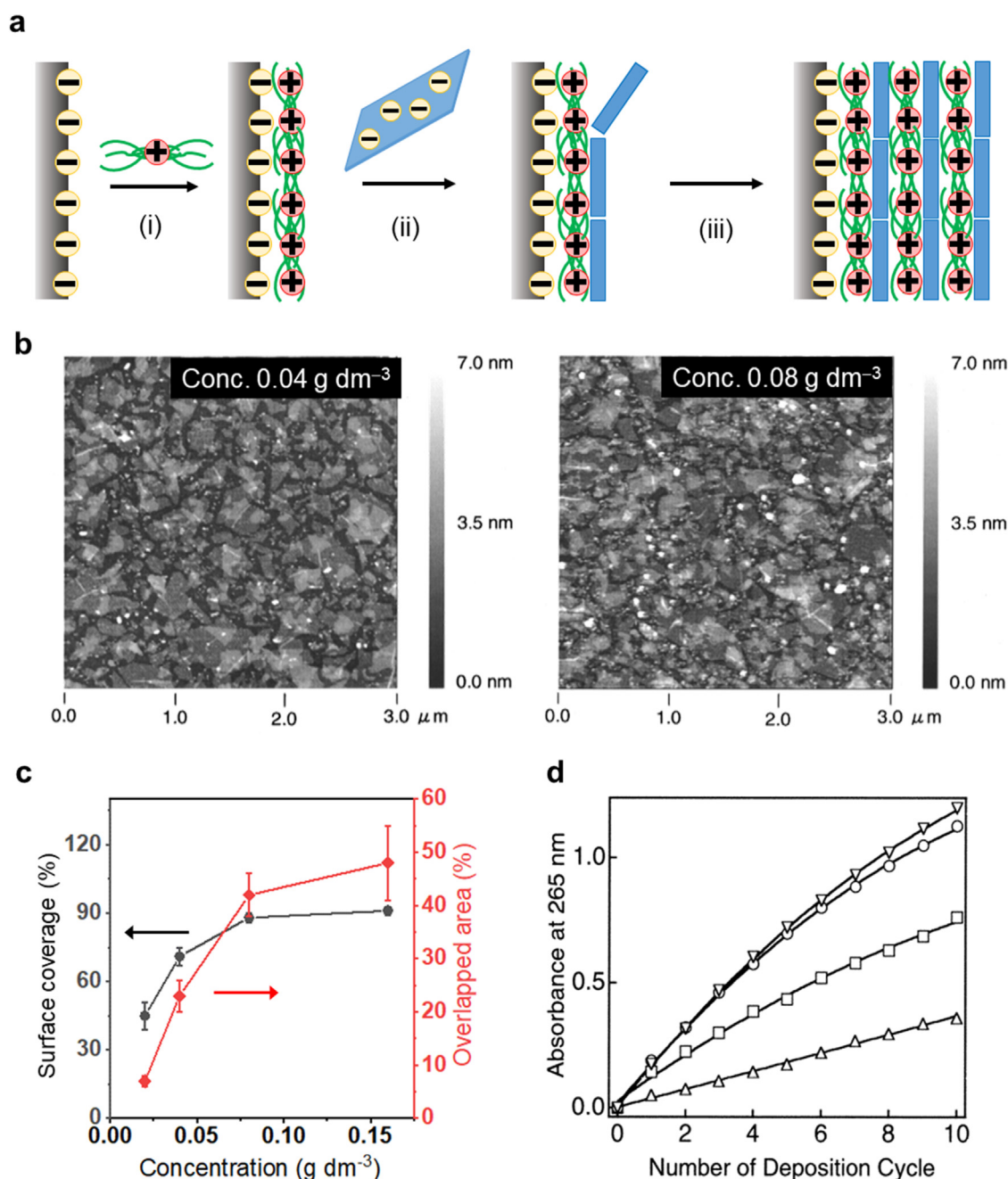
FIG. 9. Electrostatic LbL deposition method. (a) Mechanism for the LbL self-assembly. The process involves the adsorption of polycation molecules on a negatively charged substrate to modify the substrate surface (i) followed by the adsorption of negatively charged nanosheets (ii). Repeating this process results in the formation of a multilayer film composed of polycations and nanosheets (iii). (b) AFM image of the first layer of titania nanosheets deposited on a PEI-coated Si wafer for a 20 min immersion at nanosheet concentrations of 0.04 and 0.08 g dm^{-3}. (c) Surface coverage and overlapping area of the first layer of titania nanosheets deposited on PEI-coated Si wafers as a function of the dispersion concentrations of titania nanosheets. (d) Evolution of film absorbance as a function of deposition cycle from titania nanosheet dispersions at different concentrations: 0.02 (triangle), 0.04 (square), 0.08 (circle), and 0.16 (inverted triangle) g dm^{-3}. Panels (b) and (d) are reproduced with permission from Sasaki *et al.*, Chem. Mater. **13**, 4661 (2001). Copyright 2001 American Chemical Society. Panel (c) shows reprocessed data reported in Sasaki *et al.*, Chem. Mater. **13**, 4661 (2001). Copyright 2001 American Chemical Society.

on the LbL procedure have been conducted in terms of the suspension concentrations and the deposition time to optimize the surface coverage and overlapped area. A total coverage of $\sim$90% was achieved for a film of titania nanosheets with the lowest overlapping area of $\sim$40% using the optimized deposition parameters [Figs. 9(b), right and 9(c)].[139] UV-visible absorption spectroscopy is the most facile and efficient method to monitor the coverage of nanosheets after a single deposition cycle and their stepwise multilayer growth. If the nanosheet layer was uniformly deposited layer-by-layer, the absorbance linearly increased with the number of deposition cycles [Fig. 9(d)].

B. Langmuir–Blodgett deposition

The Langmuir–Blodgett (LB) technique can be employed to produce monolayer nanosheet films with dense packing and neat tiling quality. The LB method, well known to organic chemists, involves the formation of a monolayer of amphiphilic molecules at an air–water interface followed by its transfer onto the substrate in an appropriate manner. To the best of our knowledge, in 1998, the LB technique was first applied to 1T phase MoS_2 nanosheets obtained by the lithium intercalation method.[140] In that study, dihexadecyldimethylammonium bromide (DHA^+Br^-) was used as a cationic surfactant, where a DHA^+ monolayer formed at the air–water interface electrostatically attracts

negatively charged MoS_2 nanosheets to form a sparsely packed monolayer. By applying appropriate surface compression, floating nanosheets can be gathered to attain neat tiling and then readily transferred onto a substrate [Fig. 10(a)]. The same approach using an additional surfactant was employed for titania nanosheets.[141] Subsequently, Haga et al. found that the TBA^+ adsorbed on exfoliated metal oxide nanosheets could play a role as an amphiphilic surfactant floating them at the air–water interface.[142] Densely packed monolayer films of various oxide nanosheets, including $Ti_{0.91}O_2$ ($Ti_{0.87}O_2$),[142–144] $Ca_2Nb_3O_{10}$,[145,146] and $La_{0.95}Nb_2O_7$,[147] with a coverage of >95% were produced under optimized conditions, i.e., surface pressure and lifting speed [Fig. 10(b)]. The formation of gaps and overlaps is negligible in these cases, resulting in better film quality compared to those obtained by the aforementioned electrostatic LbL assembly. In addition, the construction of multilayer nanostructures with a precisely controlled film thickness is also possible by repeating the deposition procedure [Fig. 10(c)]. The LB technique was recently employed to deposit $Ti_3C_2T_x$ monolayer films.[148,149]

C. Spin coating

Spin coating is a conventional technique typically used in semiconductor manufacturing to fabricate thin layers of photoresist in photolithography processes due to its simplicity, versatility, and cost
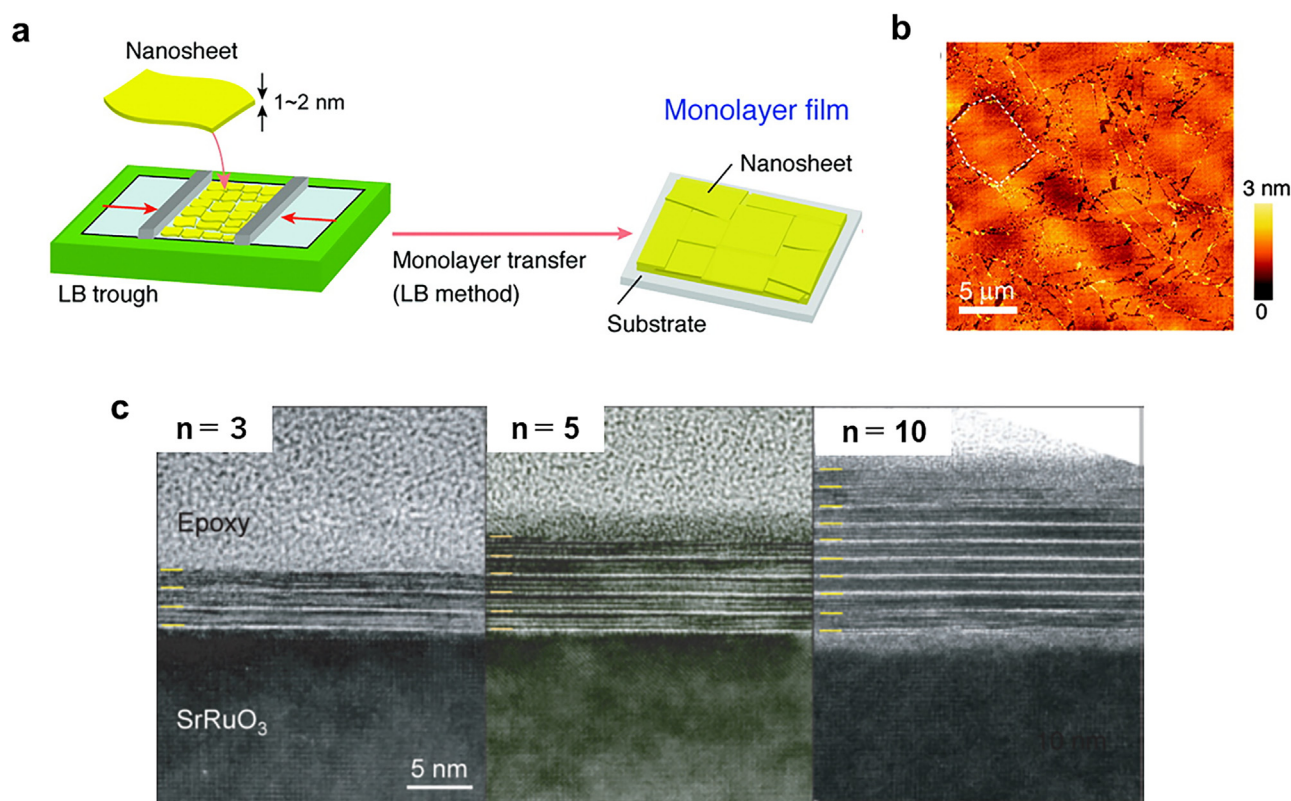
FIG. 10. LB method. (a) Scheme for the film fabrication of 2D nanosheets by the LB technique. (b) AFM image of the first layer of $Ca_2Nb_3O_{10}$ nanosheets. (c) Cross-sectional HRTEM images of the ($Ca_2Nb_3O_{10}$)$_n$ (n = 3, 5, 10) films on the $SrRuO_3$ substrate. Panel (a) and (b) are reproduced with permission from Li et al., ACS Nano **4**, 6673 (2010). Copyright 2010 American Chemical Society. Panel (c) is reproduced with permission from Osada et al., ACS Nano **4**, 5225 (2010). Copyright 2010 American Chemical Society.

effectiveness. The centrifugal force from the applied rotation spreads liquid drops evenly on the substrate, coating the substrate surface. Spin coating allows large-scale film coverage in a relatively short period of time (on the scale of minutes) without requiring complicated steps in fabrication. This method has been used to fabricate homogeneous thin films with nanosheet colloids. However, it generally produces films of bulk-scale thickness, making it unsuitable for the molecular-scale design of film architecture. On the contrary, in 2013, Kim *et al.* reported a spin coating technique for the fabrication of densely packed monolayer films of GO obtained by exfoliation with TBA.[150] We further found that dimethyl sulfoxide (DMSO) solvent in place of water plays a key role as a more robust medium to support spin coating of metal oxide nanosheets [Fig. 11(a)].[151] DMSO offers a proper viscosity and slow evaporation rate, which should, thus, spontaneously form a fluid layer in a convex shape when the liquid is loaded on the substrate, as illustrated in Fig. 11(b). In this state, the nanosheets are randomly oriented in their monodispersed forms. When

rotation is applied, the fluid flows to the substrate edge by centrifugal force, which changes the fluid outer form to a concave shape. TBA$^+$ ions contained in the suspension also play an important role in weakening the intersheet electrostatic interaction and preventing nanosheet aggregation due to a suitable charge-to-size ratio. Consequently, the individual nanosheets are aligned parallel to the substrate surface. The fluid layer becomes thinner and flat due to the continuous loss of the fluid during further spinning and eventually dried to form a densely packed nanosheet film. The single-layer coating can be completed within a few minutes. The process is much faster than the LB method, while the quality of the resultant film is almost identical. The repetition of the coating process allows multilayer buildup [Figs. 11(c) and 11(d)]. To date, monolayer deposition by spin coating has been adopted for metal oxide and GO nanosheets. Considering the analogy of surface chemistry, this facile method may be useful for obtaining high-quality TMDC and MXene nanofilms.
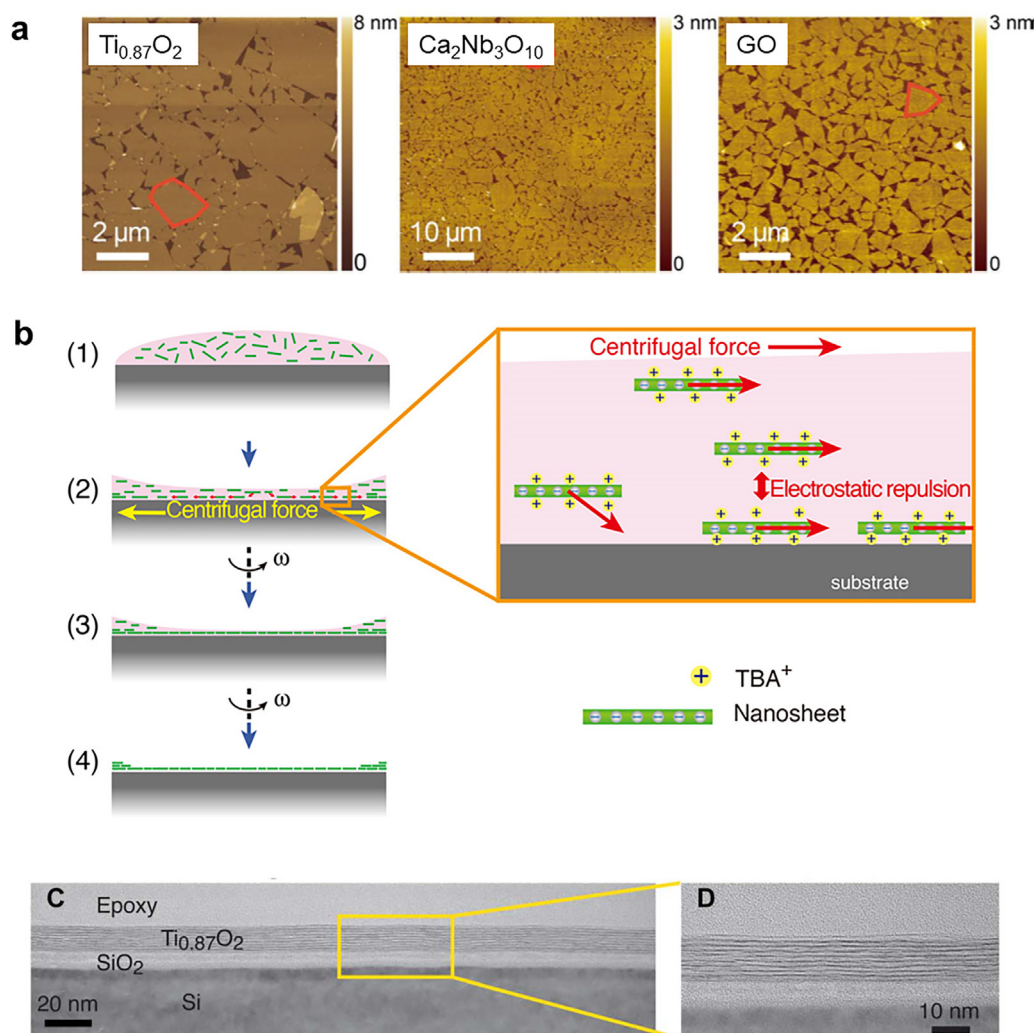
FIG. 11. Spin coating method. (a) AFM images of the monolayer films of nanosheets via spin coating of the suspensions. (b) A plausible model for the formation of the monolayer film of neatly tiled nanosheets. (c) and (d) Cross-sectional TEM images of the 10-layer film of Ti$_{0.87}$O$_2$. Reproduced with permission from Matsuba *et al.*, Sci. Adv. **3**, e1700414 (2017). Copyright 2017 Authors licensed under Creative Commons Attribution NonCommercial License 4.0 (CC BY-NC).

D. Drop casting

Drop casting is the simplest technique to fabricate films using colloidal ink. This technique works simply by loading the colloidal liquid on a substrate and allows it to dry under controlled conditions in terms of temperature, humidity, and ambient pressure. This strategy shares similar advantages with the spin coating method in terms of simplicity and cost-effectiveness. Previously, film fabrication by drop casting of colloidal suspensions generally suffered the coffee-ring effect;[152–155] a dark characteristic circle was formed by the uncontrolled accumulation of aggregates because a liquid is evaporated faster at the edge of the droplet than at the center. The difference in evaporation rates gives rise to capillary flows of the liquid from the droplet center to the pinned contact line at the droplet−substrate interface in the drying region, leading to the accumulation of the nanoparticles around the perimeter.[153]

Many attempts have been made to overcome the coffee-ring issue either by adjusting solvents,[156] adding additives,[157,158] tuning flake sizes,[159,160] or controlling deposition procedures.[161,162] For example, Kim et al. reported the use of higher-boiling-point solvents with lower surface tension, such as ethylene glycol, to enable a surface tension gradient that induces inward Marangoni flow to compensate for outward convective flow.[156] Jin et al. reported the successful fabrication of uniform MnO_2 films by drop casting aqueous dispersions of nanosized 2D flakes after the addition of a trace amount of ethanol.[157] The addition of ethanol is believed to tune the viscosity and surface tension of the MnO_2 suspension to achieve uniform deposition. Spin−controlled and ultrasonic-assisted drop casting have also been reported to reduce the formation of coffee rings, thus improving the quality of the deposited film.[161,163,164]

Drop casting has been frequently employed to obtain nanosheet-based films. However, the preparation of monolayer films has hardly been realized until recently. In 2021, a new strategy was developed to assemble monolayer films of neatly tiled 2D nanosheets via drop casting and sequential drying.[165] The assembly of nanosheets starts by introducing a single droplet on a heated substrate (100–120 °C) and then sucking up the liquid in an appropriate manner from the bottom center of the droplet [Fig. 12(a)]. A trace amount of ethanol as the additive is required to achieve densely packed 2D films. It was suggested that the deposition and arrangement of nanosheets are controlled by the thermal convection force during liquid withdrawal due to the generated surface tension gradient induced by heat treatment. The organization of neatly tiled nanosheets should accord with the co-occurrence of capillary and Marangoni flows, where the addition of a trace amount of ethanol helps to reduce the surface tension and enhance the Marangoni flows of their aqueous suspensions of 2D nanosheets. A variety of 2D nanosheets, such as $Ti_{0.87}O_2$, $Ca_2Nb_3O_{10}$, $Ru_{0.95}O_2$, $Cs_4W_{11}O_{36}$, and GO, have been successfully assembled [Figs. 12(b)–12(e)] into neatly tiled monolayer films. The repetition of the monolayer deposition produces multilayer films with precisely controlled layer numbers [Fig. 12(f)]. If the method is generalized for TMDC and MXene nanosheets, one can produce a high-quality nano-electronic device without any special deposition equipment.

E. Inkjet printing

It has been widely accepted that printed electronics potentially offer a new direction for low-cost electronic components and integrated systems fabricated on arbitrary substrates beyond the limit of conventional silicon-based semiconductor technologies. To date, various electronic devices, such as light-emitting diodes, field-effect transistors (FETs), photodetectors, and sensors, can be built by printing and patterning dispersion liquids of functional materials. One technique that can realize this direction is inkjet printing. The key point for the inkjet printing and patterning technique is the preparation and formulation of "appropriate" inks, where different inks are required to print different elements in a single component device. For instance, the fabrication of inkjet-printed FET devices requires three types of inks for patterning the semiconducting layers, dielectric layers, and conducting layers. Most of the 2D nanomaterials utilized for inkjet printing to date are prepared via ultrasonic exfoliation, which does not necessarily provide unilamellar nanosheets.[42,45,48,105,112,159] Thus, the molecular-scale design of inks and resultant devices has not been explored. In this review, we will not describe the detailed factors in the formulation of stable ink, as they have been comprehensively discussed elsewhere in the previous review report.[35] Although their discussion is to manipulate ink containing nanoflakes synthesized by ultrasonic exfoliation, the principles and concepts are applicable to nanosheet dispersions prepared by chemical exfoliation. In fact, Li et al. succeeded in preparing superconductor circuits and 3D structures by inkjet printing of monolayer TMDC ink prepared via chemical exfoliation.[115]

IV. APPLICATIONS FOR NANOELECTRONICS

In this chapter, we will discuss the electronic functionalities of nanofilms fabricated by the nanosheet deposition process described above. First, we will outline the advantages of this process in comparison with a conventional colloidal process using nanoparticles. Then, we will summarize the examples available thus far, emphasizing the importance of interface engineering to develop device functionalities.

Synthetic techniques for a range of nanoparticles have already been developed so that monodisperse nanoparticles are available for the precise design of various nanostructures.[166,167] Nevertheless, there remain critical drawbacks to applying nanoparticle assemblies to electronic devices such as transistors and transparent conductive films. Namely, the nanoparticles in the films must be chemically bonded to each other to afford conduction paths of mobile holes or electrons through the grain boundaries. For this purpose, postannealing of a nanoparticle-assembled film is needed. For example, annealing above 300 °C is at least necessary to give reasonable conductivity to films formed through the assembly of conducting nanoparticles such as indium tin oxides.[168–170] Thus, the nanoparticle assembly process is not suitable to fabricate conducting films on thermally unstable substrates such as plastics. In addition, the presence of dense grain boundaries between randomly oriented nanosized crystals detracts from the transport and mechanical properties of the resultant films. In this regard, there are several advantages of nanosheets over nanoparticles in device applications. First, two-dimensional nanosheets have a microscale lateral size, reducing the density of grain boundaries relative to the direction parallel to the substrate, i.e., the direction of carrier conduction. Second, the nanosheets in the film will adhere to each other face to face, resulting in higher electrical contact. Third, nanosheets, typically obtained from highly crystalline layered crystals, may have fewer defects than nanoparticles obtained by low-temperature solution-phase growth. In Secs. IV A–IV C, we will demonstrate that
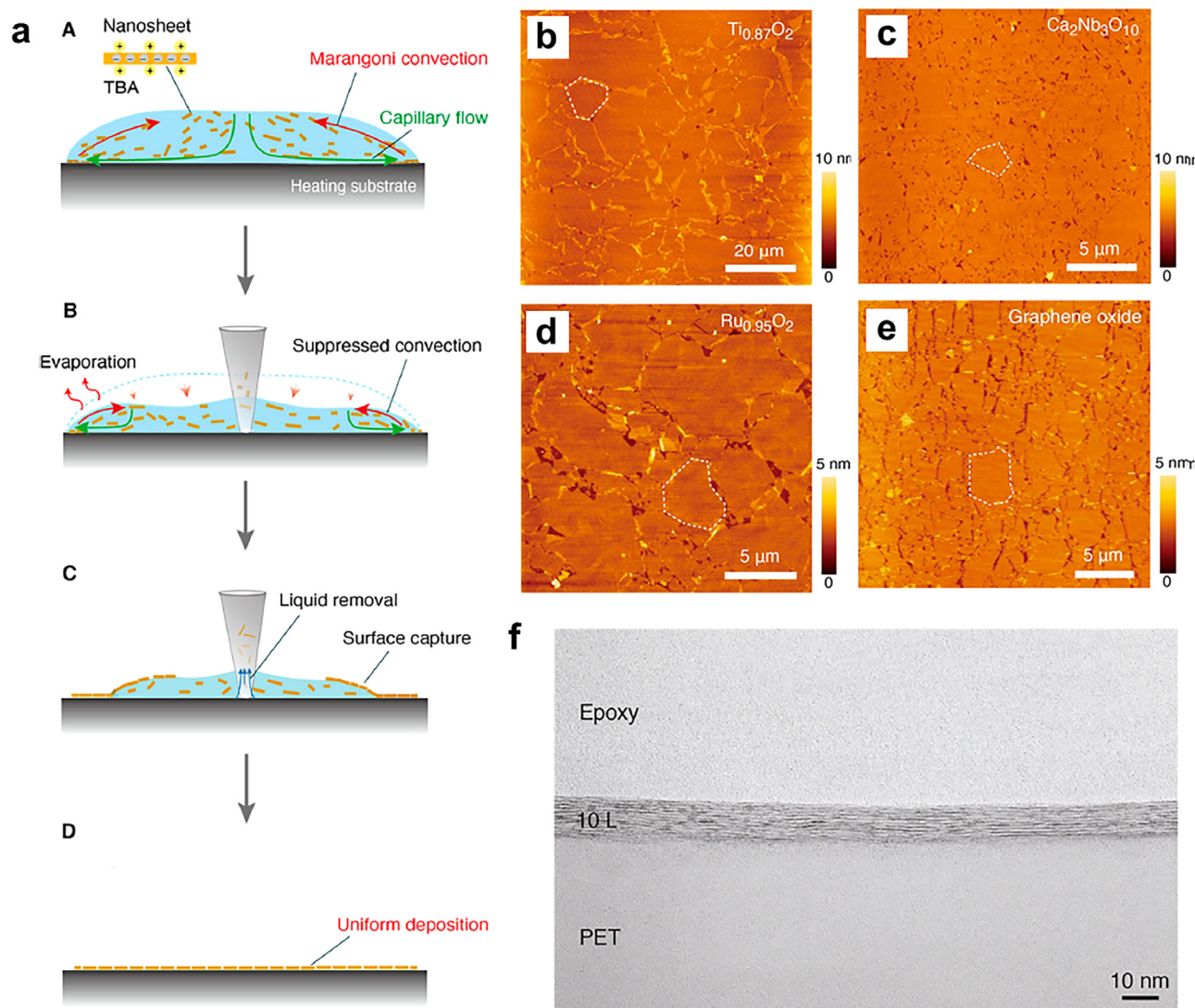
28 September 2023 06:36:42

FIG. 12. Drop casting method. (a) Procedure for single droplet assembly. (1) The height and contact angle of the sessile droplet decrease while maintaining the contact area between the droplet and substrate [(A) and (B)]. A concave surface between the center and edge parts of the droplet is formed (B). This concave surface implies the suppression of the Marangoni flow at the central part while retaining the Marangoni flow near the edge. (2) When the height of the droplet is reduced to a critical value, the contact area shrinks along with a reduced height of the residual droplet (C). After the removal of all the liquid, a neatly packed monolayer film is deposited (D). [(b)–(e)] Corresponding AFM images showing the quality of the monolayer films of $Ti_{0.87}O_2$, $Ca_2Nb_3O_{10}$, $Ru_{0.95}O_2$, and GO nanosheets. (f) Cross-sectional TEM images of the ten-layer film of $Ti_{0.87}O_2$. Reproduced with permission from Shi *et al.*, ACS Nano **14**, 15216 (2020). Copyright 2020 American Chemical Society.

these proposed advantages actually benefit the construction of various high-performance nanodevices.

A. Metal oxides

1. Dielectrics

Practical dielectric materials based on oxides have been developed and widely used. As described below, oxides in nanosheet forms also exhibit properties suitable for dielectrics. In this section, we will mainly outline the progress of oxide nanosheet-based dielectric thin films [Fig. 13(a)]. Recent reviews can provide details on the physical background and trends in recent research on 2D dielectric materials.[26,171] Titanium dioxide is well known as a photocatalyst, and this has been one of its important applications in nanosheet forms.[172,173] Dielectrics are another possible application of bulk titania and nanosheets. Anatase TiO_2 has a rather modest dielectric constant ($\varepsilon_r = 30$–40), while rutile TiO_2 exhibits a very high κ value (80–100), the highest among the binary oxides. We reported titania nanosheets as the first high-k dielectric nanosheet in 2006.[25] The five-layered film
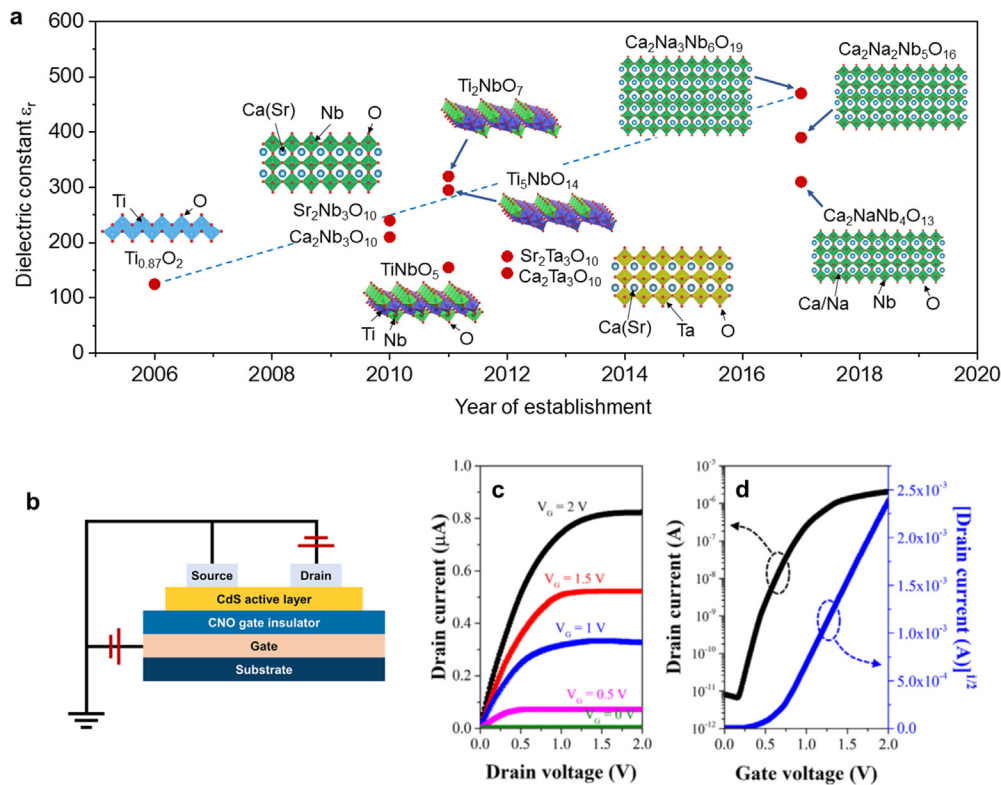
28 September 2023 06:36:42

FIG. 13. Dielectric applications of oxide nanosheets. (a) Dielectric constants of oxide nanosheets plotted with the year first reported. (b) Schematic of the CdS-TFT structure with the $Ca_2Nb_3O_{10}$ (CNO) gate insulator. (c) Output characteristics (I_{sd}–V_{ds}) and (d) transfer characteristics (I_{sd}–V_g) curves (left axis) and the square root of the IDS–VGS curves (right axis) of the CdS-TFT devices with the $Ca_2Nb_3O_{10}$ dielectric layer. Reproduced with permission from Kang *et al.*, Appl. Surf. Sci. **476**, 374 (2019). Copyright 2019 Elsevier.

of $Ti_{0.87}O_2$ nanosheets with a thickness of only 5 nm, prepared using the electrostatic LbL method, exhibited both a low leakage current density ($<10^{-7}$ A/cm^2 at 1 V) and a high dielectric constant (ε_r:120). This excellent performance also relies on the absence of pinholes across the entire film and grain boundaries that allow vertical electron transport. In addition, the high dielectric property indicates the nanosheets themselves being free from any extrinsic defects.

Following the successful application of titania nanosheets in nanodielectrics, various oxide nanosheets were studied for their dielectric properties and progressive enhancement was achieved. It should be noted that the LB process was established after the initial study with titania nanosheets, significantly improving the quality of available thin films. As a result, the LB method has been used to fabricate metal-insulator-metal (MIM) devices for tests of dielectric performance in subsequent studies. The second family, reported in 2011, consists of titanoniobate nanosheets ($TiNbO_5$, Ti_2NbO_7, and Ti_5NbO_{14}).[174] In these nanosheets, molecular polarizability is remarkably enhanced due to octahedral promoted distortion by incorporation of Nb into the host framework. As a result, high ε_r values (155–320) and high insulating properties (10^{-6}–10^{-8} A/cm^2 at 1 V) could be obtained in the multilayer stacked nanofilms. Perovskite nanosheets, as the third family, have received much attention since 2009. Initially, the $Ca_2Nb_3O_{10}$ nanosheet film demonstrated a stable dielectric response of up to 10 GHz with a dielectric constant of ~200,[145] which is the highest among ultrathin high-κ perovskites (<10 nm). Moreover, the

nanosheet films realized a high capacitance density (~20 μF/cm^2), insulating properties ($<10^{-7}$ A/cm^2 at 1 V), and a strong breakdown field (~6 MV/cm), and robust thermal stability up to 250 °C in the dielectric properties.[175] Subsequently, it was demonstrated that perovskite-based solid-solution nanosheets, $(Ca_{1-x}Sr_x)_2(Nb_{1-y}Ta_y)_3O_{10}$, improved the insulating characteristics with an enlarged bandgap and increased breakdown voltage.[176] In addition to traditional A- and B-site engineering to tailor dielectric properties in perovskite oxides, an elegant approach was found in 2D homologous perovskite nanosheets $(Ca_2Na_{m-3}Nb_mO_{3m+1}; m = 3–6)$.[90] In this system, increasing the number m incrementally controls the perovskite layer thickness at a step of NbO_6 octahedron (0.4 nm). Simultaneously, the polarizability is engineerable by such thickness control at the unit-cell level, yielding the highest dielectric constant of ~470 with the $m = 6$ member $(Ca_2Na_3Nb_6O_{19})$.[177] In that study, a room-temperature ferroelectric nanosheet, $Ca_2Na_2Nb_5O_{16}$ with an odd m number of 5, was discovered, although the other dielectric nanosheets listed above are paraelectric at room temperature. Instead of the LB method, a drop casting method, recently developed as the simplest method to perform monolayer-level deposition, was used for the fabrication of dielectric nanosheet films.[21] The ten-layer titania nanosheet films produced by this method exhibited both a high dielectric constant ($\varepsilon_r \sim 120$) and low leakage current density ($<10^{-8}$ A cm^{-2}), comparable to those observed in the films fabricated by the electrostatic LbL method followed by ultrasonic treatment.

The dielectric constants (ca. 100–500) of oxide nanosheet films are much larger than that of HfO_2 (ε_r:24), a typical high-κ gate insulator used for a state-of-the-art complementary metal-oxide semiconductor. In addition, the processable thickness of the HfO_2 dielectric layers is limited to ca. 2 nm because a thinner film cannot be used as an insulating layer owing to the large current leakage. Thus, ultrathin films based on oxide nanosheets will serve as the next generation dielectric layers that will be required for Moore's law to be followed in future semiconductor technology. Recently, Kang et al. studied the potential of $Ca_2Nb_3O_{10}$ as a gate insulator.[178] MIM structures, including the LB-deposited CNO film (ca. 17 nm), showed an acceptable leakage current density of 7.26×10^{-7} A cm^{-2} at 2 V, a very high capacitance density of 944 nF cm^{-2}, and good stability of capacitance with respect to voltage. To fabricate the thin film transistor (TFT) devices, simple solution deposition methods were used to deposit a CdS active layer at a low temperature [Fig. 13(b)]. The resulting TFTs displayed a carrier mobility of 0.428 cm^2 V^{-1} s^{-1}, ON/OFF current modulation of 10^6, the threshold voltage of 0.596 V, and subthreshold slope of 0.05 V dec^{-1} at an operating voltage of 2 V [Figs. 13(c) and 13(d)]. Thus, an ultrathin $Ca_2Nb_3O_{10}$ gate insulator would be a promising component in thin film transistors for low-voltage operations.

It is important to note that organic species are accommodated in the interlayer gallery of the as-deposited films. These include organo-ammonium cations such as TBA used for exfoliation and polycations such as PDDA used for LbL deposition. The photocatalytic activity of oxide nanosheets promotes the decomposition of such organics by exposing the assembled multilayer films to UV light.[91] Additionally, UV-O_3 cleaning is effective in the removal of organic residue from oxide nanosheet films because of the structural robustness of nanosheets against oxidation. Excellent dielectric properties are generally obtained after this elimination, yielding fully dense nanosheet films. Thermal calcination is also a common way to eliminate organic species owing to the high thermal stability of oxide nanosheets over 400 °C,[179,180] although this method cannot be adapted to produce plastic-based flexible devices.

2. Optoelectronics

The highly insulating property of metal oxide nanosheets, which enables the aforementioned dielectric applications, is based on the wide gap nature. Wide bandgap materials are suitable as ultraviolet photodetectors (UV PDs) that have continuously attracted attention in many fields, such as space exploration, biological analysis, environmental sensors, communication, and imaging. For decades, numerous UV PDs based on traditional wide-bandgap oxides (ZnO,[181] TiO$_2$,[182] Ga$_2$O$_3$,[183] etc.) have been extensively investigated. An ideal PD is generally expected to have high sensitivity, fast response speed, high spectral selectivity, and high stability. Dense and highly crystalline thin films, the fabrication of which requires calcination or annealing steps, are needed to realize this superior performance. Such annealing at high temperatures is not applicable to fabricating flexible PDs deposited on plastic substrates. Thus, oxide nanosheets with wide bandgaps and their colloidal processing without a heating process should be suitable for developing flexible UV PDs. The first application of oxide nanosheets for UV PDs was demonstrated with titania nanosheets in 2015 [Fig. 14(a)].[184] Under UV light illumination of a single titania nanosheet device, a finite photocurrent was observed as shown in

Fig. 14(b). The device exhibited a fast switching between the ON current (5.8 pA) and OFF current (<0.1 pA), where the ON/OFF ratio was larger than 50. The rise time and the fall time of the photoresponse were shorter than the measurement limit of the experimental setup (0.2 s). The fast photoresponse of the device implies a small number of carrier trapping sites in the single crystal structure of the titania nanosheet.

The 2D perovskites $Ca_2Nb_3O_{10}$ (Ref. 185) and $Sr_2Nb_3O_{10}$ (Ref. 186) were then examined by Feng et al. in 2020. $Ca_2Nb_3O_{10}$ PDs showed high performance at 3 V at 280 nm, high responsivity (14.94 A W^{-1}), high detectivity (8.7×10^{13} Jones), high spectral selectivity (8.84×10^3), fast speed (0.08/5.6 ms), and long-term stability, exceeding those of most UV PDs reported [Figs. 14(c)–14(e)]. The high photoresponse supports the hypothesis that 2D interfaces between nanosheets are more suitable than 3D interfaces between nanoparticles for in-plane carrier transport. Additionally, annealing at 200 °C was performed as the final step for device fabrication. In general, this temperature is insufficient to obtain reasonable device performance if sol-gel and nanoparticle assembly methods are employed. Thus, 2D boundaries between nanosheets might exhibit fewer carrier scattering sites than those between randomly oriented nanocrystals. The $Sr_2Nb_3O_{10}$ nanosheet-based PDs also exhibited excellent UV detection performance equal to that of $Ca_2Nb_3O_{10}$. A simple drop-coating method was used to fabricate flexible $Sr_2Nb_3O_{10}$ film PDs on a PET substrate without the use of any additional additives [Fig. 14(f)]. The flexible PD could show the photocurrent value nearly unaltered with a bending angle up to 80° [Fig. 14(g)].

Ultrathin and wide bandgap oxide nanosheets with excellent photoconductivity and photostability can be used as components of a wide range of optoelectronic devices. As an example, Chang et al. reported that $Ca_2Nb_3O_{10}$ nanosheets were used as an electron-transporting layer (ETL) in solution-processed tandem polymer solar cells.[187] $Ca_2Nb_3O_{10}$ nanosheet-based ETL devices showed a higher photon-to-current efficiency (PCE), compared with devices consisting of conventional TiO$_x$, [Figs. 15(a) and 15(b)]. Ohisa et al. reported the application of $Ca_2Nb_3O_{10}$ nanosheets for electron injection layers (EILs) in organic light-emitting devices (OLEDs) [Fig. 15(c)].[188] $Ca_2Nb_3O_{10}$ nanosheets were expected to be effective as EILs due to their dielectric characteristics capable of generating large electric polarization in an electric field. Organic light-emitting polymer-based devices with fluorescent poly[(9,9-di-n-octylfluorenyl-2,7-diyl)-alt-(benzo[2,1,3]-thiadiazol-4,8-diyl)] (F8BT) and $Ca_2Nb_3O_{10}$ nanosheet EILs showed the lower driving voltages than those with the lithium eight-quinolate EIL material [Figs. 15(d) and 15(e)]. The coverage of the $Ca_2Nb_3O_{10}$ nanosheets, their thicknesses, and their work function values were interrelated to affect the performance of OLEDs. In addition, Chen et al. used titania nanosheets in organic–inorganic lead halide perovskite solar cells.[189] They assumed that the unique features of titania nanosheets such as high UV transparency and negligible oxygen vacancies were beneficial as an electron-transporting material to produce high-performance perovskite solar cells with high stability. In fact, the titania nanosheets resulted in superior inhibition of UV degradation of perovskite solar cells compared with the conventional TiO$_2$ counterpart, which is notoriously unstable under UV irradiation [Figs. 15(f) and 15(g)]. In their subsequent study, the suggested mechanism for the origin of extended UV stability was further supported by ultrafast spectroscopy.[190] These successful case studies show great
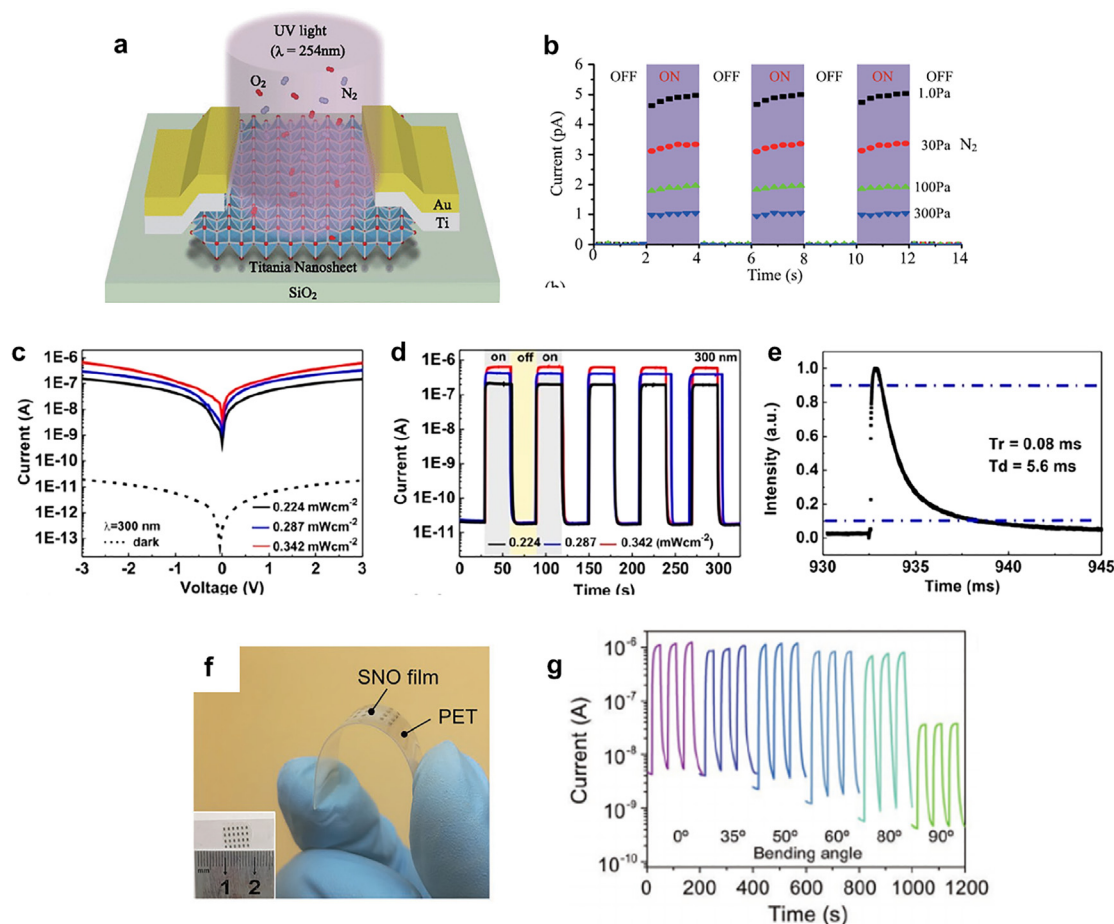
FIG. 14. Photodetector applications of oxide nanosheet. (a) Schematic illustration of the photodetector consisting of a single titania nanosheet. (b) UV photoresponse of single titania nanosheet PD under various N_2 pressures. Reproduced with permission from Matsuzaki et al., Appl. Phys. Lett. **106**, 033104 (2015). Copyright 2015 AIP Publishing. (c) I − V curves for $Ca_2Nb_3O_{10}$ PD with different incident power densities. (d) I−t curves for the device under 300 nm light switching. (e) The normalized pulse response of the device. Reproduced with permission from Zhang et al., Nano. Lett. **21**, 382 (2021). Copyright 2021 American Chemical Society. (f) Image of flexible $Sr_2Nb_3O_{10}$ (SNO) PD on a PET substrate. (g) The I–t curves under 300 nm UV switching (0.39 mW cm^{-2}) at a 1 V bias, measured at various bending angles. Reproduced with permission from Li et al., Adv. Mater. **32**, 1905443 (2020). Copyright 2020 Wiley-VCH.

promise for oxide nanosheets in the fabrication of large-area photovoltaic or optoelectronic devices based on solution processes.

3. Spintronics

Spintronics using ferromagnetic nanosheets has been a recent topic in the field of 2D nanomaterials science. In the past three years, ferromagnetism has been found in nanosheets obtained by mechanical exfoliation of vdW crystals such as CrI_3 (Ref. [191]) and Fe_3GeTe_2.[192] However, these nanosheets are not suitable for practical devices because their Curie temperatures are below 230 K. Indeed, they cannot be handled in the air due to their high reactivity with water and oxygen. On the other hand, since 2006 and long before the discovery of ferromagnetism from exfoliated vdW crystals, we have found room-temperature ferromagnetism in TiO_2 nanosheets doped with magnetic sources such as Co, Fe, and Mn [Fig. 16(a)].[193–195] It is well known that anatase and rutile can act as transparent magnets when doped with these magnetic elements.[196]

Using nanosheets as a 2D nanobuilding block, magnetic devices that integrate both ferromagnetic and semiconducting properties can be realized. One of them is the magneto-optical effect, which is used to rotate the polarization plane of light by magnetism (spin). Figure 16(b) shows the magneto-optical spectra of $Ti_{0.8}Co_{0.2}O_2$ nanosheet multilayers deposited by the LBL method. Magnetic-field-dependent magnetic circular dichroism (MCD) and magnetization showed ferromagnetic responses at ambient temperature [Fig. 16(c)]. The 2D nature of the electronic state of ferromagnetic nanosheets leads to a large MO response, superior to that of bulk systems.[83] Furthermore, (Co/Fe)-co-doped titania nanosheets, $Ti_{0.8-x/4}Fe_{x/2}Co_{0.2-x/4}O_2$ (x = 0.2, 0.4, 0.6) showed an enhanced MO response ($\sim 2 \times 10^5$ °/cm) in the range of 400–750 nm [Figs. 16(d) and 16(e)].[197]

4. Transparent conductors

The above applications of oxide nanosheets are based on their wide bandgap. On the other hand, RuO_2 (Ref. [79]) and MoO_2
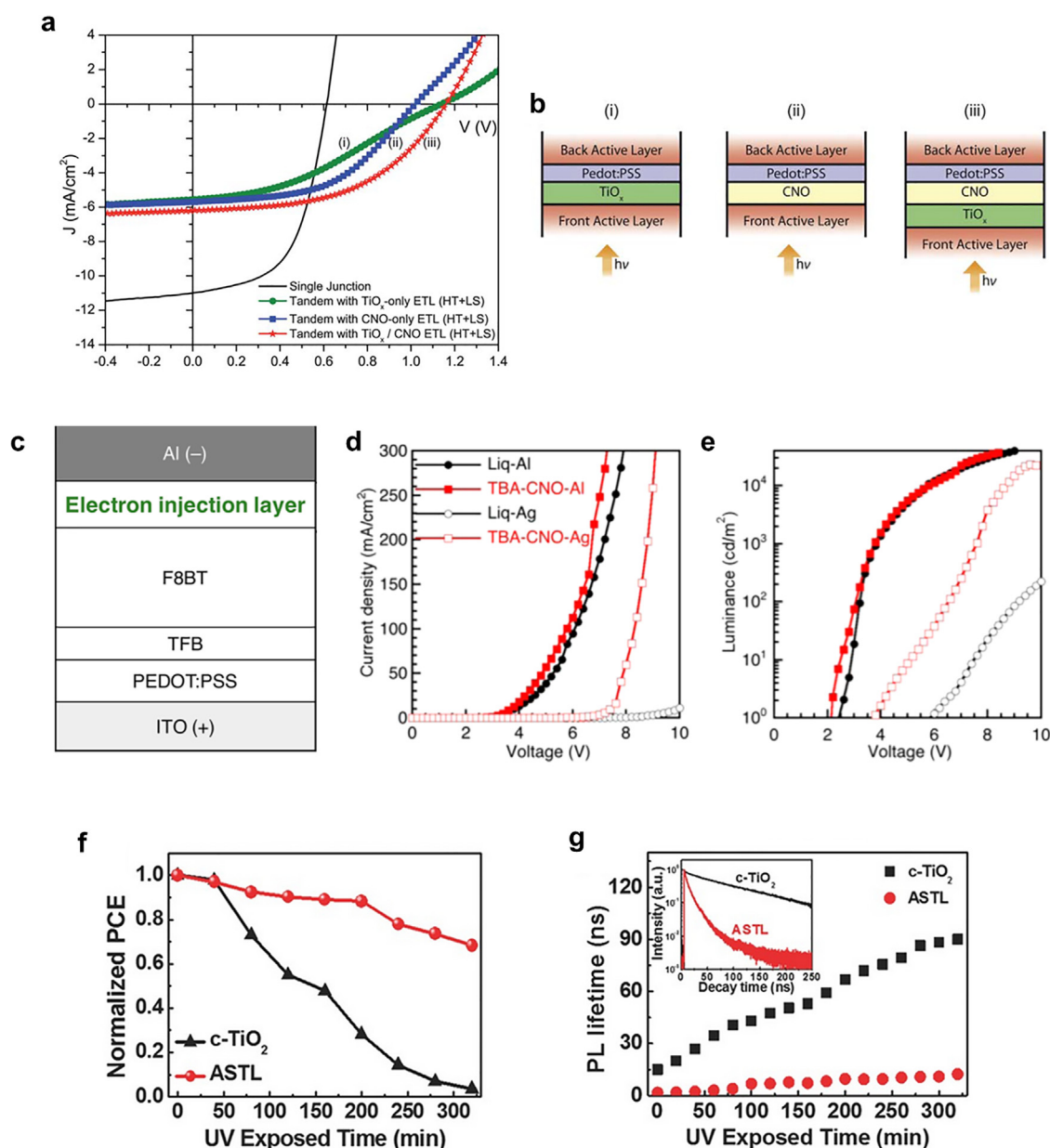
FIG. 15. Photoconversion applications of oxide nanosheets. (a) J–V curve (under illumination) comparing a P3HT:PCBM single junction device to various tandem devices with different ETLs depicted in (b). Reproduced with permission from Chang *et al.*, J. Mater. Chem. **22**, 20443 (2012). Copyright 2012 The Royal Society of Chemistry. (c) Structure of organic light-emitting devices, where $Ca_2Nb_3O_{10}$ is used as the electron injection layer, F8BT {fluorescent poly[(9,9-di-n-octylfluorenyl-2,7-diyl)-alt-(benzo[2,1,3]-thiadiazol-4,8-diyl)]}, TFB [poly(9,9-dioctyl-fluorene-co-N-(4-butylphenyl)-diphenylamine]. (d) Current density−voltage and (e) luminance−voltage characteristics of devices with Liq or TBA−$Ca_2Nb_3O_{10}$ EIL, using Al or Ag electrodes. Reproduced with permission from Ohisa *et al.*, ACS. Appl. Mater. Interfaces **10**, 27885 (2018). Copyright 2018 American Chemical Society. (f) Evolution of the normalized PCEs of perovskite solar cells consisting of a polycrystalline TiO_2 ETL (c-TiO_2) and titania nanosheet ETL (ASTL) under 5 h irradiation. (g) The corresponding time-resolved photoluminescence lifetime for the perovskite films deposited on c-TiO_2 and ASTL as a function of UV irradiation time. Reproduced with permission from Chen *et al.*, Adv. Energy. Mater. **8**, 1701722 (2018). Copyright 2018 Wiley-VCH.

(Ref. [198]) nanosheets offer high electrical conductivity. Among them, progress has been made in the transparent conductive film applications of RuO_2. In an early study, Sato *et al.* measured the sheet resistance of an isolated single RuO_2 nanosheet to be $12\,k\Omega\,sq^{-1}$ by means

of scanning probe microscopy.[199] In the same work, they also examined the conducting behaviors of ultrathin films with submonolayer to monolayer RuO_2 coverage. At coverage exceeding 70%, submonolayer films behaved as a continuous conducting film. The electron transport
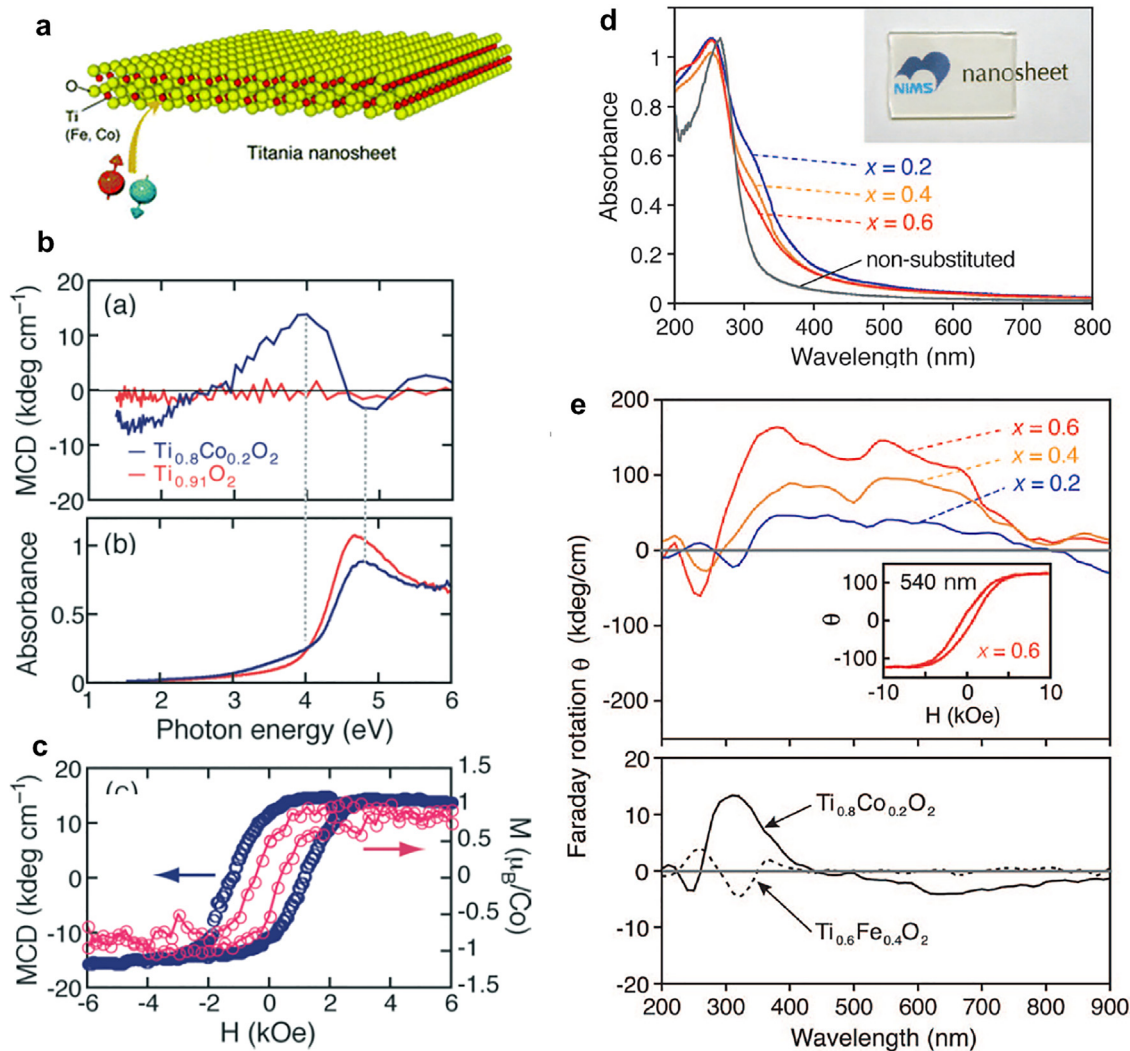
FIG. 16. Magneto-optical effect of ferromagnetic oxide nanosheets. (a) Crystal structure of Fe- and Co-doped titania nanosheets. (b) Polar Kerr MCD spectra measured at 10 kOe and 300 K for $(PDDA/Ti_{0.8}Co_{0.2}O_2)_{10}$ and $(PDDA/Ti_{0.91}O_2)_{10}$. (c) MCD signal at 4.1 eV and magnetization as a function of the applied field, measured at 300 K. Reproduced with permission from Osada et al., Adv. Mater. **18**, 295 (2006). Copyright 2006 Wiley-VCH. (d) Optical absorption spectra for $(PDDA/Ti_{0.8-x/4}Fe_{x/2}Co_{0.2-x/4}O_2)_{10}$, $x = 0.2$, 0.4, and 0.6 and $(PDDA/Ti_{0.91}O_2)_{10}$ on quartz glass substrates. The inset shows a photograph of the $(PDDA/Ti_{0.75}Fe_{0.1}Co_{0.15}O_2)_{10}$ film. (e) Faraday rotation spectra of $(PDDA/Ti_{0.8-x/4}Fe_{x/2}Co_{0.2-x/4}O_2)_{10}$ $x = 0.2$, 0.4, and 0.6, $(PDDA/Ti_{0.8}Co_{0.2}O_2)_{10}$ and $(PDDA/Ti_{0.6}Fe_{0.4}O_2)_{10}$. The inset shows the magnetic field dependence of the Faraday rotation intensity for $(PDDA/Ti_{0.75}Fe_{0.1}Co_{0.15}O_2)_{10}$ measured at 540 nm at RT. Reproduced with permission from Osada et al., Appl. Phys. Lett. **92**, 253110 (2008). Copyright 2008 AIP Publishing.

mechanism was described based on a 2D percolation model. Furthermore, multilayered films prepared by LbL deposition showed a resistivity of less than $1 k\Omega sq^{-1}$ [Fig. 17(a)]. Wang et al. also studied the resistivity of two-layer and five-layer films deposited by the LbL technique, affording a highly conducting nature with room-temperature sheet resistances of ~ 4.1 and $\sim 0.9 k\Omega sq^{-1}$, respectively.[200] Ko et al. reported that LB-deposited RuO_2 films with two layers and four layers have sheet resistances of 8.3 and $3.2 k\Omega sq^{-1}$ with optical transparencies of 97.2% and 93.4% in the visible region, respectively.[201] The transparency–resistivity relationships of RuO_2 nanosheet films are superior to solution processed GO-based

transparent conducting films, whereas the current CVD-graphene shows approximately one order magnitude lower resistivity with transparency above 95%.[202]

Several efforts have been made to reduce the resistivity of RuO_2 nanosheet films. Yun et al. studied washing a RuO_2 nanosheet layer prepared by a bar coating method,[203] as the presence of contaminants at the interface region may suppress a layer-to-layer electron transport. They found that a simple water-cleaning treatment considerably increased the work function of RuO_2 nanosheets to improve conductivity [Fig. 17(b)]. As another technique to tailor the electrical conductivity of RuO_2 nanosheets, Yoo et al. employed silver photodeposition
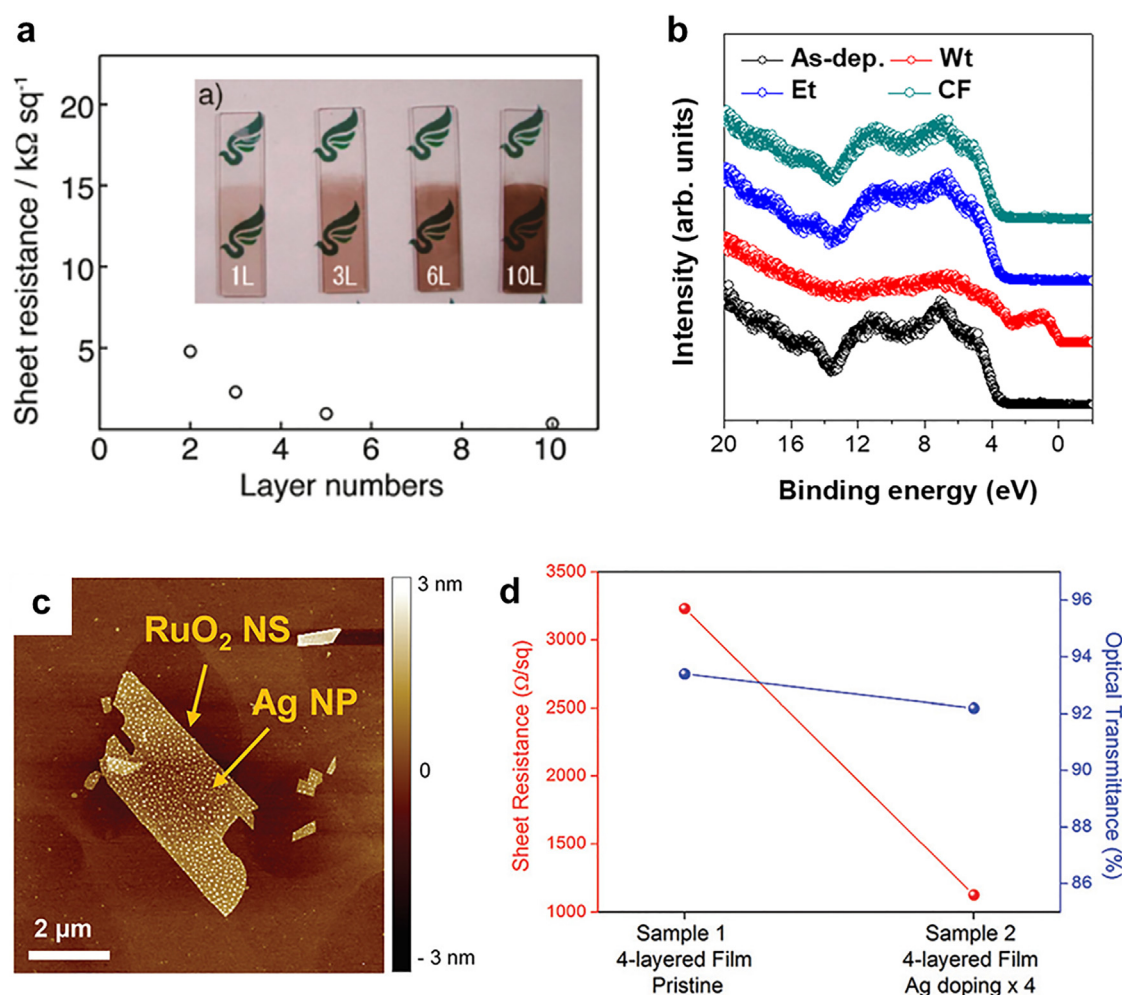
FIG. 17. RuO$_2$ nanosheet as a transparent conductor. (a) Sheet resistance and digital photoimages of the self-assembled multilayer films of RuO$_2$ nanosheets as a function of layer number. Reproduced with permission from Sato *et al.*, Langmuir **26**, 18049 (2010). Copyright 2010 American Chemical Society. (b) Valence band spectra of the solution-treated RuO$_2$; Wt (water), Et (ethanol), and CF (chloroform). Reproduced with permission from Yun *et al.*, Appl. Surf. Sci. **529**, 147154 (2020). Copyright 2020 Elsevier. (c) Topographic AFM image of an Ag-deposited RuO$_2$ nanosheet on a Si/SiO$_2$ substrate. (d) The sheet resistance and optical transmittance of the RuO$_2$ nanosheet multilayer films with/without Ag deposition. Reproduced with permission from Hwang *et al.*, Nanoscale **9**, 7104 (2017). Copyright 2017 The Royal Society of Chemistry.

[Fig. 17(c)].[204] The four-layer films of RuO$_2$ nanosheets decorated with Ag nanoparticles exhibited resistance and optical transmittance of $\sim$1.1 kΩ sq^{-1} and $\sim$92.2% in the visible region, respectively, whereas the pristine films of RuO$_2$ nanosheets showed higher resistivity (3.2 kΩ sq^{-1}) and comparable transparency ($\sim$93.4%) [Fig. 17(d)]. Furthermore, they demonstrated excellent stability upon bending, with resistance changes of less than 1% after 50 000 bending cycles.

5. Heteroassembly of 2D oxide nanosheets

The broad combination of integrating distinct monolayers into vertical heterostructures can afford synergistic coupling of disparate properties. In the past half-decade, this concept has been extensively demonstrated with vdW heterostructures,[16,18] while controlled and emergent functionalities by such heteroassembly had already been

found in artificial superlattices based on oxide nanosheets approximately 15 years ago. As the first example, it was reported in 2006 that the superlattice assemblies of Ti$_{0.8}$Co$_{0.2}$O$_2$ and Ti$_{0.6}$Fe$_{0.4}$O$_2$ nanosheets showed an enhanced MCD response by interlayer coupling [Figs. 18(a) and 18(b)],[193] which stems from the interlayer d–d transitions (Co^{2+}–Fe^{3+}) between adjacent nanosheets.[205] To date, various oxide nanosheets have been successfully integrated into superlattice heterostructures with intriguing functionalities arising from the synergistic coupling. For example, heterojunctions of semiconducting Ti$_{0.91}$O$_2$ and redoxable MnO$_2$ nanosheets showed a unique photochemical function upon UV light irradiation [Figs. 18(c) and 18(d)].[206] MnO$_2$ nanosheets underwent reduction (Mn^{4+} to Mn^{3+}), which is ascribed to the injection of photoexcited electrons generated in Ti$_{0.91}$O$_2$ into MnO$_2$ nanosheets. Artificial superlattices of paraelectric pairs such Ca$_2$Nb$_3$O$_{10}$/LaNb$_2$O$_7$ (Ref. 147) and Ca$_2$Nb$_3$O$_{10}$/
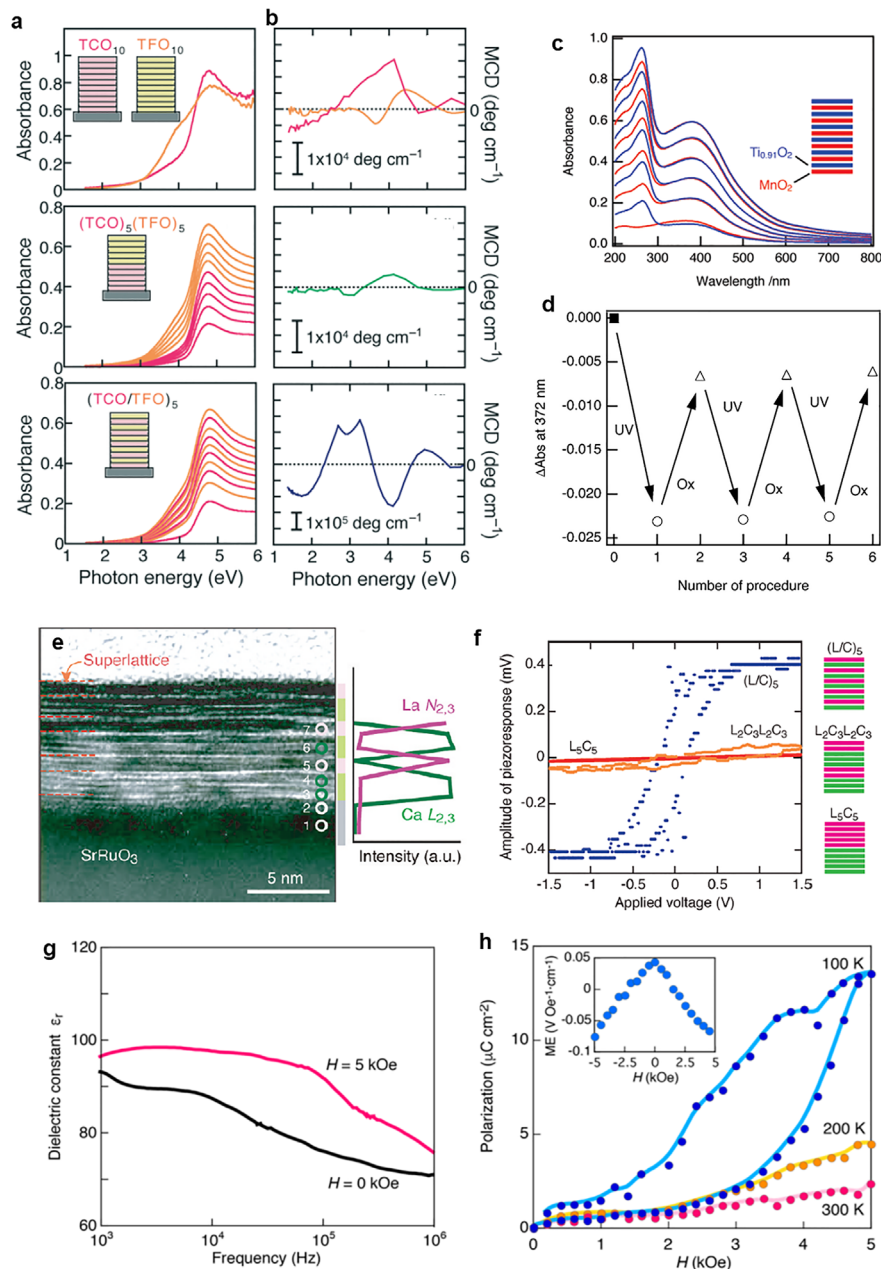
28 September 2023 06:36:42

FIG. 18. Heterostructures based on oxide nanosheets. (a) Optical absorption spectra and (b) MCD spectra of multilayer assemblies of parent nanosheets, (PDDA/$Ti_{0.8}Co_{0.2}O_2$)$_{10}$:[TCO$_{10}$] and (PDDA/$Ti_{0.6}Fe_{0.4}O_2$)$_{10}$:[TFO$_{10}$] and superlattice, (PDDA/$Ti_{0.8}Co_{0.2}O_2$)$_5$(PDDA/$Ti_{0.6}Fe_{0.4}O_2$)$_5$:[TCO$_5$TFO$_5$] and (PDDA/$Ti_{0.8}Co_{0.2}O_2$/PDDA/$Ti_{0.6}Fe_{0.4}O_2$)$_5$:[(TCO/TFO)$_5$]. The build-up process monitored by UV-visible absorption spectroscopy confirms the superlattice-type buildup. Reproduced with permission from Osada et al., Adv. Mater. **18**, 295 (2006). Copyright 2006 Wiley-VCH. (c) UV-visible absorption spectra in the multilayer buildup process of $Ti_{0.91}O_2$ and MnO$_2$ nanosheet composite films. Red lines: spectra for the films after deposition of MnO$_2$ nanosheets; blue lines: spectra for the films after deposition of $Ti_{0.91}O_2$ nanosheets. (d) Optical absorption changes at 372 nm for $Ti_{0.91}O_2$/MnO$_2$ nanosheet composite films: as-grown film (closed square) after UV irradiation (open circles) and after anodic oxidation at +1.0 V (open triangles). Reproduced with permission from Sakai et al., J. Phys. Chem. C **112**, 5197 (2008). Copyright 2008 American Chemical Society. (e) HRTEM image and integrated intensity profiles of the La-$N2,3$ and Ca-$L2,3$ edges of the (LaNb$_2$O$_7$/Ca$_2$Nb$_3$O$_{10}$)$_3$ superlattice on the SrRuO$_3$ substrate. (f) Piezo-response microscopy responses measured from different superlattices: (LaNb$_2$O$_7$/Ca$_2$Nb$_3$O$_{10}$)$_5$: [(L/C)$_5$], (LaNb$_2$O$_7$)$_2$(Ca$_2$Nb$_3$O$_{10}$)$_3$(LaNb$_2$O$_7$)$_2$(Ca$_2$Nb$_3$O$_{10}$)$_3$: [L$_2$C$_3$L$_2$C$_3$], and (LaNb$_2$O$_7$)$_5$(Ca$_2$Nb$_3$O$_{10}$)$_5$: [L$_5$C$_5$]. Reproduced with permission from Li et al., ACS Nano **4**, 6673 (2010). Copyright 2010 American Chemical Society. (g) Frequency dependence of the dielectric constant (ε_r) for [($Ti_{0.8}Co_{0.2}O_2$)$_2$/Ca$_2$Nb$_3$O$_{10}$]$_2$/($Ti_{0.8}Co_{0.2}O_2$)$_2$ on a SrRuO$_3$ substrate under a magnetic field. The magnetic field is normal to the film surface. The measurements were recorded at 300 K. (h) Magnetic-field control of electric polarization (P$_r$) of the same film sample measured at 100, 200, and 300 K. The magnetic field is normal to the film surface. Reproduced with permission from Li et al., J. Am. Chem. Soc. **138**, 7621 (2016). Copyright 2016 American Chemical Society.

$Ti_{0.87}O_2$ (Ref. 207) afforded ferroelectricity due to electronic proximity coupling [Figs. 17(e) and 17(f)]. New artificial ferroelectrics were also demonstrated using the superlattice assembly of homologous perovskite nanosheets ($Ca_2Na_{m-3}Nb_mO_{3m+1}$; $m = 3$–6), which hold a paraelectric nature in their individual components.[208] Furthermore, magnetoelectric multiferroics emerged in $Ca_2Nb_3O_{10}/Ti_{0.8}Co_{0.2}O_2$ superlattices [Figs. 18(g) and 18(h)].[209] The above-mentioned superlattices were fabricated by electrostatic LbL and LB methods. Recently, nanosheet heterostructures have been successfully fabricated by a facile spin coating method.[210]

The solution-phase heterojunction is not limited to metal oxide nanosheet pairs. For example, photoexcited electron injection and *in situ* photoreduction activities were reported in multilayer films fabricated by sequential LbL deposition of $Ti_{0.87}O_2$ and GO nanosheets, resulting in highly improved carrier transport[211] and photomodulated conductance in a field effect transistor (FET) device[212] as well as modulated photochemical activity.[213] As another example, $Ca_2Nb_3O_{10}/MoS_2$ heterostructures were fabricated by the LB method.[214] In the LB assembly process, amphipathic TBA^+ couples charge-neutral MoS_2 grown by the CVD method and negatively charged $Ca_2Nb_3O_{10}$ monolayers through vdW/electrostatic dual interactions, resulting in a trion luminescence band from $1L$-MoS_2 at an unusually low energy position (ca. 1.6 eV). Subsequent interface engineering to decompose TBA^+ with a flattened molecular conformation reactivates exciton emission, while the band position is redshifted in comparison with that of unmodified $1L$-MoS_2 probably due to the pronounced dielectric proximity effects.

B. TMDCs

As described in Sec. II E 2, Lin *et al.* reported in 2018 electrochemical exfoliation using organoamines to synthesize high-quality TMDC nanosheets.[27] The FET device fabricated by spin coating THAB-exfoliated MoS_2 nanosheets followed by conventional lithography offered average mobility of approximately 7–11 cm^2 V^{-1} s^{-1} and an ON/OFF ratio of 10^6 [Figs. 19(a) and 19(b)]. The mobility is approximately 50 to 1000 times larger than those obtained from thin film FET devices fabricated with MoS_2 nanoflakes synthesized by ultrasonication.[34,215] This colloidal integration approach was applied for large-scale fabrication of various kinds of thin-film transistor arrays

from functional logic gates (such as NAND, NOR, AND, and XOR gates) to computational circuits (such as inverter, half adder, and full adder circuits). Interestingly, the multilayer film obtained by the spin coating yielded a mobility value close to that obtained with the single MoS_2 nanosheet (ca. 10 cm^2 V^{-1} s^{-1}) [Fig. 7(e)], indicating a reasonable charge transport through the stacked nanosheets. These experimental results support the advantage of plane-to-plane contacts compared with the point-to-point contacts formed by the assembly of nanoparticles and nanowires. It should be addressed that the treatment of the as-deposited MoS_2 film with bis(trifluoromethane)sulfonimide (TFSI) solution for 2 h at 80 °C followed by moderate thermal annealing (200–300 °C) was employed in the device fabrication process, which eliminated THAB or PVP used as intercalants and surfactants, respectively [Fig. 19(c)].

Gao *et al.* further studied the effects of the semiconductor channel thickness and TFSI/annealing treatments on the FET properties of THBA-exfoliated MoS_2 nanosheets. Note that instead of spin coating, electrostatic LbL was employed for thin-film deposition, where PDDA conventionally employed for the LbL process of oxide nanosheets was used as a cationic counterpart [Fig. 20(a)].[113] First, they investigated the effects of deposition-cycle numbers on transport properties. FET devices ($L = 20 \mu m$, $W = 100 \mu m$) based on $(PDDA/MoS_2)_1$, $(PDDA/MoS_2)_2$, and $(PDDA/MoS_2)_3$ films provided the average currents of 32.7 ± 6.9, 42.4 ± 7.7 and 63.0 ± 3.6 μA, respectively [Fig. 20(b)]. The ON/OFF ratios in a range of 10^5 were obtained for FETs based on $(PDDA/MoS_2)_1$ and $(PDDA/MoS_2)_2$ films. However, FETs based on $(PDDA/MoS_2)_3$ showed a significantly decreased ON/OFF ratio of less than 10^3 due to the high current values at the OFF state, which was associated with the large thickness (~18 nm), i.e., too thick to be fully depleted. It is notable that the mobilities up to 9.8 cm^2 V^{-1} s^{-1} and ON/OFF ratios of 2.1×10^5 of the FETs based on $(PDDA/MoS_2)_2$ films are close to the aforementioned spin-coated MoS_2 FETs. The work clearly demonstrates that post-treatment, or interface engineering, is important to attain reasonable FET performance. ON/OFF ratios of as-deposited $[PDDA/MoS_2]_1$ is very small (22) due to heavy n-doping by electron–donor groups such as the nitrogen-containing functional groups in PVP. The thermal annealing at 300 °C (2 h) or TFSI immersion at 80 °C (2 h) moderately enhanced the ON/OFF ratios to 880 [Fig. 20(c)] and 6000 [Fig. 19(d)], respectively. The removal of polymer residue by thermal annealing can significantly
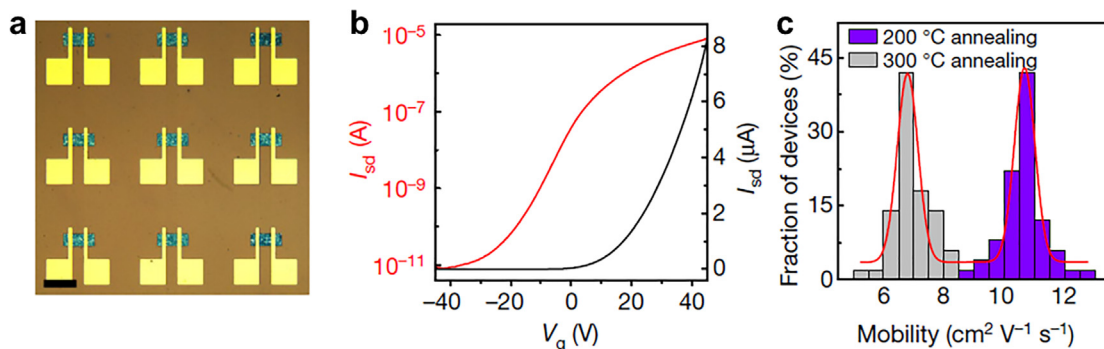
FIG. 19. FET application of electrochemically exfoliated 2H-MoS_2 nanosheets. (a) Optical microscope image of an array of back-gate thin-film transistors fabricated on a 90-nm-thick SiO_2/Si substrate. Scale bar, 100 μm. (b) I_{sd}–V_g transfer characteristics with $V_{sd} = 1$ V. (c) The statistical distribution of mobility for 50 individual transistors annealed at 200 (purple bars) and 300 °C (gray bars). Reproduced with permission from Lin *et al.*, Nature **562**, 254 (2018). Copyright 2018 Springer Nature Publishing.

FIG. 20. Control of FET characteristics of MoS_2 thin layer obtained by the LbL method. (a) Schematic of the LbL assembly pro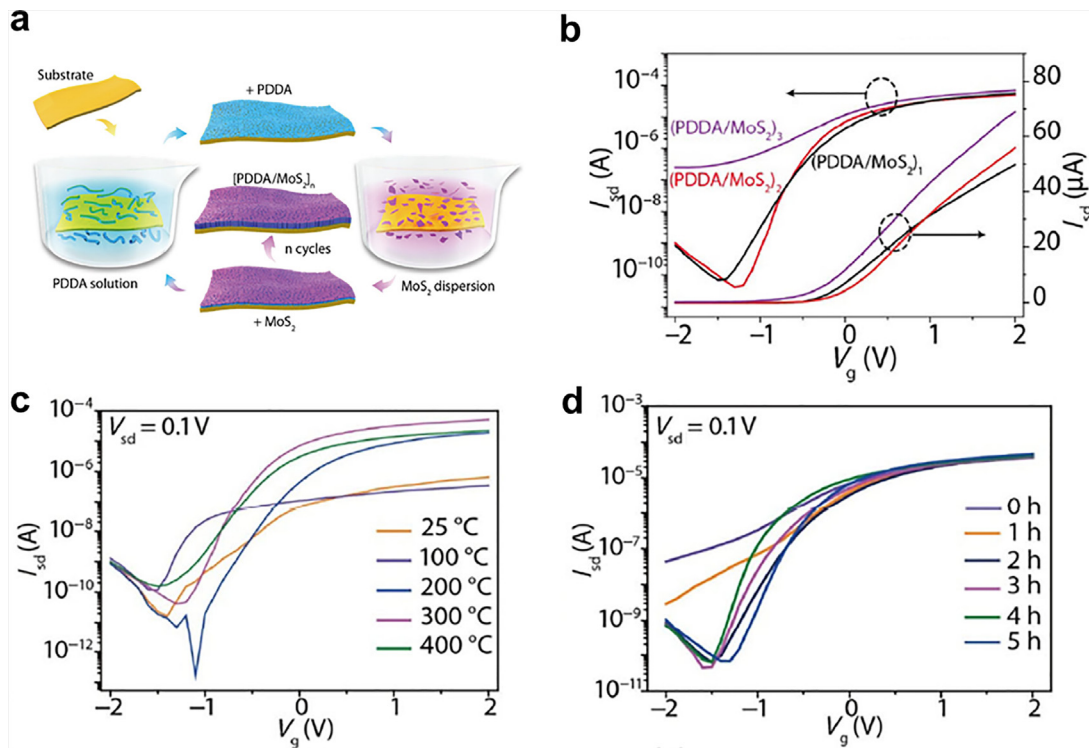cess for MoS_2 thin films. (b) Representative I_{sd}–V_g transfer characteristics of FETs (L = 20 μm, W = 100 μm) with different MoS_2 film thicknesses. (c) Transfer characteristics of MoS_2 FETs at different thermal annealing temperatures. (d) Transfer characteristics of MoS_2 FETs at different TFSI processing times. Reproduced with permission from Gao et al., Nano Res. **14**, 2255 (2021). Copyright 2021 Springer Nature Publishing.

increase the ON current, while the strong electron-withdrawing capability of TFSI allows the significant OFF current suppression. The combination of TFSI treatment and thermal annealing up to 300 °C could achieve the ON/OFF ratio surpassing 10^5. The complete removal of N-containing species at 400 °C, however, yielded a lower on-current in comparison to that at 300 °C. As addressed in Sec. IV A 1, metal oxide nanosheets exhibited thermal robustness so that thermal decomposition was applied to produce clean surfaces and interfaces. However, the development of interface control other than thermal treatments should be crucial to maximize the potential performance of chemically exfoliated TMDC nanosheets. As the maximum processing temperatures could be as low as 200 °C, it is feasible to fabricate the MoS_2 FETs on flexible PET foils showing the mostly maintained ON currents and ON/OFF ratios upon bending.

The above two references indicate that chemically exfoliated MoS_2 nanosheets offer a solution-processed FET with reasonably high mobility and ON/OFF ratio. The excellent semiconducting properties of chemically exfoliated TMDCs should be promising for PD applications. As mentioned above, oxide nanosheets have a wide bandgap so that they can be used for UV-PD. On the other hand, the bandgaps ranging ca. 1–2.5 eV are available in TMDCs depending on the chemical composition and layer numbers,[216] and PDs sensitive to near-infrared to visible light will be developed with them. PD applications were demonstrated by Ma et al. for $PtSe_2$ and $PtTe_2$ bilayer nanosheets,[114] which were synthesized by organoamine-assisted electrochemical exfoliation. In their study, $PtSe_2$ or $PtTe_2$ based FETs were fabricated by drop casting. Figure 21(a) shows how the power density of a 1064 nm laser modified the photocurrent of the $PtSe_2$-based FET. The photoresponsivities of the solution-processed $PtSe_2$ and $PtTe_2$ PDs were 72 and 1620 mA W^{-1}, respectively, at zero gate voltage under 1540 nm laser illumination, which was several orders of magnitude higher than those of the majority of IR photodetectors based on graphene, TMDCs, and black phosphorus [Fig. 21(b)]. Furthermore, the solution-processed $PtSe_2$ and $PtTe_2$ devices outperformed their mechanically exfoliated counterparts under similar wavelength laser illumination with a reasonable specific detectivity beyond 109 Jones and outstanding air stability (>several months). Finally, they successfully fabricated wafer-scale IR detectors using $PtSe_2$ and $PtTe_2$ colloidal dispersions. It is noteworthy that in their PD fabrication step, $PtSe_2$/$PtTe_2$ films deposited onto the SiO_2/Si substrate via drop casting were placed in DMSO to remove residual amine species followed by drying in a vacuum. Although the effects of DMSO cleaning on the surface properties and device performances were not described, solvent washing might be an effective cleaning method for the interfaces of multilayer stacks of TMDC nanosheets in addition to the postannealing and chemical doping addressed above.

In an important work regarding the application of chemically exfoliated TMDC nanosheets, Li et al. employed $NbSe_2$ monolayers obtained by modified electrochemical methods to produce superconducting thin films and composites.[115] The drop-cast $NbSe_2$ thin films
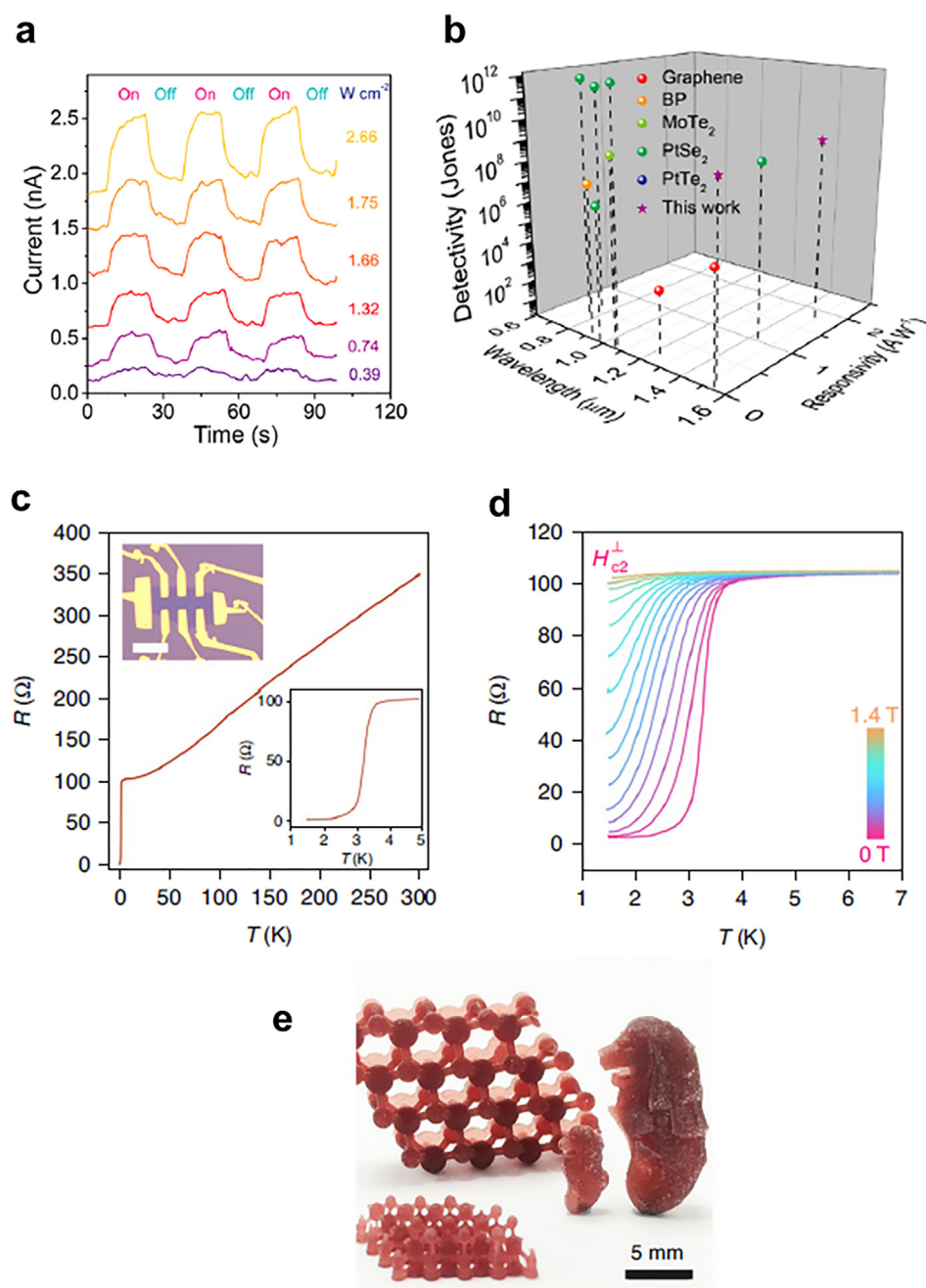
FIG. 21. Photodetector and superconductor applications of electrochemically exfoliated TMDC nanosheets. (a) Time-resolved photocurrent of the bilayer-PtSe$_2$ device for a bias voltage of 0.5 V by 1064 nm laser illumination with different laser power densities. (b) Comparison with the reported IR photodetector based on 2D materials. Reproduced with permission from Ma *et al.*, ACS Appl. Mater. Interfaces **13**, 8518 (2021). Copyright 2021 American Chemical Society. (c) Temperature-dependent longitudinal resistance for a monolayer NbSe$_2$ device. Upper inset: optical microscopic image of a typical monolayer NbSe$_2$ Hall bar device. Lower inset: resistance detail from 1.5 to 7 K. (d) Temperature-dependent resistance of a monolayer NbSe$_2$ device under different perpendicular magnetic fields ranging from 0 to 1.4 T. (e) Digital photographs of NbSe$_2$ atomic models and Merlion statues fabricated by 3D printing. Reproduced with permission from Li *et al.*, Nat. Mater. **20**, 181 (2021). Copyright 2021 Springer Nature Publishing.

showed a critical current modulated by a magnetic field [Figs. 21(c) and 21(d)]. Nanosheet inks can also be used to produce wafer-scale 2D superconducting wire arrays. Furthermore, exfoliated NbSe$_2$ monolayers can be mixed with Genesis resin for 3D printing, enabling the production of three-dimensional structures [Fig. 21(e)]. Under a magnetic field of 200 Oe, the temperature-dependent magnetization of 3D printed structures displayed a diamagnetic signal at ~6.8 K, corresponding to the superconducting transition. Thus, it is confirmed that superconductivity is retained in 3D printed structures.

C. MXenes

Most MXenes are metallic conductors. Therefore, MXenes can be used as electrodes for nanoelectronics applications. For example, Lyu *et al.* demonstrated the fabrication of a large-scale, uniform MXene electrode array on a flexible plastic substrate for application to high-performance organic FETs (OFETs).[217] An important step in the device fabrication is patterning hydrophilic/hydrophobic areas on a polymer substrate by UV/O$_3$ treatment through a shadow mask. The MXene nanosheets were deposited on the UV/ozone-treated
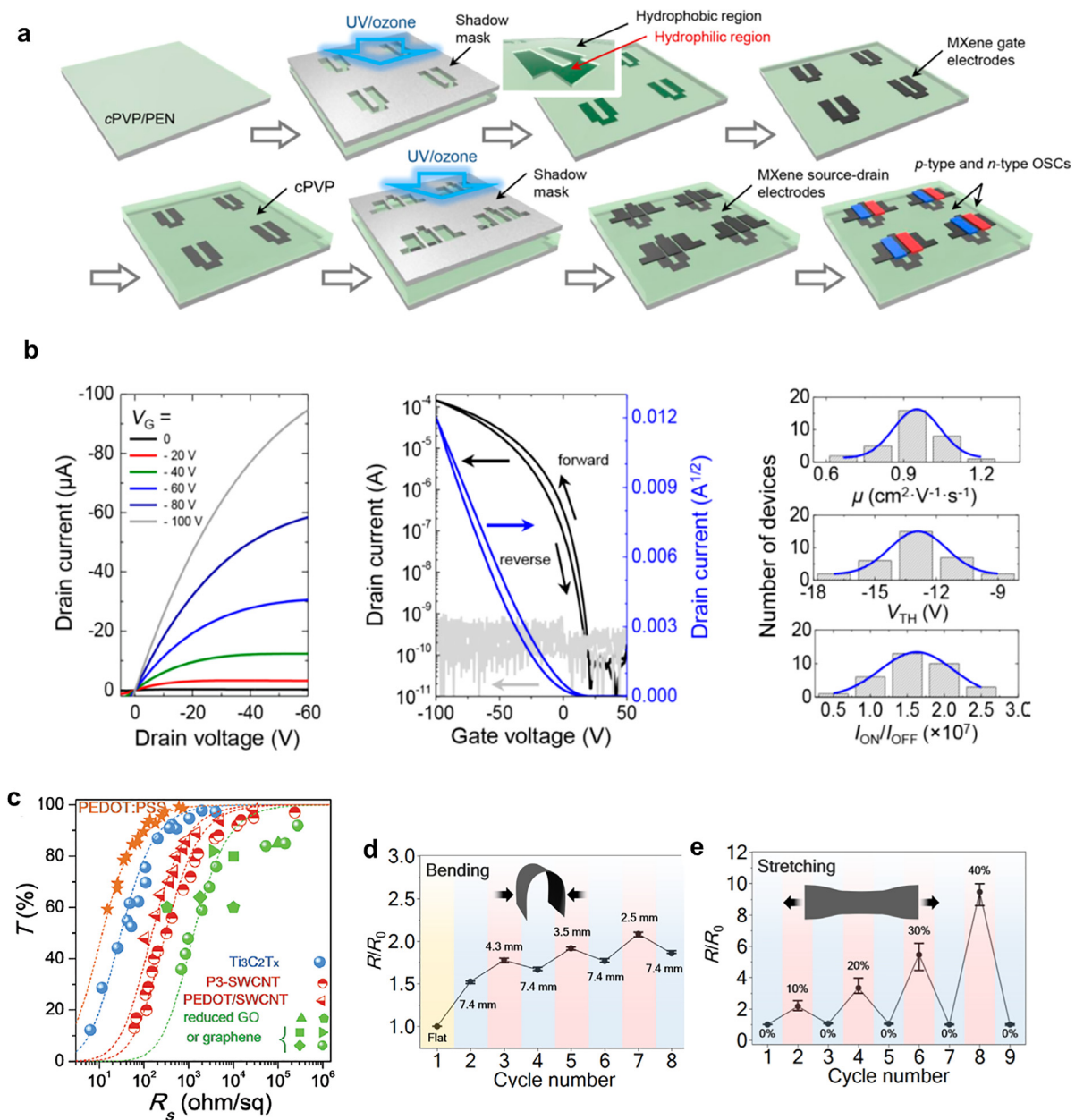
FIG. 22. Electrode applications of MXenes. (a) Schematic diagram showing a fabrication process of OFETs with $Ti_3C_2T_x$ MXene gate, source, and drain electrodes. (b) Output characteristics (left) and transfer characteristics (middle) of p-type pentacene OFETs with pristine $Ti_3C_2T_x$ MXene electrodes. The gray line indicates the gate current. Histogram and normal distribution of electrical properties of p-type pentacene OFETs with MXene electrodes (right). Reproduced with permission from Lyu et al., ACS Nano **13**, 11392 (2019). Copyright 2021 American Chemical Society. (c) T plotted as a function of R_s for the $Ti_3C_2T_x$ films and comparison to other transparent conducting films. Reproduced with permission from Zhang et al., Adv. Mater. **29**, 1702678 (2017). Copyright 2017 Wiley-VCH. Cycling performance under (d) bending and (e) stretching of an MXene film. Reproduced with permission from An et al., Sci. Adv. **4**, eaaq0118 (2018). Copyright 2018 Authors licensed under a Creative Commons Attribution NonCommercial License 4.0 (CC BY-NC).

hydrophilic region after dip-coating to produce patterned MXene electrodes [Fig. 22(a)]. The resulting p- and n- type OFETs showed excellent device performance, such as maximum carrier mobility of $\sim 1 \, cm^2 \cdot V^{-1} \cdot s^{-1}$ and I_{ON}/I_{OFF} of $\sim 10^7$ [Fig. 22(b)]. Furthermore, the patterning method was successfully extended to the fabrication of complementary logic circuits. Montazeri et al. produced patterned MXene electrodes by a conventional method using a photoresist.[218] The GaAs-PD with MXene electrodes showed significantly higher responsivities and quantum efficiencies than that of the standard Au electrodes.

The excellent electrochemical capacitance or electromagnetic shielding properties of MXenes can be coupled with the optical transparency of ultrathin MXene films to develop optically transparent energy storage devices[219] and electromagnetic shields.[220] Zhang et al. examined the relationship between optical transmittance and sheet resistivity using a $Ti_3C_2T_x$ film fabricated by spin coating an MXene dispersion.[219] The resistivity of ca. $1\,k\Omega\,sq^{-1}$ was observed when the transparency was approximately 95% in the visible region [Fig. 22(c)]. The reported transparency–resistivity relationship is close to those of the aforementioned RuO_2 nanosheets. In addition, An et al. employed electrostatic LbL deposition of $Ti_3C_2T_x$ nanosheets to obtain stretchable, bendable, and foldable conducting films.[136] The coating showed a recoverable resistance response to bending (up to a 2.5-mm bending radius) and stretching (up to 40%

tensile strain) [Figs. 22(d) and 22(e)]. Thus, MXene-based coatings can be implemented onto mechanically deformable objects.

In 2019, Tian et al. investigated the effects of cationic species used in electrostatic LbL assembly on the electrical resistivity of MXene thin films.[137] In this study, LbL deposition was conducted with MXenes exfoliated by ultrasonic treatment. Uniquely, they used a small molecule, tris(2-aminoethyl) amine (TAEA), as a cationic counterpart to negatively charged MXenes [Fig. 23(a)]. The ten-cycled LbL films with TAEA exhibit the sheet resistance of $154\,\Omega\,sq^{-1}$, which is much lower than that of ten-cycled LbL MXene films with conventional PEI ($830\,\Omega\,sq^{-1}$) and PDDA ($8\,k\Omega\,sq^{-1}$) [Fig. 23(b)]. These findings indicate that polyelectrolytes, such as PEI, resulted in large insulating gaps between neighboring MXene flakes with an interlayer spacing of 8.71 Å, interrupting electron transport between the flakes.
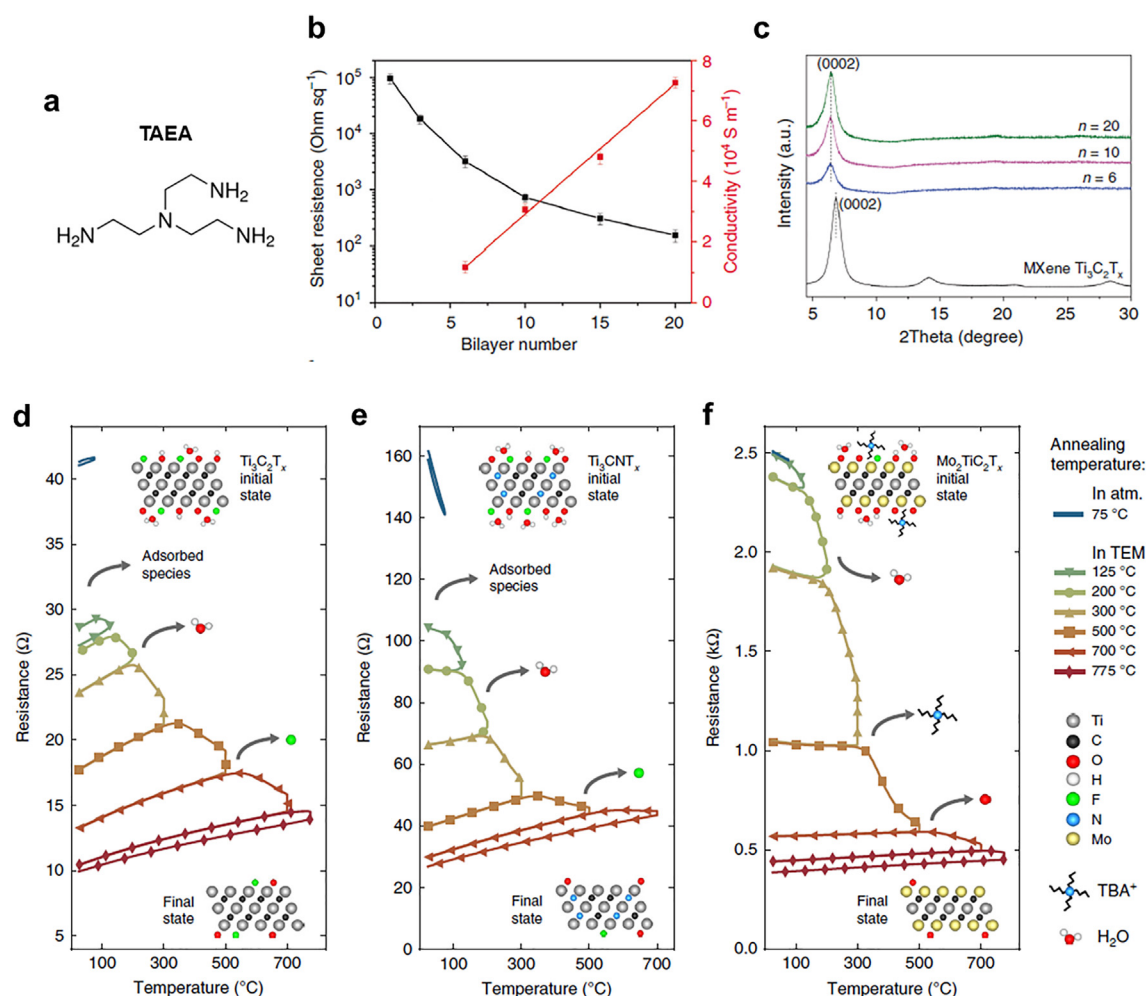

FIG. 23. Surface and interface engineering of MXenes. (a) Molecular structure of TAEA. (b) Sheet resistance and electric conductivity of (MXene/TAEA)$_n$ on silicon wafers vs n. (c) XRD patterns of (MXene/TAEA)$_n$ vs n and pure MXene $Ti_3C_2T_x$ film. Reproduced with permission from Tian et al., Nat. Commun. **10**, 2558 (2019). Copyright 2019 Authors licensed under Creative Commons Attribution 4.0 International License (CC BY 4.0). Evolution of MXene electronic properties through in situ vacuum annealing. Resistance vs temperature measurements is shown for $Ti_3C_2T_x$ (d), Ti_3CNT_x (e), and $Mo_2TiC_2T_x$ (f). The atomic structures of various MXenes are shown as insets. The initial state schematics (top schematics) show $Ti_3C_2T_x$ and Ti_3CNT_x with intercalated water molecules on their surfaces, and $Mo_2TiC_2T_x$ is shown with water and TBA^+ ions. Reproduced with permission from Hart et al., Nat. Commun. **10**, 522 (2019). Copyright 2019 Authors licensed under Creative Commons Attribution 4.0 International License (CC BY 4.0).

On the other hand, TAEA can significantly narrow the interlayer spacing (1.0 Å) in the LbL films to facilitate the layer-to-layer electron transport [Fig. 23(c)].

In 2019, Hart et al. directly correlated MXene surface defunctionalization with increased electronic conductivity through in situ TEM analysis.[221] They found that in situ annealing of multilayer $Ti_3C_2T_x$, Ti_3CNT_x, $Ti_3CNT_x(TBA^+)$, and $Mo_2TiC_2T_x$ resulted in the 4, 6, >10, and 6-fold increased conductivity, respectively [Figs. 23(d) and 23(e)]. Simultaneous deintercalation or surface defunctionalization was confirmed by both in situ and ex situ spectroscopic techniques. Moreover, both H_2O and TBA^+ intercalants led to semiconductor-like negative dR/dT. They proposed that the low conductivity of the as-synthesized MXene multilayers could be associated with transitions from metallic to semiconductor-like transport caused by the insertion of the guest molecules. TBA^+ in the gallery of MXene layers imparts more strong influences on the electronic properties than H_2O, and the effects of TBA^+ sustained even after annealing above 750 °C. They further provide useful insights into interface reactions of MXene such as higher stability of oxygen terminations than F-terminations and more facile defunctionalization of $Mo_2TiC_2T_x$ than Ti-based MXenes. Hence, the works of Tian et al. and Hart et al. demonstrate that interface engineering is critically important to optimize the electrical conductivity of MXene ultrathin films. Considering the large diversity in the chemical composition of the MXene family, there should remain plenty of opportunity to find better MXenes for general and specific applications. Han et al. systematically studied three interrelated binary solid-solution MXene systems based on Ti, Nb, and/or V at the M-site in an M_2XT_x structure ($Ti_{2-y}Nb_yCT_x$, $Ti_{2-y}V_yCT_x$, and $V_{2-y}Nb_yCT_x$), showing the evolution of electronic and optical properties as a function of composition.[222] The authors also demonstrated the wide range of conductivity of films based on M_2XT_x, $M_3X_2T_x$, and $M_4X_3T_x$ (ca. 10^1–10^4 S cm^{-1}).[223] Thus, in fact, the conductivity and optical properties can be tuned on demand to some extent by selecting an appropriate MXene.

V. PERSPECTIVE

As introduced in this Review, chemical exfoliation methods, particularly those using organoamines as an exfoliation agent, have enabled us to obtain high-quality oxide, TMDC, and MXene nanosheets in high yield. Colloidal deposition processes using nanosheet dispersions allow the fabrication of nanoscale thin films at ambient temperature and pressure. Recent years have witnessed a high demand for technological innovations in various fields. In the semiconductor industry, the development of high-performance flexible devices for the realization of the IoT society has become a major concern. Due to the difficulty of fabricating electronic devices with plastics and paper using conventional semiconductor processes, which require a high deposition temperature. Solution or colloidal processes with nanoparticles have been considered alternative approaches. However, devices fabricated by this approach generally suffer from insufficient performance. In contrast, devices based on such nanosheet assembly have already yielded satisfactory performance not far from those required for practical applications. Therefore, the nanosheet-based process will offer a new platform to develop flexible devices, including wearable devices.

To exploit the potential of chemically exfoliated nanosheets as a device component, further efforts are needed from chemistry, physics, and materials science aspects. For example, theoretical approaches

should be developed for a better understanding of the electronic states and exfoliation phenomena of nanosheets. The DFT calculations by Sato et el. resulted in a close similarity in the densities of states and bandgap between single and stacked TiO_2 nanosheets [Fig. 4(c)];[93] however, the calculation does not reproduce the exfoliation-induced bandgap enlargement observed experimentally. The discrepancy probably comes from the difference between the real and model structures. Namely, surface dangling bonds and surface termination in a real $Ti_{0.87}O_2^{0.52-}$ nanosheets are excluded to build the lepidocrocite TiO_2 model in the Sato's and subsequent DFT studies.[94,95] To our knowledge, there are no detailed DFT studies on oxide nanosheets using structural models that include guest and surface species. Thus, more proper modeling should be developed, considering the interfacial bonding states between host and guest (surface) species. Although the phenomenological understanding of the exfoliation of layered oxides has been established through intensive experimental studies for two decades, a theoretical approach is further needed to understand the exfoliation phenomena at the molecular level. In addition, the utilization of data science or materials informatics is emerging as a new approach to inductively extract essential parameters determining intercalation/swelling/exfoliation boundaries.[224]

In the case of TMDC nanosheets, suitable exfoliation conditions should be found to improve the monolayer yield and lateral size/shape. Simultaneously, the defects and surface states must be finely controlled, as any extrinsic factors potentially induced during exfoliation (formation of defects, etc.), have a critical impact on semiconducting properties. THBA-exfoliated MoS_2 nanosheets have shown electron mobility approximately three times lower than that of benchmarking high-quality CVD MoS_2 (ca. 30 cm^2 V^{-1} s^{-1}).[225] Rapid progress in the chemical exfoliation method is expected and will lead to higher mobility in the near future. There will be opportunities for the chemical exfoliation strategy to be applied to efficient exfoliation of other layered compounds. For example, recently, Kondo et al. have reported the synthesis of hydrogen boride nanosheets through chemical etching of the magnesium layer in MgB_2.[226] Chemical exfoliation with organoamine cations or other types of bulky ionic species may assist in improving the yield of the monolayers.

Concerning the integration methods, the electrostatic LbL and LB methods have already been applied to oxides, TMDC, and MXene nanosheets. Spin coating and drop-casting methods, more recently developed for facile monolayer-level deposition of oxide nanosheets, will be employed for TMDC and MXene sheets, considering their common surface chemistry. In addition to the quality of individual nanosheets, the device performance relies on the interfacial state between the nanosheets and substrate as well as between the nanosheets themselves. Most oxide nanosheets exhibit high oxidation resistance and thermal stability, which allows them to be treated with robust cleaning processes, such as UV-O_3 and annealing treatments (≥400 °C) to remove organic species almost completely while maintaining their crystalline nature. On the other hand, since these treatments degrade the performance of TMDCs, other approaches, such as optimization of the washing process, introduction of appropriate interface species during deposition, or substitution of appropriate molecules after deposition, are likely to be the main options to control the interfaces. Although the thermal and chemical stability of a wide range of MXenes has not been fully revealed, low-temperature annealing in an oxidizing atmosphere produces oxide impurities in $Ti_3C_2T_x$ (ca.

300 °C)[227] and V_2CT_x[228] (ca. 200 °C). Similar to TMDCs, oxidation should be suppressed during interface modification. It will be crucial to control the surface functional groups generated at the etching step in MXene synthesis. In this regard, extensive studies on the reduction of GO will be of help and used as a reference.[229]

Next, we also face challenges in developing devices based on chemically exfoliated nanosheets (Fig. 24). First, for oxides, further improvement of dielectric properties will be an important subject. To date, the maximum dielectric constant of nanosheet thin films is approximately 500 [Fig. 12(a)], which is well above that of the next-generation gate insulator HfO_2 thin film (25) but still much below the dielectric constant of bulk $BaTiO_3$ (ca. 7000) at room temperature. Therefore, it is of both fundamental and practical importance to pursue the limit of dielectric performance of perovskite nanosheets via A/B-site and/or superlattice engineering approaches. Essential efforts toward practical applications of dielectric nanosheets will involve the adoption of the above deposition methods for the large-scale fabrication of nanofilms with uniform quality. Since there are no 2D nanomaterials other than *h*BN and oxide nanosheets that have a wide bandgap suitable for insulating layers in 2D vdW materials, oxide nanosheets may play a role as promising insulating layers for the construction of 2D heterostructures. From broader physical aspects, metal oxides with various compositions and structures are a treasure trove of functions. The further development of oxide nanosheets with fascinating functions, such as oxygen ion conductivity, transparent conductivity, high-temperature superconductivity, and Mott transition, will be a long-term research prospect.

For TMDCs, it has been only three years since highly efficient electrochemical exfoliation using organoamines was reported. Therefore, research from a fundamental perspective will be one of the main subjects in the next few years. Further seeking effective combinations of intercalants and organic solvents is essential. At the same time, the interaction/swelling/exfoliation boundaries, which are unclear at present, should be outlined to establish reliable guidelines for high-yield exfoliation. As another essential task, we need to reveal

that a range of TMDCs, as well as other 2D vdW crystals, is exfoliatable with electrochemical exfoliation with organoamines. If this approach is widely applicable to the synthesis of monolayers of 2D vdW crystals, which are difficult to obtain through adhesive tape-exfoliation and vacuum-phase growth methods, the chemical exfoliation method can serve as a platform for discovering new nanosheets. Chemical exfoliation of new nanosheets and subsequent thin-film fabrication via the colloidal deposition process should be desirable, facilitating device applications of nanosheets with unique functionalities.

Chemical exfoliation is essential for finding new materials and functions of MXenes, since the other methods to obtain 2D nanomaterials are not available yet. At present, owing to metallic conductivities, MXenes attract great interest in developing ultrathin and/or flexible electrodes, while theoretical studies predict that MXenes cover broader physical properties, including magnetism,[230] fully spin-polarized transport,[231] semiconducting behavior,[232] and nontrivial topological order.[233] MXenes are emerging as one of the most actively studied nanosheets for energy device applications such as electrochemical capacitors and secondary batteries. In conjunction with the progress of the energy applications of MXenes, MXene-based nanoelectronics and spintronics will be advanced simultaneously.

Oxide, TMDC, and MXene nanosheets exhibit excellent dielectric, semiconducting, and metallic properties, respectively. Thus, their combination can offer a cherished opportunity to create various all-nanosheet devices. As addressed in Sec. II B, Kelly *et al.* reported FET devices consisting of MoS_2, *h*BN insulators, and graphene nanoflakes obtained by ultrasonication for semiconductor channels, gate insulators, and electrodes.[40] However, the mobility of the resultant device is rather poor (0.3 cm^2 V^{-1} s^{-1}), indicating that there are many deteriorating factors in each layer in terms of crystallinity and overall film quality. In addition, the device is not optically transparent due to the multilayer features of individual nanoflakes and uncontrollable film thickness at the nanoscale. Furthermore, the gate insulator consists of *h*BN nanoflakes mixed with ionic liquid, as *h*BN exhibits a tiny dielectric constant (ca. 3–4).[234] The use of ionic liquids in devices makes
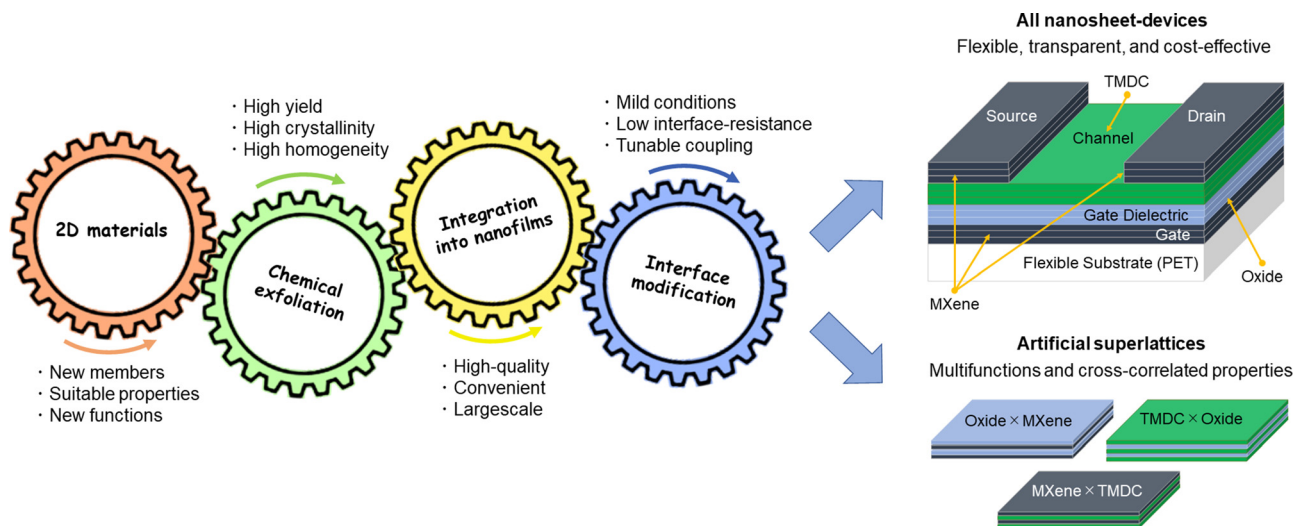
FIG. 24. Research elements and directions for the application of chemically exfoliated nanosheets in nanoelectronics.

practical applications impossible due to the lack of chemical and thermal stability as well as switching speeds. If chemically exfoliated nanosheets, including oxide nanosheets with a dielectric constant over 200, MoS_2 with mobility over $10\,cm^2\,V^{-1}\,s^{-1}$, and MXene with high electrical conductivity over 10^4 S/cm, are conjugated to fabricate FET devices, an actual all-nanosheet FET with high device performance, durability, optical transparency, and mechanical flexibility will potentially be invented. This can be set as an ultimate goal. Furthermore, a programmable deposition of desired nanosheets selected from the ever-expanding materials library will offer a platform to search for artificial heterostructures and superlattices with multifunctional or cross-correlated properties.

Many challenges will be addressed in the short term under multidisciplinary collaborations. The research field dealing with device applications of chemically exfoliated nanosheets is in its infancy so it may be premature to predict longer-term prospects. Finally, chemically exfoliated nanosheets and related technologies will occupy a unique and important position in solid-state chemistry, solid-state physics, and materials science for the next decade.

VI. SUMMARY

Herein we reviewed the development of nanosheets based on oxides, TMDCs, and MXenes in terms of chemical exfoliation of layered crystals, fabrication of ultrathin films by colloidal integration, and their applications in electronic, magnetic, and optical devices. As seen from this review, the field of chemical exfoliation has a relatively long history over the past two decades and is still very active. At the same time, colloidal integration processes have been developed to enable monolayer, multilayer, and even superlattice deposition in a more convenient manner. Chemically exfoliated nanosheets are expected to find applications, especially in transparent and/or flexible devices, as 2D nanomaterials obtained by vacuum deposition methods are not suitable for such applications because of their high reaction temperature and high cost. While significant scientific and technological achievements have been made, enormous challenges remain in the exfoliation and integration steps for the exploration of new materials and applications and to control device performance. In this sense, there is plenty of opportunity for new research in this field. With continued effort, colloidal integration with exfoliated functional nanosheets will provide a practical route to a wide range of scientific and industrial applications.

AUTHOR DECLARATIONS
Conflict of Interest

The authors have no conflicts to disclose.

DATA AVAILABILITY

Data sharing is not applicable to this article as no new data were created or analyzed in this study.

REFERENCES

[1] K. S. Novoselov, A. K. Geim, S. V. Morozov, D. Jiang, Y. Zhang, S. V. Dubonos, I. V. Grigorieva, and A. A. Firsov, Science **306**(5696), 666–669 (2004).

[2] Y. Zhang, T.-T. Tang, C. Girit, Z. Hao, M. C. Martin, A. Zettl, M. F. Crommie, Y. R. Shen, and F. Wang, Nature **459**(7248), 820–823 (2009).

[3] Y. Cao, V. Fatemi, S. Fang, K. Watanabe, T. Taniguchi, E. Kaxiras, and P. Jarillo-Herrero, Nature **556**(7699), 43–50 (2018).

[4] K. P. Loh, Q. Bao, G. Eda, and M. Chhowalla, Nat. Chem. **2**(12), 1015–1024 (2010).

[5] D. D. Chronopoulos, A. Bakandritsos, M. Pykal, R. Zbořil, and M. Otyepka, Appl. Mater. Today **9**, 60–70 (2017).

[6] K. E. Whitener, Jr., J. Vac. Sci. Technol. A **36**(5), 05G401 (2018).

[7] S. Manzeli, D. Ovchinnikov, D. Pasquier, O. V. Yazyev, and A. Kis, Nat. Rev. Mater. **2**(8), 17033 (2017).

[8] M. Akhtar, G. Anderson, R. Zhao, A. Alruqi, J. E. Mroczkowska, G. Sumanasekera, and J. B. Jasinski, npj 2D Mater. Appl. **1**, 5 (2017).

[9] A. Molle, C. Grazianetti, L. Tao, D. Taneja, M. H. Alam, and D. Akinwande, Chem. Soc. Rev. **47**(16), 6370–6387 (2018).

[10] D. Li, J. Gao, P. Cheng, J. He, Y. Yin, Y. Hu, L. Chen, Y. Cheng, and J. Zhao, Adv. Funct. Mater. **30**(8), 1904349 (2020).

[11] A. Splendiani, L. Sun, Y. Zhang, T. Li, J. Kim, C.-Y. Chim, G. Galli, and F. Wang, Nano Lett. **10**(4), 1271–1275 (2010).

[12] Y. Cai, G. Zhang, and Y.-W. Zhang, Sci. Rep. **4**, 6677 (2014).

[13] O. Lopez-Sanchez, D. Lembke, M. Kayci, A. Radenovic, and A. Kis, Nat. Nanotechnol. **8**(7), 497–501 (2013).

[14] R. S. Sundaram, M. Engel, A. Lombardo, R. Krupke, A. C. Ferrari, P. Avouris, and M. Steiner, Nano Lett. **13**(4), 1416–1421 (2013).

[15] S. A. Vitale, D. Nezich, J. O. Varghese, P. Kim, N. Gedik, P. Jarillo-Herrero, D. Xiao, and M. Rothschild, Small **14**(38), 1801483 (2018).

[16] A. K. Geim and I. V. Grigorieva, Nature **499**(7459), 419–425 (2013).

[17] K. Kang, K.-H. Lee, Y. Han, H. Gao, S. Xie, D. A. Muller, and J. Park, Nature **550**(7675), 229–233 (2017).

[18] K. S. Novoselov, A. Mishchenko, A. Carvalho, and A. H. Castro Neto, Science **353**(6298), aac9439 (2016).

[19] D. Akinwande, N. Petrone, and J. Hone, Nat. Commun. **5**, 5678 (2014).

[20] H. P. Boehm, A. Clauss, G. O. Fischer, and U. Hofmann, Z. Anorg. Allg. Chem. **316**(3–4), 119–127 (1962).

[21] X. Wen, C. W. Garland, T. Hwa, M. Kardar, E. Kokufuta, Y. Li, M. Orkisz, and T. Tanaka, Nature **355**(6359), 426–428 (1992).

[22] P. Joensen, R. F. Frindt, and S. R. Morrison, Mater. Res. Bull. **21**(4), 457–461 (1986).

[23] T. Sasaki, M. Watanabe, H. Hashizume, H. Yamada, and H. Nakazawa, J. Am. Chem. Soc. **118**(35), 8329–8335 (1996).

[24] M. M. J. Treacy, S. B. Rice, A. J. Jacobson, and J. T. Lewandowski, Chem. Mater. **2**(3), 279–286 (1990).

[25] M. Osada, Y. Ebina, H. Funakubo, S. Yokoyama, T. Kiguchi, K. Takada, and T. Sasaki, Adv. Mater. **18**(8), 1023–1027 (2006).

[26] M. Osada and T. Sasaki, Adv. Mater. **24**(2), 210–228 (2012).

[27] Z. Lin, Y. Liu, U. Halim, M. Ding, Y. Liu, Y. Wang, C. Jia, P. Chen, X. Duan, C. Wang, F. Song, M. Li, C. Wan, Y. Huang, and X. Duan, Nature **562**(7726), 254–258 (2018).

[28] M. Naguib, R. R. Unocic, B. L. Armstrong, and J. Nanda, Dalton Trans. **44**(20), 9353–9358 (2015).

[29] H. Li, J. Wu, Z. Yin, and H. Zhang, Acc. Chem. Res. **47**(4), 1067–1075 (2014).

[30] B. Radisavljevic, A. Radenovic, J. Brivio, V. Giacometti, and A. Kis, Nat. Nanotechnol. **6**(3), 147–150 (2011).

[31] C. R. Dean, A. F. Young, I. Meric, C. Lee, L. Wang, S. Sorgenfrei, K. Watanabe, T. Taniguchi, P. Kim, K. L. Shepard, and J. Hone, Nat. Nanotechnol. **5**(10), 722–726 (2010).

[32] L. Li, Y. Yu, G. J. Ye, Q. Ge, X. Ou, H. Wu, D. Feng, X. H. Chen, and Y. Zhang, Nat. Nanotechnol. **9**(5), 372–377 (2014).

[33] B. Huang, G. Clark, E. Navarro-Moratalla, D. R. Klein, R. Cheng, K. L. Seyler, D. Zhong, E. Schmidgall, M. A. McGuire, D. H. Cobden, W. Yao, D. Xiao, P. Jarillo-Herrero, and X. Xu, Nature **546**(7657), 270–273 (2017).

[34]J. N. Coleman, M. Lotya, A. O'Neill, S. D. Bergin, P. J. King, U. Khan, K. Young, A. Gaucher, S. De, R. J. Smith, I. V. Shvets, S. K. Arora, G. Stanton, H.-Y. Kim, K. Lee, G. T. Kim, G. S. Duesberg, T. Hallam, J. J. Boland, J. J. Wang, J. F. Donegan, J. C. Grunlan, G. Moriarty, A. Shmeliov, R. J. Nicholls, J. M. Perkins, E. M. Grieveson, K. Theuwissen, D. W. McComb, P. D. Nellist, and V. Nicolosi, Science 331(6017), 568–571 (2011).

[35]F. Bonaccorso, A. Bartolotta, J. N. Coleman, and C. Backes, Adv. Mater. 28(29), 6136–6166 (2016).

[36]G. Cunningham, M. Lotya, C. S. Cucinotta, S. Sanvito, S. D. Bergin, R. Menzel, M. S. P. Shaffer, and J. N. Coleman, ACS Nano 6(4), 3468–3480 (2012).

[37]E. Varrla, C. Backes, K. R. Paton, A. Harvey, Z. Gholamvand, J. McCauley, and J. N. Coleman, Chem. Mater. 27(3), 1129–1139 (2015).

[38]C. Backes, R. J. Smith, N. McEvoy, N. C. Berner, D. McCloskey, H. C. Nerl, A. O'Neill, P. J. King, T. Higgins, D. Hanlon, N. Scheuschner, J. Maultzsch, L. Houben, G. S. Duesberg, J. F. Donegan, V. Nicolosi, and J. N. Coleman, Nat. Commun. 5, 4576 (2014).

[39]D. B. Velusamy, R. H. Kim, S. Cha, J. Huh, R. Khazaeinezhad, S. H. Kassani, G. Song, S. M. Cho, S. H. Cho, I. Hwang, J. Lee, K. Oh, H. Choi, and C. Park, Nat. Commun. 6, 8063 (2015).

[40]A. G. Kelly, T. Hallam, C. Backes, A. Harvey, A. S. Esmaeily, I. Godwin, J. Coelho, V. Nicolosi, J. Lauth, A. Kulkarni, S. Kinge, L. D. A. Siebbeles, G. S. Duesberg, and J. N. Coleman, Science 356(6333), 69–73 (2017).

[41]T. M. Higgins, S. Finn, M. Matthiesen, S. Grieger, K. Synnatschke, M. Brohmann, M. Rother, C. Backes, and J. Zaumseil, Adv. Funct. Mater. 29(4), 1804387 (2019).

[42]G. Hu, L. Yang, Z. Yang, Y. Wang, X. Jin, J. Dai, Q. Wu, S. Liu, X. Zhu, X. Wang, T.-C. Wu, R. C. T. Howe, T. Albrow-Owen, L. W. T. Ng, Q. Yang, L. G. Occhipinti, R. I. Woodward, E. J. R. Kelleher, Z. Sun, X. Huang, M. Zhang, C. D. Bain, and T. Hasan, Sci. Adv. 6(33), eaba5029 (2020).

[43]F. I. Alzakia, W. Jonhson, J. Ding, and S. C. Tan, ACS Appl. Mater. Interfaces 12(25), 28840–28851 (2020).

[44]F. I. Alzakia, B. Tang, S. J. Pennycook, and S. C. Tan, Mater. Horiz. 7(12), 3325–3338 (2020).

[45]T. Leng, K. Parvez, K. Pan, J. Ali, D. McManus, K. S. Novoselov, C. Casiraghi, and Z. Hu, 2D Mater. 7(2), 024004 (2020).

[46]J. Kim, S. Kim, Y. S. Cho, M. Choi, S.-H. Jung, J. H. Cho, D. Whang, and J. Kang, ACS Appl. Mater. Interfaces 13(10), 12221–12229 (2021).

[47]S. Ippolito, A. G. Kelly, R. Furlan de Oliveira, M.-A. Stoeckel, D. Iglesias, A. Roy, C. Downing, Z. Bian, L. Lombardi, Y. A. Samad, V. Nicolosi, A. C. Ferrari, J. N. Coleman, and P. Samorì, Nat. Nanotechnol. 16(5), 592–598 (2021).

[48]T. Carey, S. Cacovich, G. Divitini, J. Ren, A. Mansouri, J. M. Kim, C. Wang, C. Ducati, R. Sordan, and F. Torrisi, Nat. Commun. 8, 1202 (2017).

[49]S. Li, Y.-C. Lin, W. Zhao, J. Wu, Z. Wang, Z. Hu, Y. Shen, D.-M. Tang, J. Wang, Q. Zhang, H. Zhu, L. Chu, W. Zhao, C. Liu, Z. Sun, T. Taniguchi, M. Osada, W. Chen, Q.-H. Xu, A. T. S. Wee, K. Suenaga, F. Ding, and G. Eda, Nat. Mater. 17(6), 535–542 (2018).

[50]T. Jurca, M. J. Moody, A. Henning, J. D. Emery, B. Wang, J. M. Tan, T. L. Lohr, L. J. Lauhon, and T. J. Marks, Angew. Chem. Int. Ed. 56(18), 4991–4995 (2017).

[51]F. Godel, V. Zatko, C. Carrétéro, A. Sander, M. Galbiati, A. Vecchiola, P. Brus, O. Bezencenet, B. Servet, M.-B. Martin, B. Dlubak, and P. Seneor, ACS Appl. Nano Mater. 3(8), 7908–7916 (2020).

[52]H. Park, N. Liu, B. H. Kim, S. H. Kwon, S. Baek, S. Kim, H.-K. Lee, Y. J. Yoon, and S. Kim, ACS Appl. Mater. Interfaces 12(18), 20645–20652 (2020).

[53]T. Orzali, M. Casarin, G. Granozzi, M. Sambi, and A. Vittadini, Phys. Rev. Lett. 97(15), 156101 (2006).

[54]R. Addou, A. Dahal, and M. Batzill, Nat. Nanotechnol. 8(1), 41–45 (2013).

[55]J. Yu, J. Li, W. Zhang, and H. Chang, Chem. Sci. 6(12), 6705–6716 (2015).

[56]Y. Zhang, L. Zhang, and C. Zhou, Acc. Chem. Res. 46(10), 2329–2339 (2013).

[57]J. Sun, C. Lu, Y. Song, Q. Ji, X. Song, Q. Li, Y. Zhang, L. Zhang, J. Kong, and Z. Liu, Chem. Soc. Rev. 47(12), 4242–4257 (2018).

[58]Y. Shi, H. Li, and L.-J. Li, Chem. Soc. Rev. 44(9), 2744–2756 (2015).

[59]J. B. Smith, D. Hagaman, and H.-F. Ji, Nanotechnology 27(21), 215602 (2016).

[60]Y. Zhang, Y. Yao, M. G. Sendeku, L. Yin, X. Zhan, F. Wang, Z. Wang, and J. He, Adv. Mater. 31(41), 1901694 (2019).

[61]T. Ban, Y. Kondo, and Y. Ohya, CrystEngComm 18(45), 8731–8738 (2016).

[62]K. Kai, Y. Yoshida, H. Kageyama, G. Saito, T. Ishigaki, Y. Furukawa, and J. Kawamata, J. Am. Chem. Soc. 130(47), 15938–15943 (2008).

[63]Y. Oaki and H. Imai, Angew. Chem. Int. Ed. 46(26), 4951–4955 (2007).

[64]Z. Sun, T. Liao, Y. Dou, S. M. Hwang, M.-S. Park, L. Jiang, J. H. Kim, and S. X. Dou, Nat. Commun. 5, 3813 (2014).

[65]X. Huang, S. Tang, X. Mu, Y. Dai, G. Chen, Z. Zhou, F. Ruan, Z. Yang, and N. Zheng, Nat. Nanotechnol. 6(1), 28–32 (2011).

[66]T. Yu, B. Lim, and Y. Xia, Angew. Chem. Int. Ed. 49(26), 4484–4487 (2010).

[67]T. Taniguchi, K. Yamaguchi, A. Shigeta, Y. Matsuda, S. Hayami, T. Shimizu, T. Matsui, T. Yamazaki, A. Funatstu, Y. Makinose, N. Matsushita, M. Koinuma, and Y. Matsumoto, Adv. Funct. Mater. 23(25), 3140–3145 (2013).

[68]T. Taniguchi, Y. Sonoda, M. Echikawa, Y. Watanabe, K. Hatakeyama, S. Ida, M. Koinuma, and Y. Matsumoto, ACS Appl. Mater. Interfaces 4(2), 1010–1015 (2012).

[69]R. E. Schaak and T. E. Mallouk, Chem. Mater. 12(11), 3427–3434 (2000).

[70]S. Ida, C. Ogata, U. Unal, K. Izawa, T. Inoue, O. Altuntasoglu, and Y. Matsumoto, J. Am. Chem. Soc. 129(29), 8956–8957 (2007).

[71]R. Uppuluri, A. Sen Gupta, A. S. Rosas, and T. E. Mallouk, Chem. Soc. Rev. 47(7), 2401–2430 (2018).

[72]N. Miyamoto, H. Yamamoto, R. Kaito, and K. Kuroda, Chem. Commun. 2002(20), 2378–2379.

[73]Y. Omomo, T. Sasaki, Wang, and M. Watanabe, J. Am. Chem. Soc. 125(12), 3568–3575 (2003).

[74]T. Shibata, G. Takanashi, T. Nakamura, K. Fukuda, Y. Ebina, and T. Sasaki, Energy Environ. Sci. 4(2), 535–542 (2011).

[75]A. Takagaki, T. Yoshida, D. Lu, J. N. Kondo, M. Hara, K. Domen, and S. Hayashi, J. Phys. Chem. B 108(31), 11549–11555 (2004).

[76]K. Fukuda, I. Nakai, Y. Ebina, R. Ma, and T. Sasaki, Inorg. Chem. 46(12), 4787–4789 (2007).

[77]R. E. Schaak and T. E. Mallouk, Chem. Commun. 2002(7), 706–707.

[78]K. Fukuda, K. Akatsuka, Y. Ebina, R. Ma, K. Takada, I. Nakai, and T. Sasaki, ACS Nano 2(8), 1689–1695 (2008).

[79]W. Sugimoto, H. Iwata, Y. Yasunaga, Y. Murakami, and Y. Takasu, Angew. Chem. Int. Ed. 42(34), 4092–4096 (2003).

[80]R. Ma and T. Sasaki, Adv. Mater. 22(45), 5082–5104 (2010).

[81]Y. Ebina, T. Sasaki, and M. Watanabe, Solid State Ionics 151(1), 177–182 (2002).

[82]Z. Liu, R. Ma, Y. Ebina, K. Takada, and T. Sasaki, Chem. Mater. 19(26), 6504–6512 (2007).

[83]T. Maluangnont, K. Matsuba, F. Geng, R. Ma, Y. Yamauchi, and T. Sasaki, Chem. Mater. 25(15), 3137–3146 (2013).

[84]T. Tanaka, Y. Ebina, K. Takada, K. Kurashima, and T. Sasaki, Chem. Mater. 15(18), 3564–3568 (2003).

[85]K. S. Virdi, Y. Kauffmann, C. Ziegler, P. Ganter, P. Blaha, B. V. Lotsch, W. D. Kaplan, and C. Scheu, J. Phys. Chem. C 120(20), 11170–11179 (2016).

[86]M. Im, W.-H. Lee, S.-H. Kweon, C.-Y. Kang, and S. Nahm, J. Eur. Ceram. Soc. 39(4), 1149–1155 (2019).

[87]N. Sakai, Y. Ebina, K. Takada, and T. Sasaki, J. Am. Chem. Soc. 126(18), 5851–5858 (2004).

[88]T. Sasaki and M. Watanabe, J. Phys. Chem. B 101(49), 10159–10161 (1997).

[89]K. Akatsuka, G. Takanashi, Y. Ebina, M.-A. Haga, and T. Sasaki, J. Phys. Chem. C 116(23), 12426–12433 (2012).

[90]Y. Ebina, K. Akatsuka, K. Fukuda, and T. Sasaki, Chem. Mater. 24(21), 4201–4208 (2012).

[91]T. Sasaki, Y. Ebina, K. Fukuda, T. Tanaka, M. Harada, and M. Watanabe, Chem. Mater. 14(8), 3524–3530 (2002).

[92]K. Awaya and S. Ida, Chem. Commun. 56(68), 9811–9814 (2020).

[93]H. Sato, K. Ono, T. Sasaki, and A. Yamagishi, J. Phys. Chem. B 107(36), 9824–9828 (2003).

[94]W. Zhou, N. Umezawa, R. Ma, N. Sakai, Y. Ebina, K. Sano, M. Liu, Y. Ishida, T. Aida, and T. Sasaki, Chem. Mater. 30(18), 6449–6457 (2018).

[95]C. Sun, T. Liao, G. Q. Lu, and S. C. Smith, J. Phys. Chem. C 116(3), 2477–2482 (2012).

[96]T. Sasaki, M. Watanabe, Y. Michiue, Y. Komatsu, F. Izumi, and S. Takenouchi, Chem. Mater. 7(5), 1001–1007 (1995).

[97]T. Sasaki and M. Watanabe, J. Am. Chem. Soc. **120**(19), 4682–4689 (1998).

[98]T. Sasaki, F. Kooli, M. Iida, Y. Michiue, S. Takenouchi, Y. Yajima, F. Izumi, B. C. Chakoumakos, and M. Watanabe, Chem. Mater. **10**(12), 4123–4128 (1998).

[99]F. Geng, R. Ma, A. Nakamura, K. Akatsuka, Y. Ebina, Y. Yamauchi, N. Miyamoto, Y. Tateyama, and T. Sasaki, Nat. Commun. **4**, 1632 (2013).

[100]F. Geng, R. Ma, Y. Ebina, Y. Yamauchi, N. Miyamoto, and T. Sasaki, J. Am. Chem. Soc. **136**(14), 5491–5500 (2014).

[101]Y. Song, N. Iyi, T. Hoshide, T. C. Ozawa, Y. Ebina, R. Ma, S. Yamamoto, N. Miyamoto, and T. Sasaki, Dalton Trans. **47**(9), 3022–3028 (2018).

[102]Y. Song, N. Iyi, T. Hoshide, T. C. Ozawa, Y. Ebina, R. Ma, N. Miyamoto, and T. Sasaki, Chem. Commun. **51**(96), 17068–17071 (2015).

[103]V. Dudko, K. Ottermann, S. Rosenfeldt, G. Papastavrou, and J. Breu, Langmuir **37**(1), 461–468 (2021).

[104]X. Yin, C. S. Tang, Y. Zheng, J. Gao, J. Wu, H. Zhang, M. Chhowalla, W. Chen, and A. T. S. Wee, Chem. Soc. Rev. **50**(18), 10087–10115 (2021).

[105]J. Zheng, H. Zhang, S. Dong, Y. Liu, C. Tai Nai, H. Suk Shin, H. Young Jeong, B. Liu, and K. Ping Loh, Nat. Commun. **5**, 2995 (2014).

[106]S. Park, C. Kim, S. O. Park, N. K. Oh, U. Kim, J. Lee, J. Seo, Y. Yang, H. Y. Lim, S. K. Kwak, G. Kim, and H. Park, Adv. Mater. **32**(33), 2001889 (2020).

[107]H. Feng, Z. Hu, and X. Liu, Chem. Commun. **51**(54), 10961–10964 (2015).

[108]S. Jeong, D. Yoo, M. Ahn, P. Miro, T. Heine, and J. Cheon, Nat. Commun. **6**, 5763 (2015).

[109]G. Eda, H. Yamaguchi, D. Voiry, T. Fujita, M. Chen, and M. Chhowalla, Nano Lett. **11**(12), 5111–5116 (2011).

[110]D. M. Sim, H. J. Han, S. Yim, M.-J. Choi, J. Jeon, and Y. S. Jung, ACS Omega **2**(8), 4678–4687 (2017).

[111]X. Fan, P. Xu, D. Zhou, Y. Sun, Y. C. Li, M. A. T. Nguyen, M. Terrones, and T. E. Mallouk, Nano Lett. **15**(9), 5956–5960 (2015).

[112]T. Carey, A. Arbab, L. Anzi, H. Bristow, F. Hui, S. Bohm, G. Wyatt-Moon, A. Flewitt, A. Wadsworth, N. Gasparini, J. M. Kim, M. Lanza, I. McCulloch, R. Sordan, and F. Torrisi, Adv. Electron. Mater. **7**(7), 2100112 (2021).

[113]X. Gao, J. Yin, G. Bian, H.-Y. Liu, C.-P. Wang, X.-X. Pang, and J. Zhu, Nano Res. **14**(7), 2255–2263 (2021).

[114]Y. Ma, X. Shao, J. Li, B. Dong, Z. Hu, Q. Zhou, H. Xu, X. Zhao, H. Fang, X. Li, Z. Li, J. Wu, M. Zhao, S. J. Pennycook, C. H. Sow, C. Lee, Y. L. Zhong, J. Lu, M. Ding, K. Wang, Y. Li, and J. Lu, ACS Appl. Mater. Interfaces **13**(7), 8518–8527 (2021).

[115]J. Li, P. Song, J. Zhao, K. Vaklinova, X. Zhao, Z. Li, Z. Qiu, Z. Wang, L. Lin, M. Zhao, T. S. Herng, Y. Zuo, W. Jonhson, W. Yu, X. Hai, P. Lyu, H. Xu, H. Yang, C. Chen, S. J. Pennycook, J. Ding, J. Teng, A. H. Castro Neto, K. S. Novoselov, and J. Lu, Nat. Mater. **20**(2), 181–187 (2021).

[116]Z. Lin, Z. Wan, F. Song, B. Huang, C. Jia, Q. Qian, J. S. Kang, Y. Wu, X. Yan, L. Peng, C. Wan, J. Zhou, Z. Sofer, I. Shakir, Z. Almutairi, S. Tolbert, X. Pan, Y. Hu, Y. Huang, and X. Duan, Chem **7**(7), 1887–1902 (2021).

[117]S. Abdolhosseinzadeh, X. Jiang, H. Zhang, J. Qiu, and C. Zhang, Mater. Today **48**, 214–240 (2021).

[118]O. Mashtalir, M. Naguib, V. N. Mochalin, Y. Dall'Agnese, M. Heon, M. W. Barsoum, and Y. Gogotsi, Nat. Commun. **4**, 1716 (2013).

[119]J. Halim, S. Kota, M. R. Lukatskaya, M. Naguib, M.-Q. Zhao, E. J. Moon, J. Pitock, J. Nanda, S. J. May, Y. Gogotsi, and M. W. Barsoum, Adv. Funct. Mater. **26**(18), 3118–3127 (2016).

[120]P. Urbankowski, B. Anasori, T. Makaryan, D. Er, S. Kota, P. L. Walsh, M. Zhao, V. B. Shenoy, M. W. Barsoum, and Y. Gogotsi, Nanoscale **8**(22), 11385–11391 (2016).

[121]M. Alhabeb, K. Maleski, B. Anasori, P. Lelyukh, L. Clark, S. Sin, and Y. Gogotsi, Chem. Mater. **29**(18), 7633–7644 (2017).

[122]J. Xuan, Z. Wang, Y. Chen, D. Liang, L. Cheng, X. Yang, Z. Liu, R. Ma, T. Sasaki, and F. Geng, Angew. Chem. -Int. Ed. **55**(47), 14569–14574 (2016).

[123]G. Decher, J. D. Hong, and J. Schmitt, Thin Solid Films **210–211**, 831–835 (1992).

[124]G. Decher, Science **277**(5330), 1232–1237 (1997).

[125]N. A. Kotov, Nanostruct. Mater. **12**(5), 789–796 (1999).

[126]C. J. Comerci, J. Herrmann, J. Yoon, F. Jabbarpour, X. Zhou, J. F. Nomellini, J. Smit, L. Shapiro, S. Wakatsuki, and W. E. Moerner, Nat. Commun. **10**, 2731 (2019).

[127]Z. Ferjaoui, S. Nahle, C. S. Chang, J. Ghanbaja, O. Joubert, R. Schneider, L. Ferrari, E. Gaffet, and H. Alem, ACS Omega **5**(10), 4770–4777 (2020).

[128]N. A. Kotov, I. Dekany, and J. H. Fendler, J. Phys. Chem. **99**(35), 13065–13069 (1995).

[129]Y. Zhou, R. Ma, Y. Ebina, K. Takada, and T. Sasaki, Chem. Mater. **18**(5), 1235–1239 (2006).

[130]L. Wang, Y. Ebina, K. Takada, and T. Sasaki, J. Phys. Chem. B **108**(14), 4283–4288 (2004).

[131]L. Wang, N. Sakai, Y. Ebina, K. Takada, and T. Sasaki, Chem. Mater. **17**(6), 1352–1357 (2005).

[132]L. Nurdiwijayanto, H. Nishijima, Y. Miyake, N. Sakai, M. Osada, T. Sasaki, and T. Taniguchi, Nano Lett. **21**(16), 7044–7049 (2021).

[133]P. Joo, K. Jo, G. Ahn, D. Voiry, H. Y. Jeong, S. Ryu, M. Chhowalla, and B.-S. Kim, Nano Lett. **14**(11), 6456–6462 (2014).

[134]J. Shen, Y. Pei, P. Dong, J. Ji, Z. Cui, J. Yuan, R. Baines, P. M. Ajayan, and M. Ye, Nanoscale **8**(18), 9641–9647 (2016).

[135]Y. Tian, C. Yang, W. Que, X. He, X. Liu, Y. Luo, X. Yin, and L. B. Kong, J. Power Sources **369**, 78–86 (2017).

[136]H. An, T. Habib, S. Shah, H. Gao, M. Radovic, M. J. Green, and J. L. Lutkenhaus, Sci. Adv. **4**(3), eaaq0118 (2018).

[137]W. Tian, A. VahidMohammadi, Z. Wang, L. Ouyang, M. Beidaghi, and M. M. Hamedi, Nat. Commun. **10**, 2558 (2019).

[138]E. R. Kleinfeld and G. S. Ferguson, Science **265**(5170), 370–373 (1994).

[139]T. Sasaki, Y. Ebina, T. Tanaka, M. Harada, M. Watanabe, and G. Decher, Chem. Mater. **13**(12), 4661–4667 (2001).

[140]Y. Taguchi, R. Kimura, R. Azumi, H. Tachibana, N. Koshizaki, M. Shimomura, N. Momozawa, H. Sakai, M. Abe, and M. Matsumoto, Langmuir **14**(22), 6550–6555 (1998).

[141]T. Yamaki and K. Asai, Langmuir **17**(9), 2564–2567 (2001).

[142]M. Muramatsu, K. Akatsuka, Y. Ebina, K. Wang, T. Sasaki, T. Ishida, K. Miyake, and M.-a. Haga, Langmuir **21**(14), 6590–6595 (2005).

[143]K. Akatsuka, M-a. Haga, Y. Ebina, M. Osada, K. Fukuda, and T. Sasaki, ACS Nano **3**(5), 1097–1106 (2009).

[144]H. Yuan, R. Lubbers, R. Besselink, M. Nijland, and J. E. ten Elshof, ACS Appl. Mater. Interfaces **6**(11), 8567–8574 (2014).

[145]M. Osada, K. Akatsuka, Y. Ebina, H. Funakubo, K. Ono, K. Takada, and T. Sasaki, ACS Nano **4**(9), 5225–5232 (2010).

[146]P. T. P. Le, J. E. ten Elshof, and G. Koster, ACS Appl. Nano Mater. **3**(9), 9487–9493 (2020).

[147]B.-W. Li, M. Osada, T. C. Ozawa, Y. Ebina, K. Akatsuka, R. Ma, H. Funakubo, and T. Sasaki, ACS Nano **4**(11), 6673–6680 (2010).

[148]D. I. Petukhov, A. P. Chumakov, A. S. Kan, V. A. Lebedev, A. A. Eliseev, O. V. Konovalov, and A. A. Eliseev, Nanoscale **11**(20), 9980–9986 (2019).

[149]H. Kim, J. Kee, D.-R. Seo, Y. Lee, C. W. Ahn, and J. Koo, ACS Appl. Mater. Interfaces **12**(37), 42294–42301 (2020).

[150]J. W. Kim, D. Kang, T. H. Kim, S. G. Lee, N. Byun, D. W. Lee, B. H. Seo, R. S. Ruoff, and H. S. Shin, ACS Nano **7**(9), 8082–8088 (2013).

[151]K. Matsuba, C. Wang, K. Saruwatari, Y. Uesusuki, K. Akatsuka, M. Osada, Y. Ebina, R. Ma, and T. Sasaki, Sci. Adv. **3**(6), e1700414 (2017).

[152]A. F. Routh, Rep. Prog. Phys. **76**(4), 046603 (2013).

[153]R. D. Deegan, O. Bakajin, T. F. Dupont, G. Huber, S. R. Nagel, and T. A. Witten, Nature **389**(6653), 827–829 (1997).

[154]H. Hu and R. G. Larson, J. Phys. Chem. B **110**(14), 7090–7094 (2006).

[155]D. Mampallil and H. B. Eral, Adv. Colloid Interface Sci. **252**, 38–54 (2018).

[156]D. Kim, S. Jeong, B. K. Park, and J. Moon, Appl. Phys. Lett. **89**(26), 264101 (2006).

[157]H. Jin, J. Qian, L. Zhou, J. Yuan, H. Huang, Y. Wang, W. M. Tang, and H. L. W. Chan, ACS Appl. Mater. Interfaces **8**(14), 9088–9096 (2016).

[158]W. Sempels, R. De Dier, H. Mizuno, J. Hofkens, and J. Vermant, Nat. Commun. **4**, 1757 (2013).

[159]P. He and B. Derby, Adv. Mater. Interfaces **4**(22), 1700944 (2017).

[160]P. J. Yunker, T. Still, M. A. Lohr, and A. G. Yodh, Nature **476**(7360), 308–311 (2011).

[161]M. Eslamian and F. Zabihi, Nanoscale Res. Lett. **10**, 462 (2015).

[162]E. He, D. Guo, and Z. Li, Adv. Mater. Interfaces **6**(14), 1900446 (2019).

[163]S. Haar, M. El Gemayel, Y. Shin, G. Melinte, M. A. Squillaci, O. Ersen, C. Casiraghi, A. Ciesielski, and P. Samorì, Sci. Rep. **5**, 16684 (2015).

[164]F. Soltani-Kordshuli and M. Eslamian, Exp. Therm. Fluid Sci. **89**, 238–248 (2017).

[165]Y. Shi, M. Osada, Y. Ebina, and T. Sasaki, ACS Nano **14**(11), 15216–15226 (2020).

[166]J. Park, K. An, Y. Hwang, J.-G. Park, H.-J. Noh, J.-Y. Kim, J.-H. Park, N.-M. Hwang, and T. Hyeon, Nat. Mater. **3**(12), 891–895 (2004).

[167]E. V. Shevchenko, D. V. Talapin, N. A. Kotov, S. O'Brien, and C. B. Murray, Nature **439**(7072), 55–59 (2006).

[168]B. T. Diroll, T. R. Gordon, E. A. Gaulding, D. R. Klein, T. Paik, H. J. Yun, E. D. Goodwin, D. Damodhar, C. R. Kagan, and C. B. Murray, Chem. Mater. **26**(15), 4579–4588 (2014).

[169]L. Luo, M. D. Rossell, D. Xie, R. Erni, and M. Niederberger, ACS Sustainable Chem. Eng. **1**(1), 152–160 (2013).

[170]B. M. Crockett, A. W. Jansons, K. M. Koskela, M. C. Sharps, D. W. Johnson, and J. E. Hutchison, Chem. Mater. **31**(9), 3370–3380 (2019).

[171]M. Osada and T. Sasaki, APL Mater. **7**(12), 120902 (2019).

[172]T. Shibata, N. Sakai, K. Fukuda, Y. Ebina, and T. Sasaki, Phys. Chem. Chem. Phys. **9**(19), 2413–2420 (2007).

[173]G. Liu, L. Wang, C. Sun, Z. Chen, X. Yan, L. Cheng, H.-M. Cheng, and G. Q. Lu, Chem. Commun. **2009**(11), 1383–1385.

[174]M. Osada, G. Takanashi, B.-W. Li, K. Akatsuka, Y. Ebina, K. Ono, H. Funakubo, K. Takada, and T. Sasaki, Adv. Funct. Mater. **21**(18), 3482–3487 (2011).

[175]Y.-H. Kim, H.-J. Kim, M. Osada, B.-W. Li, Y. Ebina, and T. Sasaki, ACS Appl. Mater. Interfaces **6**(22), 19510–19514 (2014).

[176]M. Osada and T. Sasaki, Int. J. Appl. Ceram. Technol. **9**(1), 29–36 (2012).

[177]B.-W. Li, M. Osada, Y.-H. Kim, Y. Ebina, K. Akatsuka, and T. Sasaki, J. Am. Chem. Soc. **139**(31), 10868–10874 (2017).

[178]L. Kang, H. An, S. Jung, S. Kim, S. Nahm, D.-G. Kim, and C. G. Lee, Appl. Surf. Sci. **476**, 374–377 (2019).

[179]K. Fukuda, Y. Ebina, T. Shibata, T. Aizawa, I. Nakai, and T. Sasaki, J. Am. Chem. Soc. **129**(1), 202–209 (2007).

[180]B.-W. Li, M. Osada, Y. Ebina, K. Akatsuka, K. Fukuda, and T. Sasaki, ACS Nano **8**(6), 5449–5461 (2014).

[181]T. Chen, X. Gao, J.-Y. Zhang, J.-L. Xu, and S.-D. Wang, Adv. Opt. Mater. **8**(4), 1901289 (2020).

[182]J. Zou, Q. Zhang, K. Huang, and N. Marzari, J. Phys. Chem. C **114**(24), 10725–10729 (2010).

[183]J. Xu, W. Zheng, and F. Huang, J. Mater. Chem. C **7**(29), 8753–8770 (2019).

[184]K. Matsuzaki, T. Taniguchi, Y. Matsumoto, and M. Hara, Appl. Phys. Lett. **106**(3), 033104 (2015).

[185]Y. Zhang, S. Li, Z. Li, H. Liu, X. Liu, J. Chen, and X. Fang, Nano Lett. **21**(1), 382–388 (2021).

[186]S. Li, Y. Zhang, W. Yang, H. Liu, and X. Fang, Adv. Mater. **32**(7), 1905443 (2020).

[187]L. Chang, M. A. Holmes, M. Waller, F. E. Osterloh, and A. J. Moulé, J. Mater. Chem. **22**(38), 20443–20450 (2012).

[188]S. Ohisa, T. Hikichi, Y.-J. Pu, T. Chiba, and J. Kido, ACS Appl. Mater. Interfaces **10**(33), 27885–27893 (2018).

[189]T.-P. Chen, C.-W. Lin, S.-S. Li, Y.-H. Tsai, C.-Y. Wen, W. J. Lin, F.-M. Hsiao, Y.-P. Chiu, K. Tsukagoshi, M. Osada, T. Sasaki, and C.-W. Chen, Adv. Energy Mater. **8**(2), 1701722 (2018).

[190]A. P. Thilakan, J.-X. Li, T.-P. Chen, S.-S. Li, C.-W. Chen, M. Osada, K. Tsukagoshi, T. Sasaki, A. Yabushita, K.-H. Wu, and C.-W. Luo, ACS Appl. Mater. Interfaces **11**(24), 21473–21480 (2019).

[191]T. Li, S. Jiang, N. Sivadas, Z. Wang, Y. Xu, D. Weber, J. E. Goldberger, K. Watanabe, T. Taniguchi, C. J. Fennie, K. Fai Mak, and J. Shan, Nat. Mater. **18**(12), 1303–1308 (2019).

[192]Y. Deng, Y. Yu, Y. Song, J. Zhang, N. Z. Wang, Z. Sun, Y. Yi, Y. Z. Wu, S. Wu, J. Zhu, J. Wang, X. H. Chen, and Y. Zhang, Nature **563**(7729), 94–99 (2018).

[193]M. Osada, Y. Ebina, K. Takada, and T. Sasaki, Adv. Mater. **18**(3), 295–299 (2006).

[194]X. Dong, M. Osada, H. Ueda, Y. Ebina, Y. Kotani, K. Ono, S. Ueda, K. Kobayashi, K. Takada, and T. Sasaki, Chem. Mater. **21**(19), 4366–4373 (2009).

[195]M. Osada, Y. Ebina, K. Fukuda, K. Ono, K. Takada, K. Yamaura, E. Takayama-Muromachi, and T. Sasaki, Phys. Rev. B **73**(15), 153301 (2006).

[196]Y. Matsumoto, M. Murakami, T. Shono, T. Hasegawa, T. Fukumura, M. Kawasaki, P. Ahmet, T. Chikyow, S.-Y. Koshihara, and H. Koinuma, Science **291**(5505), 854–856 (2001).

[197]M. Osada, M. Itose, Y. Ebina, K. Ono, S. Ueda, K. Kobayashi, and T. Sasaki, Appl. Phys. Lett. **92**(25), 253110 (2008).

[198]D. S. Kim, T. C. Ozawa, K. Fukuda, S. Ohshima, I. Nakai, and T. Sasaki, Chem. Mater. **23**(11), 2700–2702 (2011).

[199]J. Sato, H. Kato, M. Kimura, K. Fukuda, and W. Sugimoto, Langmuir **26**(23), 18049–18054 (2010).

[200]C. Wang, M. Osada, Y. Ebina, B.-W. Li, K. Akatsuka, K. Fukuda, W. Sugimoto, R. Ma, and T. Sasaki, ACS Nano **8**(3), 2658–2666 (2014).

[201]D.-S. Ko, W.-J. Lee, S. Sul, C. Jung, D.-J. Yun, H.-G. Kim, W.-J. Son, J. G. Chung, D. W. Jung, S. Y. Kim, J. Kim, W. Lee, C. Kwak, J. K. Shin, J.-H. Kim, and J. W. Roh, NPG Asia Mater. **10**, 266–276 (2018).

[202]P. Mustonen, D. M. A. Mackenzie, and H. Lipsanen, Front. Optoelectron. **13**(2), 91–113 (2020).

[203]D.-J. Yun, S. Y. Kim, D.-S. Ko, S. Heo, K. Kim, and S. H. Kim, Appl. Surf. Sci. **529**, 147154 (2020).

[204]S. Yoo, J. Kim, H. Moon, S. Y. Kim, D.-S. Ko, W. H. Shin, S. Hwang, D. W. Jung, S. Sul, C. Kwak, J. W. Roh, and W. Lee, Nanoscale **9**(21), 7104–7113 (2017).

[205]M. Osada, T. Sasaki, K. Ono, Y. Kotani, S. Ueda, and K. Kobayashi, ACS Nano **5**(9), 6871–6879 (2011).

[206]N. Sakai, Y. Omomo, Y. Ebina, K. Takada, and T. Sasaki, J. Phys. Chem. C **112**(13), 5197–5202 (2008).

[207]Y.-H. Kim, L. Dong, M. Osada, B.-W. Li, Y. Ebina, and T. Sasaki, Nanotechnology **26**(24), 244001 (2015).

[208]M. S. Khan, M. Osada, L. Dong, Y.-H. Kim, Y. Ebina, and T. Sasaki, ACS Appl. Mater. Interfaces **13**(1), 1783–1790 (2021).

[209]B.-W. Li, M. Osada, Y. Ebina, S. Ueda, and T. Sasaki, J. Am. Chem. Soc. **138**(24), 7621–7625 (2016).

[210]H. Yano, N. Sakai, Y. Ebina, R. Ma, M. Osada, K. Fujimoto, and T. Sasaki, ACS Appl. Mater. Interfaces **13**(36), 43258–43265 (2021).

[211]X. Cai, R. Ma, T. C. Ozawa, N. Sakai, A. Funatsu, and T. Sasaki, Nanoscale **6**(23), 14419–14427 (2014).

[212]X. Cai, N. Sakai, T. C. Ozawa, A. Funatsu, R. Ma, Y. Ebina, and T. Sasaki, ACS Appl. Mater. Interfaces **7**(21), 11436–11443 (2015).

[213]N. Sakai, K. Kamanaka, and T. Sasaki, J. Phys. Chem. C **120**(42), 23944–23950 (2016).

[214]T. Taniguchi, S. Li, L. Nurdiwijayanto, Y. Kobayashi, T. Saito, Y. Miyata, S. Obata, K. Saiki, H. Yokoi, K. Watanabe, T. Taniguchi, K. Tsukagoshi, Y. Ebina, T. Sasaki, and M. Osada, ACS Nano **13**(10), 11214–11223 (2019).

[215]J. Song, Y. Chu, Z. Liu, and H. Xu, J. Mater. Chem. C **9**(5), 1701–1708 (2021).

[216]A. Chaves, J. G. Azadani, H. Alsalman, D. R. da Costa, R. Frisenda, A. J. Chaves, S. H. Song, Y. D. Kim, D. He, J. Zhou, A. Castellanos-Gomez, F. M. Peeters, Z. Liu, C. L. Hinkle, S.-H. Oh, P. D. Ye, S. J. Koester, Y. H. Lee, P. Avouris, X. Wang, and T. Low, npj 2D Mater. Appl. **4**, 29 (2020).

[217]B. Lyu, M. Kim, H. Jing, J. Kang, C. Qian, S. Lee, and J. H. Cho, ACS Nano **13**(10), 11392–11400 (2019).

[218]K. Montazeri, M. Currie, L. Verger, P. Dianat, M. W. Barsoum, and B. Nabet, Adv. Mater. **31**(43), 1903271 (2019).

[219]C. Zhang, B. Anasori, A. Seral-Ascaso, S.-H. Park, N. McEvoy, A. Shmeliov, G. S. Duesberg, J. N. Coleman, Y. Gogotsi, and V. Nicolosi, Adv. Mater. **29**(36), 1702678 (2017).

[220]W. Chen, L.-X. Liu, H.-B. Zhang, and Z.-Z. Yu, ACS Nano **14**(12), 16643–16653 (2020).

[221]J. L. Hart, K. Hantanasirisakul, A. C. Lang, B. Anasori, D. Pinto, Y. Pivak, J. T. van Omme, S. J. May, Y. Gogotsi, and M. L. Taheri, Nat. Commun. **10**, 522 (2019).

[222]M. Han, K. Maleski, C. E. Shuck, Y. Yang, J. T. Glazar, A. C. Foucher, K. Hantanasirisakul, A. Sarycheva, N. C. Frey, S. J. May, V. B. Shenoy, E. A. Stach, and Y. Gogotsi, J. Am. Chem. Soc. **142**(45), 19110–19118 (2020).

[223]M. Han, C. E. Shuck, R. Rakhmanov, D. Parchment, B. Anasori, C. M. Koo, G. Friedman, and Y. Gogotsi, ACS Nano **14**(4), 5008–5016 (2020).

[224]G. Nakada, Y. Igarashi, H. Imai, and Y. Oaki, Adv. Theory Simul. **2**(4), 1800180 (2019).

[225]A. Sebastian, R. Pendurthi, T. H. Choudhury, J. M. Redwing, and S. Das, Nat. Commun. **12**, 693 (2021).

28 September 2023 06:36:42

[226]H. Nishino, T. Fujita, N. T. Cuong, S. Tominaka, M. Miyauchi, S. Iimura, A. Hirata, N. Umezawa, S. Okada, E. Nishibori, A. Fujino, T. Fujimori, S.-I. Ito, J. Nakamura, H. Hosono, and T. Kondo, J. Am. Chem. Soc. **139**(39), 13761–13769 (2017).

[227]R. Liu and W. Li, ACS Omega **3**(3), 2609–2617 (2018).

[228]M. Narayanasamy, B. Kirubasankar, M. Shi, S. Velayutham, B. Wang, S. Angaiah, and C. Yan, Chem. Commun. **56**(47), 6412–6415 (2020).

[229]S. Pei and H.-M. Cheng, Carbon **50**(9), 3210–3228 (2012).

[230]Y. Xie and P. R. C. Kent, Phys. Rev. B **87**(23), 235441 (2013).

[231]G. Gao, G. Ding, J. Li, K. Yao, M. Wu, and M. Qian, Nanoscale **8**(16), 8986–8994 (2016).

[232]X.-H. Zha, Q. Huang, J. He, H. He, J. Zhai, J. S. Francisco, and S. Du, Sci. Rep. **6**, 27971 (2016).

[233]H. Weng, A. Ranjbar, Y. Liang, Z. Song, M. Khazaei, S. Yunoki, M. Arai, Y. Kawazoe, Z. Fang, and X. Dai, Phys. Rev. B **92**(7), 075436 (2015).

[234]A. Laturia, M. L. Van de Put, and W. G. Vandenberghe, npj 2D Mater. Appl. **2**, 6 (2018).

28 September 2023 06:36:42